Magnetic states of the ionosphere of Venus observed by Venus Express

Von der Fakultät für Elektrotechnik, Informationstechnik, Physik
der Technischen Universität Carolo-Wilhelmina
zu Braunschweig
zur Erlangung des Grades einer
Doktorin der Naturwissenschaften
(Dr. rer. nat.)
genehmigte
Dissertation

von Anne Angsmann
aus Oelde

Bibliografische Information der Deutschen Nationalbibliothek

Die Deutsche Nationalbibliothek verzeichnet diese Publikation in der Deutschen Nationalbibliografie; detaillierte bibliografische Daten sind im Internet über `http://dnb.d-nb.de` abrufbar.

1. Referentin oder Referent: Prof. Dr. Uwe Motschmann
2. Referentin oder Referent: Prof. Dr. Kristian Schlegel
eingereicht am: 25. Januar 2011
mündliche Prüfung (Disputation) am: 31. März 2011

ISBN 978-3-942171-49-6

uni-edition GmbH 2011
http://www.uni-edition.de
© Anne Angsmann

This work is distributed under a
Creative Commons Attribution 3.0 License

Printed in Germany

Vorveröffentlichungen aus der Dissertation

Teilergebnisse aus dieser Arbeit wurden mit Genehmigung der Fakultät für Elektrotechnik, Informationstechnik und Physik, vertreten durch den Mentor der Arbeit, in folgenden Beiträgen vorab veröffentlicht:

Publikationen:

- **A. Angsmann**, M. Fränz, E. Dubinin, J. Woch, S. Barabash, T.L. Zhang and U. Motschmann, *Magnetic States of the Ionosphere of Venus observed by Venus Express*, Planetary and Space Science, doi: 10.1016/j.pss.2010.12.004

Tagungsbeiträge:

- **A. Angsmann**, M. Fränz, N. Krupp, J. Woch, E. Dubinin, C. Martinecz, S. Barabash, M. Pätzold and T.L. Zhang, *Structure and dynamics of the ionopause of Venus*, European Planetary Science Congress (EPSC), Münster, Deutschland, 22. - 26. September 2008 (Vortrag).

- **M. Fränz**, A. Angsmann, E. Dubinin, C. Martinecz, J. Woch, S. Barabash, R. Lundin and A. Fedorov, *Ion density and transport in the upper ionospheres of Mars and Venus*, European Planetary Science Congress (EPSC), Münster, Deutschland, 22. - 26. September 2008 (Vortrag).

- **A. Angsmann**, M. Fränz, N. Krupp, J. Woch, E. Dubinin, C. Martinecz, S. Barabash, M. Pätzold and T.L. Zhang, *Structure and dynamics of the upper ionosphere of Venus*, Solar System Seminar, Max-Planck-Institut für Sonnensystemforschung (MPS), Katlenburg-Lindau, Deutschland, 3. Dezember 2008 (Vortrag).

- A. Angsmann, **M. Fränz**, N. Krupp, J. Woch, E. Dubinin, S. Barabash, M. Pätzold and T.L. Zhang, *Structure and dynamics of the upper ionosphere of Venus*, European Geosciences Union (EGU) General Assembly 2009, Wien, Österreich, 19. - 24. April 2009 (Vortrag).

- **M. Fränz**, E. Dubinin, E. Nielsen, A. Angsmann, J. Woch, S. Barabash, R. Lundin and A. Fedorov, *Ion transport in the upper ionospheres of Mars and Venus*, European Geosciences Union (EGU) General Assembly 2009, Wien, Österreich, 19. - 24. April 2009 (Vortrag).

- **A. Angsmann**, M. Fränz, E. Dubinin, J. Woch, S. Barabash, M. Pätzold, C. Martinecz and T.L. Zhang, *Structure and dynamics of the upper ionosphere of Venus*, International Conference on Comparative Planetology: Venus - Earth - Mars (ESLAB), ESTEC, Noordwijk, Niederlande, 11. - 15. Mai 2009 (Poster).

- **M. Fränz**, E. Dubinin, E. Nielsen, A. Angsmann, J. Woch, S. Barabash, R. Lundin and A. Fedorov, *Ion transport in the upper ionospheres of Mars and Venus*, International Conference on Comparative Planetology: Venus - Earth - Mars (ESLAB), ESTEC, Noordwijk, Niederlande, 11. - 15. Mai 2009 (Vortrag).

- **A. Angsmann**, M. Fränz, N. Krupp, J. Woch, E. Dubinin, S. Barabash, M. Pätzold and T.L. Zhang, *Structure and dynamics of the upper ionosphere of Venus*, European Planetary Science Congress (EPSC), Potsdam, Deutschland, 13. - 18. September 2009 (Vortrag).

- **A. Angsmann**, M. Fränz, N. Krupp, J. Woch, E. Dubinin, S. Barabash, M. Pätzold and T.L. Zhang, *Structure and dynamics of the upper ionosphere of Venus*, Solar System Seminar, Max-Planck-Institut für Sonnensystemforschung (MPS), Katlenburg-Lindau, Deutschland, 25. November 2009 (Vortrag).

- **A. Angsmann**, M. Fränz, J. Woch, E. Dubinin, S. Barabash, M. Pätzold and T.L. Zhang, *Structure and dynamics of the upper ionosphere of Venus*, ASPERA Team-Meeting, Bern, Schweiz, 7. - 8. Dezember 2009 (Vortrag).

- **A. Angsmann**, M. Fränz, J. Woch, E. Dubinin, C. Martinecz, S. Barabash, T.L. Zhang and U. Motschmann, *Structure and dynamics of the upper ionosphere of Venus*, Oberseminar, Institut für Theoretische Physik, Technische Universität Braunschweig, Braunschweig, Deutschland, 29. April 2010 (Vortrag).

- **A. Angsmann**, M. Fränz, E. Dubinin, J. Woch, U. Motschmann, S. Barabash, M. Pätzold and T.L. Zhang, *Structure and dynamics of the ionosphere of Venus*, European Geosciences Union (EGU) General Assembly 2010, Wien, Österreich, 2. - 7. Mai 2010 (Poster).

- **M. Fränz**, E. Dubinin, E. Nielsen, A. Angsmann, J. Woch, S. Barabash, R. Lundin and A. Fedorov, *Cross-terminator flow in the ionosphere of Mars*, European Geosciences Union (EGU) General Assembly 2010, Wien, Österreich, 2. - 7. Mai 2010 (Poster).

- **A. Angsmann**, M. Fränz, J. Woch, E. Dubinin, S. Barabash, M. Pätzold, T.L. Zhang and U. Motschmann, *Structure and dynamics of the upper ionosphere of Venus*, ASPERA Team-Meeting, IRF, Kiruna, Schweden, 9. - 11. Juni 2010 (Vortrag).

- **M. Fränz**, E. Dubinin, A. Angsmann, E. Nielsen, J. Woch, S. Barabash, R. Lundin and A. Fedorov, *Cross-terminator ion flow in the ionospheres of Mars and Venus*, 38th COSPAR Scientific Assembly, Bremen, Deutschland, 18. - 25. Juli 2010 (Vortrag).

- **A. Angsmann**, M. Fränz, J. Woch, E. Dubinin, S. Barabash, M. Pätzold, T.L. Zhang and U. Motschmann, *Structure and dynamics of the ionosphere of Venus*, European Planetary Science Congress (EPSC), Rom, Italien, 19. - 24. September 2010 (Vortrag).

- **A. Angsmann**, M. Fränz, N. Krupp, J. Woch, E. Dubinin, C. Martinecz, S. Barabash, T.L. Zhang and U. Motschmann, *Magnetic fields in the ionosphere of Venus*, Solar System Seminar, Max-Planck-Institut für Sonnensystemforschung (MPS), Katlenburg-Lindau, Deutschland, 20. Oktober 2010 (Vortrag).

- **A. Angsmann**, M. Fränz, J. Woch, E. Dubinin, S. Barabash, M. Pätzold, T.L. Zhang and U. Motschmann, *Structure and dynamics of the upper ionosphere of Venus*, American Geophysical Union (AGU) Fall Meeting, San Francisco, USA, 13. - 17. Dezember 2010 (Vortrag).

- **A. Angsmann**, M. Fränz, E. Dubinin, J. Woch, S. Barabash, T. Zhang and U. Motschmann, *Magnetic states of the ionosphere of Venus*, European Geosciences Union (EGU) General Assembly 2011, Wien, Österreich, 3. - 8. April 2011 (Vortrag).

- **M. Fränz**, E. Dubinin, E. Nielsen, A. Angsmann, J. Woch, S. Barabash, R. Lundin, A. Fedorov and T. Zhang, *Trans-terminator flow in the ionospheres of Mars and Venus*, European Geosciences Union (EGU) General Assembly 2011, Wien, Österreich, 3. - 8. April 2011 (Vortrag).

Contents

Abstract **9**

1 Introduction **11**
1.1 Observational history of Venus . . . 13
1.1.1 Ground-based observations . . . 13
1.1.2 Space missions to Venus . . . 14
1.1.3 Long-term missions to Venus (PVO and VEX) . . . 17
1.1.3.1 Pioneer Venus Orbiter . . . 17
1.1.3.2 Venus Express . . . 19
1.2 Planet Venus . . . 25
1.2.1 Surface and geology . . . 25
1.2.2 Atmosphere . . . 28
1.2.2.1 Composition . . . 28
1.2.2.2 Dynamics . . . 30
1.2.3 Ionosphere . . . 31
1.2.4 Plasma environment . . . 37
1.2.4.1 Solar wind and IMF . . . 38
1.2.4.2 Interaction with the solar wind . . . 38
1.2.4.3 Magnetization states of the ionosphere . . . 41
1.3 Magnetospheres in our solar system . . . 45
1.3.1 Magnetized bodies . . . 45
1.3.1.1 Earth . . . 45
1.3.1.2 Mercury . . . 48
1.3.1.3 The gas giants in our solar system . . . 50
1.3.1.4 Ganymede . . . 51
1.3.2 Unmagnetized bodies . . . 52
1.3.2.1 Comets . . . 52
1.3.2.2 Moons . . . 53
1.3.3 Partially magnetized bodies . . . 55
1.3.3.1 Mars . . . 55
1.3.3.2 Induced magnetic fields in moons . . . 56

2 Data analysis **59**
2.1 Coordinate systems . . . 59
2.1.1 Aberration . . . 61
2.2 Interpretation of Venus Express plasma data . . . 62

2.2.1 ELS measurements 62
2.2.2 MAG measurements 64
2.2.3 Plasma boundary identification 65
2.2.3.1 Bow shock 68
2.2.3.2 Induced magnetopause 68
2.2.3.3 Ionopause/PEB 70
2.3 Relations between plasma parameters 70
2.4 VeRa electron density profiles 80
2.5 Magnetization states of the ionosphere 83
2.5.1 Long-time averaged B fields 85
2.5.2 Manual sorting and cross-correlation method 87
2.5.2.1 Sample plots of magnetized and unmagnetized states . 90
2.5.2.2 Transitional cases 92
2.5.3 Mean magnetic field method 97
2.5.3.1 Comparison with manually sorted orbits 97
2.6 Influence of external factors on ionospheric magnetization 99

3 Comparison with previous results 109
3.1 Plasma boundaries 109
3.1.1 Bow shock 109
3.1.2 Magnetopause 110
3.1.2.1 Magnetospheric flaring angle 110
3.1.3 Ionopause 112
3.2 Ionospheric magnetization 115

4 Summary and conclusions 117

5 Outlook 119

Bibliography 121

Acknowledgements 131

Curriculum Vitae 135

Abstract

This thesis focuses on the investigation of the prevalence of magnetic fields in the ionosphere of Venus, and on their implications and dependence on external factors.
Strong ultraviolet radiation from the Sun ionizes the upper atmosphere of Venus, creating a dense ionosphere on the dayside of the planet. In contrast to Earth, the ionosphere of Venus is not protected against the solar wind by a magnetic field. However, the interaction between the ionospheric plasma and the solar wind dynamic and magnetic pressure creates a pseudo-magnetosphere which deflects the solar wind flow around the planet (Schunk and Nagy (1980)). The combination of changing solar radiation and solar wind intensities leads to a highly variable structure and plasma composition of the ionosphere. The instrumentation of the Venus Express spacecraft allows to measure the magnetic field (MAG experiment) as well as the electron energy spectrum and the ion composition (ASPERA-4 experiment) of the upper ionosphere and ionopause. In contrast to the earlier Pioneer Venus Orbiter (PVO) measurements which were conducted during solar maximum, the solar activity was very low in the period 2006 - 2009. A comparison with PVO allows for an investigation of ionospheric properties under different solar wind and EUV radiation conditions. Observations of MAG and ASPERA have been analyzed to determine the positions of the photoelectron boundary (PEB), the induced "magnetopause" and the bow shock together with their dependence on the solar zenith angle (SZA). The PEB was determined using the ELS observations of ionospheric photoelectrons, which can be identified by their specific energy range. It is of particular interest to explore the different magnetic states of the ionosphere, since these influence the local plasma conductivity, currents and probably the escape of electrons and ions. The penetration of magnetic fields into the ionosphere depends on external conditions as well as on ionospheric properties. By analyzing a large number of orbits, using a combination of two different methods, we define criteria to distinguish between the so-called magnetized and unmagnetized ionospheric states. Furthermore, we confirm that the average magnetic field inside the ionosphere shows a linear dependence on the magnetic field in the region directly above the PEB, and we investigated several other interrelations between plasma parameters and magnetic fields.
For the future, a comparison of ASPERA-4 results with computer simulations of the ionosphere is planned. Furthermore, the PEB locations determined from these data can be verified by using ionopause altitudes derived from VeRa data, a procedure which will also yield a better overview of the general shape of the ionopause/PEB layer. Another future possibility is the comparison of ASPERA-derived PEBs with existing theoretical models describing the ionosphere.

1 Introduction

Venus is the second planet of our solar system, seen from the Sun. It is often called the Earth's sister or twin because both planets have very similar diameters, bulk densities and surface gravity. Apart from these basic properties, however, they are strikingly different. The average surface temperature on Venus is about 737 K, accompanied by an atmospheric surface pressure of 92 bar (Williams (2010), see also Table 1.3). Venus orbits the Sun on a slightly elliptic trajectory with a semi-major axis of about $1.08 \cdot 10^8$ km, corresponding to 0.723 Astronomical Units (AU)[1]. Its orbital period is 224.7 days. One of the many puzzling facts about Venus is its rotation. Firstly, it rotates in a retrograde way, which means opposite to its orbital motion (and to most other planets' rotational direction), and secondly, this motion is very slow and thus one sidereal[2] Venus day lasts for about 243 Earth days. In the extreme case of Venus, however, the length of a solar day differs largely from the sidereal day and is only about 116.75 Earth days due to the effects of its motion around the Sun. Since the rotational axis of Venus is inclined by only 2.6° to its orbital plane[3] and at the same time, its orbit is nearly perfectly circular, there are hardly any detectable seasonal effects. A comparison of bulk parameters and orbital characteristics of Venus and Earth is provided in Table 1.1 and 1.2, respectively.
In addition to the lack of seasons, the rapidly rotating clouds distribute irradiated solar energy efficiently across the whole planet, especially from dayside to nightside, but there are winds from equator to pole as well. See Section 1.2.2.1 for more details on the cloud dynamics. Another salient difference between Earth and Venus is that the latter lacks an intrinsic magnetic field. This leads to a very different dynamic interaction with the solar wind. While at Earth, the magnetic pressure of the intrinsic magnetosphere keeps off the solar wind, this is mainly accomplished via thermal plasma pressure at Venus. Nevertheless, both planets have analogous plasma regions, e.g. an ionosphere, a magnetosphere and a clear bow shock. Still, these generally display different scales and generation processes, and there are many boundaries which do not have an analogue at the respective other planet. The plasma environment of Venus will be described in detail in Section 1.2.4. Planet Venus thus still holds many mysteries and riddles, and the aim of this thesis is to contribute additional knowledge to help solving them.

[1] 1 AU = 149,597,871 km. Originally one AU was defined as the semi-major axis of the Earth's orbit around the Sun. Nowadays the definition has been modified, but it is still very close to the average distance between Earth and Sun.

[2] A sidereal day is defined as one rotation of the planet with respect to the background, e.g. distant stars. Due to the orbital motion, this differs from the solar day, which is defined as the time of a rotation until the same meridian is facing the Sun again.

[3] Because of the retrograde rotation of Venus, this angle is sometimes given as 177.4 °.

	Venus	**Earth**	**Ratio (Venus/Earth)**
Mass (10^{24} kg)	4.8685	5.9736	0.815
Volume (10^{10} km^3)	92.843	108.321	0.857
Equatorial radius (km)	6051.8	6378.1	0.949
Polar radius (km)	6051.8	6356.8	0.952
Volumetric mean radius (km)	6051.8	6371.0	0.950
Ellipticity (Flattening)	0.000	0.00335	0.0
Mean density (kg/m^3)	5243	5515	0.951
Surface gravity (eq.) (m/s^2)	8.87	9.80	0.905
Escape velocity (km/s)	10.36	11.19	0.926
Bond albedo	0.76	0.306	2.94
Visual geometric albedo	0.67	0.367	1.83
Solar irradiance (W/m^2)	2613.9	1367.6	1.911
Black-body temperature (K)	231.7	254.3	0.724
Topographic range (km)	15	20	0.750
Number of natural satellites	0	1	-
Planetary ring system	No	No	-

Table 1.1: Bulk parameters of Venus and Earth in comparison (Taylor (2006), Williams (2010))

	Venus	**Earth**	**Ratio (Venus/Earth)**
Semi-major axis (10^6 km)	108.21	149.60	0.723
Sidereal orbit period (days)	224.701	365.256	0.615
Tropical orbit period (days)	224.695	365.242	0.615
Perihelion (10^6 km)	107.48	147.09	0.731
Aphelion (10^6 km)	108.94	152.10	0.716
Mean orbital velocity (km/s)	35.02	29.78	1.176
Orbit inclination (deg)	3.39	0.00	-
Orbit eccentricity	0.0067	0.0167	0.401
Sidereal rotation period (hrs)	5832.5	23.9345	243.686
Length of day (hrs)	2802.0	24.0000	116.750
Obliquity to orbit (deg)	177.36	23.45	(0.113)

Table 1.2: Orbital parameters of Venus and Earth in comparison (Taylor (2006))

1.1 Observational history of Venus

1.1.1 Ground-based observations

Venus has been well-known already in ancient times as the morning and evening star. Apart from the Sun and the Moon, it is the brightest object visible in the sky and can, under good conditions, even be seen during full daylight. Since the radius of its orbit around the Sun is smaller than for the Earth, it can never be seen in opposition from our planet. Instead, Venus displays different phases similar to our Moon, and appears at varying angular diameters (between 10 and 66 arcseconds) depending on its actual distance from the Earth (see Figure 1.1). Galileo Galilei observed these phases in 1610 with his small telescope, and realized that this finding was a contradiction to the geocentric model which was the standard at his time.

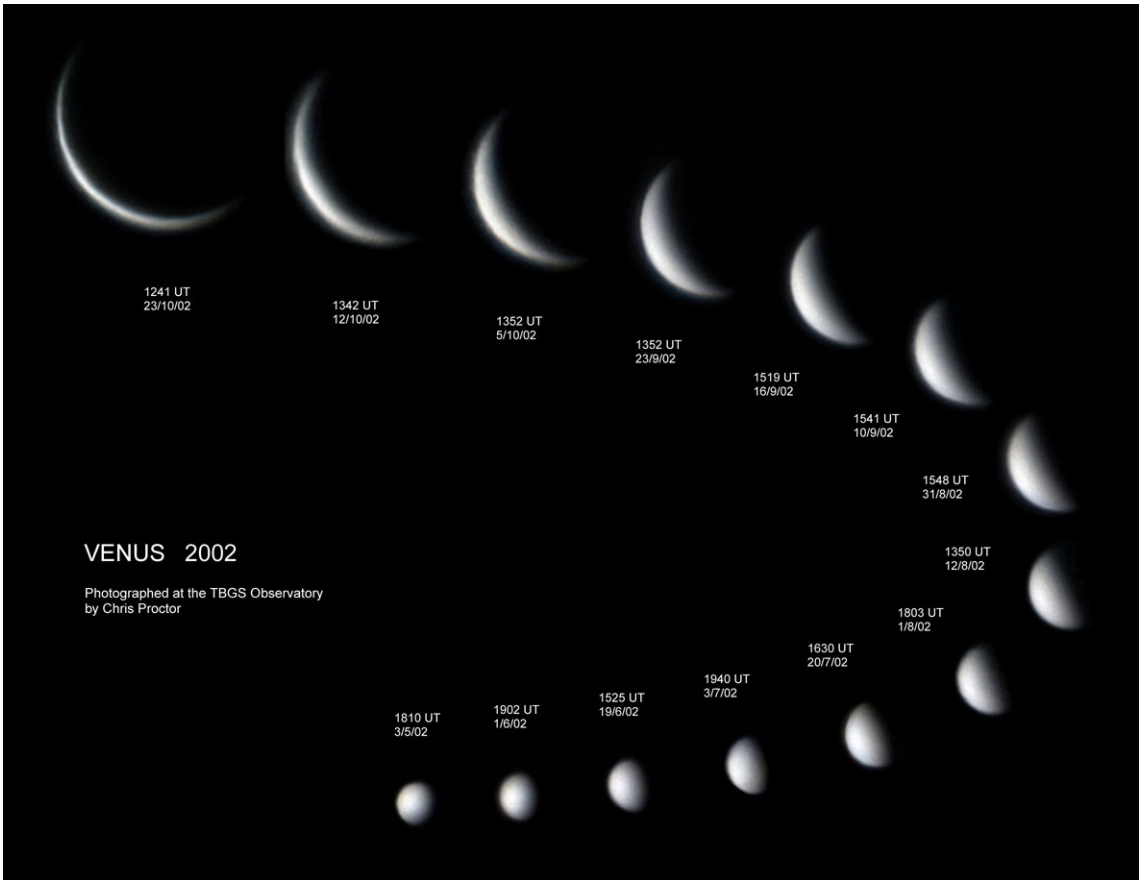

Figure 1.1: The phases of Venus, as observed from the Earth (© Chris Proctor). One can clearly see the variations in apparent diameter due to the changing distance from our planet, and recognize the correlation with the illuminated part of the visible disk.

The largest angular distance from the Sun that Venus can have in the Earth's sky is about 47°, making it sometimes visible for several hours after sunset (in the so-called eastern elongation) or before sunrise (in western elongation). The reason why this planet appears so bright is not only due to its closeness to Earth, but also due to its high albedo of about

0.76 (Taylor (2006)), which is the largest among all planets in our solar system. The orbital inclination of Venus with respect to the ecliptic plane is 3.4°. This implies that Venus passes exactly between Sun and Earth only on very rare occasions[4]. During such a so-called transit, it blocks a tiny fraction of the sunlight and can be seen as a black spot on the Sun's disk even with the naked eye (with appropriate protection). In the past, transits were used to determine distances in our solar system more precisely using the parallax method. Nowadays, a Venus transit can yield further information about the constituents and conditions of its atmosphere by means of spectroscopy. This is also a very good test case for similar investigations of atmospheres of transiting extrasolar planets, a technique which is already possible today. Moreover, a transit of Venus always causes renewed interest in celestial phenomena not only among amateur astronomers, but also among laypersons, and thus is a good incentive for astronomical outreach.
In the visible wavelength regime, Venus shows only an impenetrable cloud layer with very little structure. Many more details in these clouds can be observed in UV light - nowadays not only by professional Earth-bound telescopes and spacecraft, but even by amateur astronomers who use special UV filters in combination with digital sensors. On the exploration and composition of the atmosphere, including the clouds, see Section 1.2.2. Even though Venus is much closer to the Sun, it actually absorbs less radiation than the Earth due to its high albedo (Taylor (2006)). In the past, this led many people to expect Earth-like conditions on its surface. This notion began to change as early as 1922, when John and Nicholson (1922) reported detecting no trace of oxygen or water vapour in the spectrum of Venus. This was confirmed by measurements of Adams and Dunham (1932), who furthermore found strong indications for the presence of carbon dioxide. In the 1950s, radio telescopes were first used to determine the surface temperature of Venus by measuring its microwave radiation. These measurements resulted in very high temperatures around 600 - 700 K. After these early remote investigations, the general image was clear, namely that Venus is very different from the Earth in terms of its atmospheric composition and temperature, and the past speculations concerning oceans or even alien life on Venus could not be true.

1.1.2 Space missions to Venus

In this section, we will give a general overview of space missions to planet Venus (Williams (2007)). More detailed results will be discussed in the following sections.
Already a few years after the first successful launch of a satellite into Earth orbit (Sputnik 1 in 1957), attempts were made by the USA and the Soviet Union to send space probes to other bodies in our solar system, first to the Moon and later also to other planets. The first flyby at Venus was carried out by the *Venera 1* probe in 1961, which was only a partial success since contact was lost before the on-board instruments could deliver measurement data. *Mariner 2* was the next successful mission, passing by Venus in 1962. It confirmed the previous estimates for surface temperature and pressure. These results also put an end to the debate whether the high measured temperatures could be originating from a different atmospheric layer instead of the surface. Furthermore, *Mariner 2* did

[4]Transits occur in a pattern which repeats every 243 years and consists of a transit in the first and the eighth year, then a gap of 121.5 years, followed by two transits which are again eight years apart, and then a gap of 105.5 years. The next transit will take place in 2012.

not detect any signs of a planetary magnetic field, so that it became apparent that Venus has at most a very weak field, not exceeding a tenth of that of the Earth. *Mariner 2* also discovered the slow retrograde rotation of the planet. After several failed missions to Venus, the *Venera-4* probe successfully descended into the atmosphere (relaying its data to the *Venera-4* main bus which did a fly-by). It measured in-situ values of temperature, pressure, density and atmospheric composition until it ceased to function at an altitude of 25 km. Just two days later, *Mariner 5* passed by Venus. This spacecraft had originally been a back-up for the *Mariner 3 and 4* missions to Mars, and was later slightly modified and sent to Venus, an early analogy to the present *Venus Express* mission. *Mariner 5* was more focused on plasma investigations than previous missions, measuring charged particles and magnetic field amplitudes as well as atmospheric UV emissions. It was the first mission which measured ionospheric properties by means of radio occultation, and found a dense dayside ionosphere as well as the existence of a nightside ionosphere, albeit weaker and more extended (Brace and Kliore (1991)). The following atmospheric probes, *Venera 5 and 6* (1969), were improved versions of *Venera 4* and managed to transmit data during descent down to an altitude of 18 and 10 km, respectively, before they were crushed by the immense pressure. Only a few months later, *Venera 7* successfully landed on the surface of Venus and continued sending data for about 20 minutes, making it the first man-made probe which transmitted data after having landed on another planet. In the following years, the missions became technically more sophisticated, and the *Venera-8* lander (1972) already comprised a gamma-ray spectrometer for the investigation of surface rocks in addition to atmospheric pressure and temperature sensors. During its descent by parachute, *Venera 8* determined wind speeds, and after its successful landing it continued to operate for almost one hour before succumbing to the hostile environment conditions. It found uranium, thorium and potassium in similar amounts to those present in basalt rocks on the Earth. This confirmed the hypothesis that Venus formed in a way similar to the other terrestrial planets and the Earth's moon, which all have a basaltic crust (Taylor (2006)). In spite of the thick cloud cover, the *Venera-8* descent probe found that the lower atmosphere is rather clear, and with the built-in light sensors it could show that the amount of light on the surface is sufficient for photography, similar to a cloudy day on Earth. In 1974, *Mariner 10*, a combined Venus-Mercury mission, did a swing-by at Venus on its way to Mercury, the first time ever that this kind of manoeuvre was conducted. When approaching Venus, the spacecraft investigated its plasma environment as well as atmospheric circulation patterns. The successful *Venera* program was continued with *Venera 9 and 10* in the following year, which each consisted of an orbiter and a descent probe. While the orbiters investigated the atmosphere and clouds from above by means of different spectrometers, the landers determined in-situ cloud layer thicknesses and altitudes as well as atmospheric constituents. On the surface, they photographed their surroundings. Because they had landed about 2200 km apart, they observed different kinds of terrains. Whereas *Venera 9* photographed several non-eroded rocks with diameters around 30 - 40 cm, *Venera 10* saw large pancake-like lava rocks with some eroded stones in between. From 1978 to 1992, the long-lasting *Pioneer-Venus* spacecraft was in orbit around Venus. It carried various instruments, investigating the plasma environment, imaging the surface with radar, recording IR and UV emissions from the atmosphere, conducting radio-science and radio-occultation experiments and many more. Further details on this mission will be given in Section 1.1.3.1. In addition

to the orbiter, there was the so-called *Pioneer Venus Multiprobe* which comprised a main bus, a large atmospheric probe and three small descent modules. To get a more global picture of atmospheric dynamics, the probes were sent into different regions. They investigated the atmosphere in detail, measuring its composition, cloud particle sizes and shapes, solar flux penetration and radiative energy distribution. In 1978, the *Venera 11* and *12* landers reached the surface after they had further studied the atmospheric composition during their descent. After their soft landing, they also investigated the composition of the soil. The exploration of the surface continued with the landers of *Venera 13* and *14* (1981), which were even equipped with drills which took samples of the surface, after which the on-board X-ray fluorescence spectrometer was used to examine their composition. In 1983, the twin spacecraft *Venera 15 and 16* were inserted into nearly polar orbits around Venus. Their task was to map the surface by means of radar, since radio waves are able to penetrate the thick cloud layer of Venus. They reached an unprecedented surface resolution of 1 m (Taylor (2006)). These were the last spacecraft of the large *Venera* series up to today. *Vega 1 and 2*, which were launched in 1984, first encountered Venus and dropped their descent probes, and then used the planet for a swing-by to travel to comet Halley. The two landers again investigated the composition of the atmosphere as well as of the surface. Additionally, a balloon with a diameter of 3.4 m was deployed into the atmosphere from each of the landing probes, which transmitted data for almost two Earth days from an altitude of about 50 km until the batteries were exhausted. After a 5-year gap, *Magellan* was the next spacecraft to be inserted into orbit around Venus. It mapped the surface using high-resolution (75 - 120 m) radar, covering 98% of the planet at the end of the mission in 1994 and resolving many small features. Towards the end of the *Magellan* mission, aerobraking was used to lower its orbit and finally, in the so-called "windmill experiment", the physics of Venus' upper atmosphere was investigated. The solar panels of the spacecraft were turned in a way that they would be set into rotation when flying through the thin outer atmosphere, and then the torque needed to keep it from spinning was measured. After *Magellan*, there was a large gap of more than a decade during which no space missions were specifically targeted at Venus. Still, several probes passed by Venus on their way to other planets or comets, and collected valuable data. The first of them was *Galileo* (launched in 1989) on its way to Jupiter, which used Venus for a swing-by manoeuvre. It recorded near-infrared spectra of the planet's nightside, imaging the thermal structure of the hot lower atmosphere. In this way, further conclusions about the variations of atmospheric composition and cloud properties, e.g. particle sizes, could be drawn (Carlson and Taylor (1993)). The *Cassini* spacecraft twice passed by Venus in 1998 and 1999 en route to Saturn. Cassini's plasma instruments detected the bow shock, energetic pickup ions and plasma waves near the planet. The optical instruments also recorded images in different wavelength regimes (Burton et al. (2001)). *Messenger*, on its way to Mercury, encountered Venus twice as well, in 2006 and 2007. At this time, *Venus Express* was already in orbit around the planet. The latter mission will be described extensively in Section 1.1.3.2. The combined observations of Messenger and Venus Express have led to a better knowledge of the Venus foreshock, of the transport of magnetic field into the magnetosphere and also generally of the influence of upstream conditions on the planetary plasma environment (Slavin et al. (2009)). In December 2010, the Japanese *Akatsuki* space probe was supposed to be injected into an orbit around Venus. It carries five cameras operating in different wavelength regimes to investigate various phenomena

occurring at Venus, including atmospheric processes and lightning. Unfortunately, the orbit insertion failed and *Akatsuki* is now in an orbit around the Sun. If its batteries last long enough, there will however be another possibility to enter into an orbit around Venus in 2016.

1.1.3 Long-term missions to Venus (PVO and VEX)

Up to now, there have been two spacecraft which continuously investigated Venus over a time range of several years, namely the Pioneer Venus Orbiter (PVO, 1978 - 1992) and Venus Express (VEX, 2006 - now). In this section we will describe their orbital characteristics, instrumentation, and mission objectives.

1.1.3.1 Pioneer Venus Orbiter

The objectives of this NASA mission were the investigation of the surface, upper atmosphere and plasma environment of Venus. Therefore it was equipped with the following instruments (Colin and Hall (1977), Bauer et al. (1977)):

- Neutral Mass Spectrometer (ONMS)
  This instrument determined in-situ density and composition of the upper atmosphere (down to 150 km) for atoms and molecules with masses between 1 and 46 amu.

- Ion Mass Spectrometer (OIMS)
  This ionospheric analyzer measured upper atmospheric ions with masses between 1 and 60 amu.

- Retarding Potential Analyzer (ORPA)
  This sensor recorded temperatures, densities and velocities of ions as well as photoelectron energies and densities.

- Electron Temperature Probe (OETP)
  The OETP analyzed the cold plasma component in the environment of Venus and furthermore, it determined electron densities and temperatures.

- Ultraviolet Spectrometer (OUVS) for the observation of the Venusian airglow

- Solar Wind Plasma Analyzer (OPA)
  This instrument was constructed for the analysis of the three-dimensional distribution of hot ions (50 - 8000 eV) as well as electrons (1 - 500 eV).

- Magnetometer (OMAG) for the measurement of planetary and interplanetary magnetic fields

- Infrared Radiometer (OIR) for the determination of the temperature in one layer of the ionosphere

- Cloud Photopolarimeter/Imager (OCPP)

- Radar Altimeter (ORAD)
- Electric Field Detector (OEFD)
- Gamma Burst Detector (OGBD)

In addition to the measurements conducted by the instruments described above, perturbations of the spacecraft orbit were measured and used to investigate the planetary gravitational field (Colin and Hall (1977)).
PVO was launched in May 1978 and inserted into Venus orbit on December 4, 1978. Its orbit was highly elliptical with a period of 24 hours. This configuration allowed a coverage of the complete surface, since Venus with its long rotation period slowly turned below the spacecraft trajectory. PVO's orbital parameters varied throughout the mission. At the beginning, the periapsis was located only 150 km above the surface and occurred at a northern latitude of 17°. This orbit was kept for 19 months, until the necessity arose to increase the periapsis altitude due to fuel limitations. Until 1986, it moved up to more than 2000 km, before it slowly decreased again towards the end of the mission in 1992 (Brace and Kliore (1991)). Due to the orbital configuration of PVO, in-situ dayside ionospheric

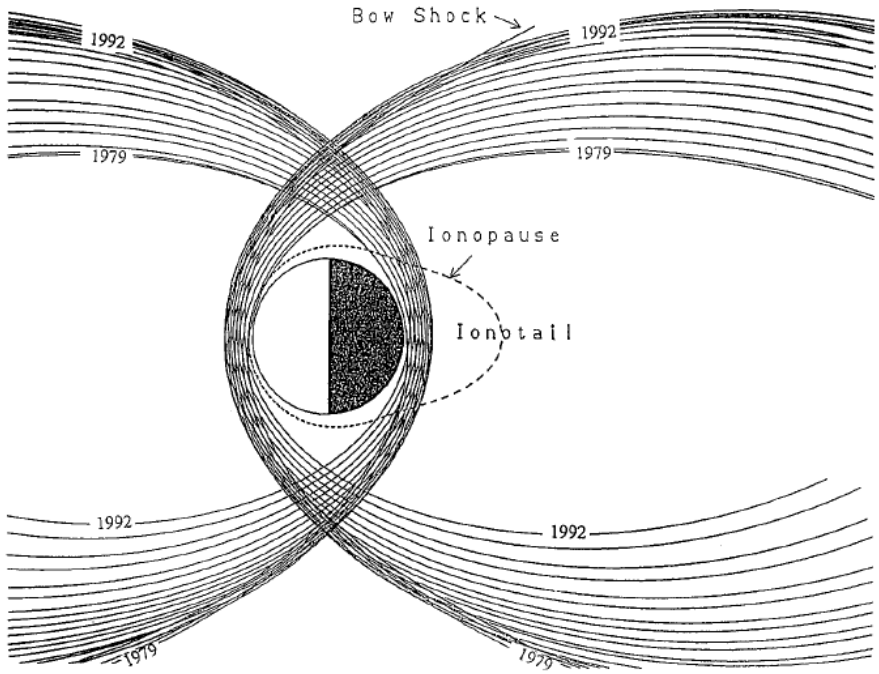

Figure 1.2: The evolution of the PVO orbit during the whole mission time (Brace and Kliore (1991)).

measurements were only possible during the first two years, which fell into the time of solar maximum, and again towards the end of the mission. The whole region covered during the PVO mission is displayed in Figure 1.2, which shows two orbits for each Venus year. The PVO orbit had a constant inclination with respect to the Venus orbital plane, and was precessing at a period of one Venus year with a low-latitude periapsis. Therefore the

spacecraft could observe the dayside as well as the nightside from close-up. In the time of low periapsis at the beginning of the mission, the sharply bounded dayside ionosphere could be covered quite thoroughly, while the nightside ionosphere (or ionotail) is much more extended. Therefore the latter could not be investigated fully, but still the lower region and the far tail were covered.

1.1.3.2 Venus Express

This ESA mission was constructed on the heritage of the Mars Express spacecraft. The main objectives of VEX are the investigation of atmospheric dynamics, the cloud system, the chemical state of the atmosphere, particle escape mechanisms, surface structures and surface composition, and geologic processes on Venus. Since the general design of Mars Express, together with most of the instruments, could be used, VEX could be launched already three years after the mission was approved. The instrument package differs slightly from Mars Express, since some of the sensors had to be adapted to the harsher environment near Venus, and a few instruments, partially coming from the Rosetta mission, were added (Svedhem et al. (2009)). VEX was launched in November 2005 and was injected into orbit around Venus in May 2006. It is on a highly elliptical trajectory with a periapsis between about 170 and 400 km altitude which is located near the north pole. Figure 1.3 shows a sample sketch of one orbit, where the numbers given are the hours. The orbit duration was chosen as 24 hours to facilitate data management on Earth. Figure 1.4 illustrates the spatial coverage reached by Venus Express. While originally the mission was planned for three years, it has recently been extended up to 2014.

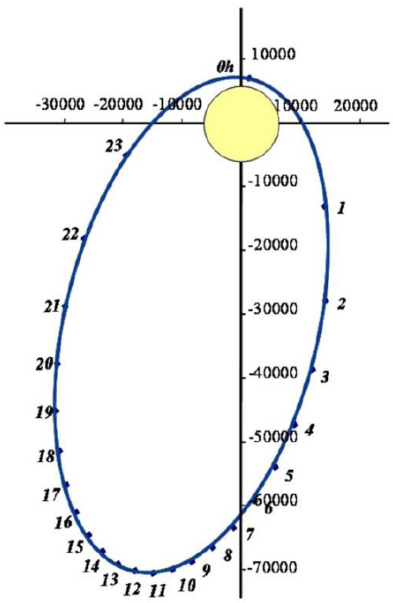

Figure 1.3: The nominal orbit of Venus Express (Svedhem et al. (2009)). The Sun is on the right-hand side and the positive y axis points northward, normal to the orbital plane of Venus.

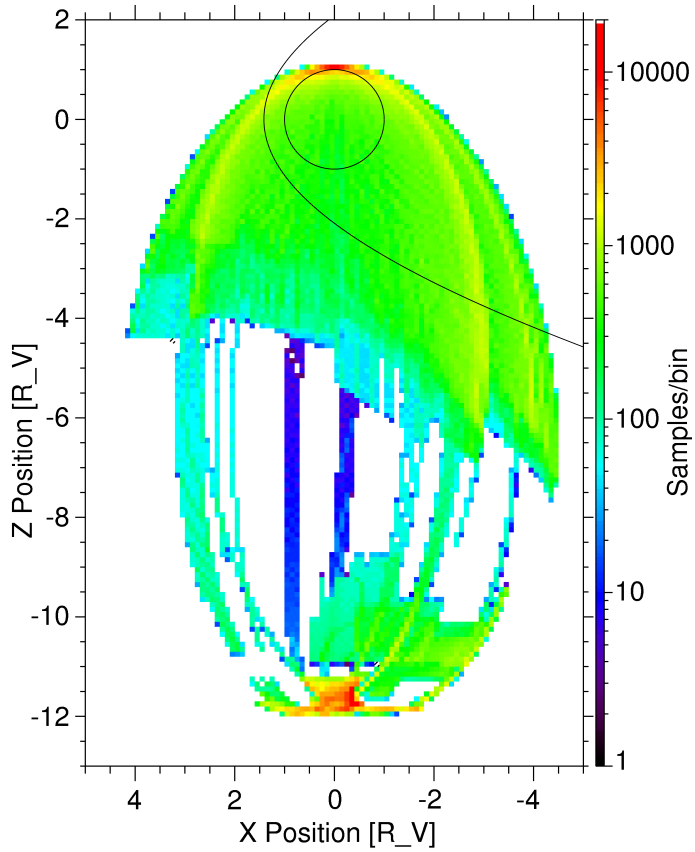

Figure 1.4: The spatial coverage of the ELS instrument from May 2006 to August 2010. The Sun is on the left-hand side, and the y axis (indicated as "Z Position") points northward, out of the orbital plane of Venus. The circle corresponds to the surface of Venus and the hyperbola represents the average bow shock position. R_V on the axes stands for Venus radii. The colours indicate how often a particular bin has been crossed by VEX while ELS was operating. In this figure, the spatial limitations due to the orbit of VEX become visible. But on the other hand, the ionosphere can be probed at a large range of altitudes and latitudes in this orbital configuration. Moreover, the coverage is especially good not only around the apoapsis, but also at the periapsis, which usually is located near and inside the ionosphere.

Overall, VEX comprises the following instrument packages (Barabash et al. (2007b), Svedhem et al. (2009)):

- SPICAV/SOIR (Spectroscopy for the Investigation of the Characteristics of the Atmosphere of Venus/Ultraviolet and Infrared Atmospheric Spectrometer)
  This is a package consisting of three spectrometers for the observation of thermal profiles and the composition of the upper atmosphere. The spectrometers cover the wavelengths between 110 - 310 nm, 0.7 - 1.7 μm and 2.2 - 4.4 μm. Two of the three spectrometers are identical to those on the Mars Express mission.

- VIRTIS (Visible and Infrared Thermal Imaging Spectrometer)
  VIRTIS also consists of three spectrometers, one at visible wavelengths (0.27 -

1.1 μm) and two within the infrared range (1.05 - 5.2 μm and 1.8 - 5 μm, where the latter has a higher resolution). The first two spectrometers are called VIRTIS-M, while the high-resolution spectrometer is named VIRTIS-H. The VIRTIS instrument is identical to the one on the Rosetta mission.

- VMC (Venus Monitoring Camera)
  This camera operates in four channels, each of them with a very narrow wavelength range. One of them lies in the ultraviolet, at 365 nm, where the structure of the cloud tops on the dayside becomes visible. Two wavelength bands lie in the visible and near-infrared, at 513 and 965 nm, and are targeted at the observation of O_2 emission and possibly absorption by water vapour. The fourth band is even further in the infrared, at 1 μm, where the general dayside surface brightness can be observed.

- PFS (Planetary Fourier Spectrometer)
  This is a two-channel spectrometer (0.9 - 5.5 μm and 5.5 - 45 μm) designed for the investigation of the temperature of the surface and the upper cloud layer as well as gas abundances. It is identical to the spectrometer on Mars Express. Unfortunately, an internal mirror got stuck so that the VEX PFS is pointing at a calibration target and cannot be used for observations.

- VeRa (Venus Radio-Science Experiment)
  VeRa mainly utilizes radio occultations to derive density profiles of the neutral atmosphere, as well as profiles of temperature and pressure, focusing on the altitude range between 40 and 90 km. With this method, VeRa can also measure electron densities and therefore detect the structure of the ionosphere (including the main density peak) and its upper boundary, the ionopause. Besides the radio occultations, the radar reflectivity of the surface is investigated by a technique named *bistatic radar*, in which the VEX main antenna sends a signal to the surface at an oblique angle. This signal is then reflected from the surface and received on Earth, providing information about surface structure and possibly also materials.

- MAG (Magnetometer)
  The magnetometer on Venus Express is mounted on a boom that has a length of 1 m. It consists of a main sensor at the tip of this boom and a second sensor at its bottom, both of which are triaxial fluxgate magnetometers. This configuration helps to remove effects of spacecraft charging from the magnetic field data, resulting in a measurement accuracy of about 1 nT (Zhang et al. (2008b)). Magnetic field measurements yield information about a wide variety of processes, ranging from lightning on Venus to the IMF configuration and plasma boundary locations. The investigation of the induced magnetosphere is one of the key goals of this instrument, since many of the effects occurring within this region are still poorly understood.

- ASPERA-4 (Analyzer of Space Plasmas and Energetic Atoms)
  This plasma package is a replica of ASPERA-3 on Mars Express and addresses many open questions concerning the interaction of the solar wind with the atmosphere and ionosphere of Venus. By measuring charged particles and energetic

neutral atoms (ENAs), it characterizes the neutral gas and plasma environment. ASPERA-4 consists of the following four sensors:

- NPI (Neutral Particle Imager)
  This sensor measures ENAs with high angular resolution, but does not separate these by mass and energy. The energy range of the detector lies within 0.1 - 60 keV and particles can be recorded within a field of view of $9° \times 344°$.
- NPD (Neutral Particle Detector)
  This sensor complements the NPI measurements by determining masses and energies of incoming ENAs, which enables it to distinguish H and O atoms. It has an intrinsic field of view of $9° \times 180°$ and an energy range from 0.1 to 10 keV with an energy resolution of $\Delta E/E = 0.8$.
- ELS (Electron Spectrometer)
  ELS is a top-hat electrostatic analyzer that has a high energy resolution of $\Delta E/E = 0.07$ within 0.01 - 20 keV/q. Figure 1.5 shows the basic principle of the ELS sensor. Electrons can enter within the region indicated in black, allowing for a field of view of 360° in the plane of the two parallel top-hat plates. In the direction perpendicular to this plane, the field of view depends on the opening angle of the set-up; in the case of ELS, it is 4°. Electrons entering between the parallel plates will then proceed between the two spherical plates, where a voltage is applied which filters incoming particles in energy and only lets them pass for certain values of mv^2/q. Eventually, the electrons are registered by a detector, which in the case of ELS is a micro-channel plate (MCP).
  Figure 1.6 shows a sketch of the ELS instrument. The top-hat analyzer structure, as it was described above, is clearly recognizable, with the two spherical voltage plates visible as a grey hemisphere. In order to get a full energy spectrum, the voltage of the spherical analyzer plates is varied in 128 steps within four seconds, thereby sweeping through the full energy range. (Sometimes, the time resolution is even set to one second, but then only a smaller energy range can be sampled.) The actual detection of the electrons takes place in 16 anodes which are located behind the MCP, which means that each anode covers an angle of 22.5°. Since ELS is insensitive to UV light, it can operate even when pointing directly towards the Sun. In addition to two UV suppression mechanisms, a special coating inside the ELS reduces the secondary electrons produced by the interaction of UV light with the charged spacecraft. Still, the number of these secondary electrons is large enough to saturate the sensor. In order to avoid this, a negative voltage of about 5 V is applied. This means that no ionospheric electrons below an energy of 5 eV can be detected (see also Coates et al. (2008)). In the meantime, it turned out that during ionospheric crossings, the spacecraft acquires a negative potential which is sufficient to repel electrons below 5 eV, and thus an additional negative voltage is not needed any more. One problem of the ASPERA-4 ELS is the fact that the symmetry axes of its spherical deflection plates have a certain offset, which induces an asymmetry in the measurements that has to be taken into account.
- IMA (Ion Mass Analyzer)

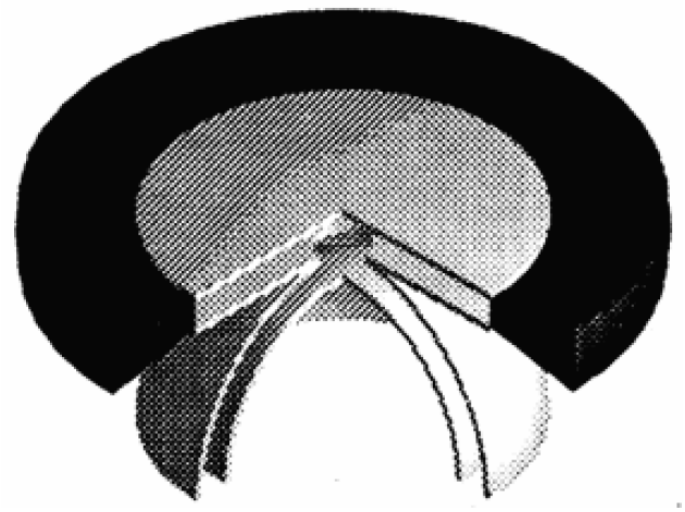

Figure 1.5: The basic configuration of a top-hat electrostatic analyzer (Funsten and McComas (1998)).

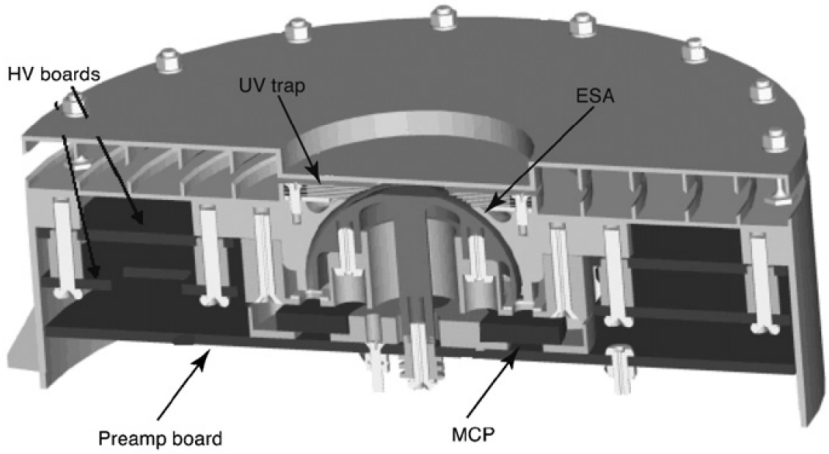

Figure 1.6: The configuration of the electron spectrometer (Barabash et al. (2007b)). ESA indicates the electrostatic analyzer, i.e. the pair of spherical plates filtering incoming electrons in energy.

This instrument is a twin of the ICA instrument on Rosetta. It has a field of view of $90° \times 360°$, and its energy range lies between 0.01 and 36 keV/q with a resolution of $\Delta E/E = 0.07$. IMA can resolve ions such as H^+, He^+ and He^{++} as well as ions with m/q between 20 and 80 amu/q, but the mass resolution for heavier ions is poor. Due to the negative spacecraft potential which often occurs, positive ions can be detected even below the energy threshold of IMA in many cases.

While NPI, NPD and ELS are accommodated within the main unit of ASPERA on a scanning platform, IMA is placed separately. For a full 3D scan, the main unit instruments usually take 32 seconds, which corresponds to one full rotation of the

scanning platform (sometimes this value is increased to 64 or 128 s). IMA, on the other hand, uses electrostatic sweeping and reaches a temporal resolution of 192 s. Although in theory, most instruments on the platform can achieve a full 4π coverage due to the scanning mode, in reality the spacecraft often blocks part of the field of view. This leads to many difficulties in the calibration and analysis of the data since the complex shape of the spacecraft has to be taken into account when compensating for this blocking. Figure 1.7 shows the locations of the different sensors on the main unit (left-hand side) as well as the configuration of IMA (right-hand side).

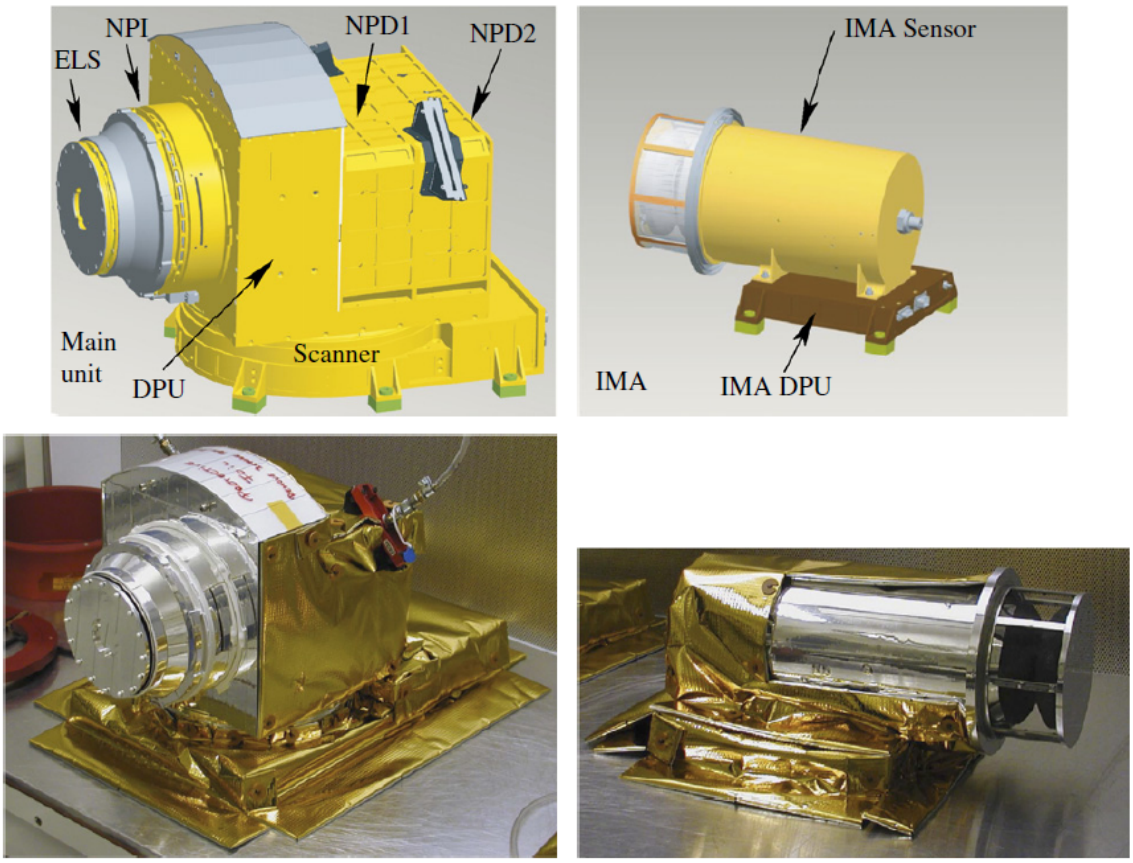

Figure 1.7: The locations of NPI, NPD and ELS on the ASPERA-4 main unit and the configuration of the ion mass analyzer (Barabash et al. (2007b)). DPU stands for Digital Processing Unit.

An overview of the fields of view for the different spectrometers is given in Figure 1.8. The ranges are projected on an UV image of Venus taken by VMC and scaled to a distance of 20,000 km from the planet, which is roughly 1/3 of the apoapsis distance. At apoapsis, the field of view of VMC comprises more than the full planetary disk, while VIRTIS-M covers one third of the planet's angular diameter in this case. Figure 1.9 illustrates the accommodation of the instruments on the VEX spacecraft.

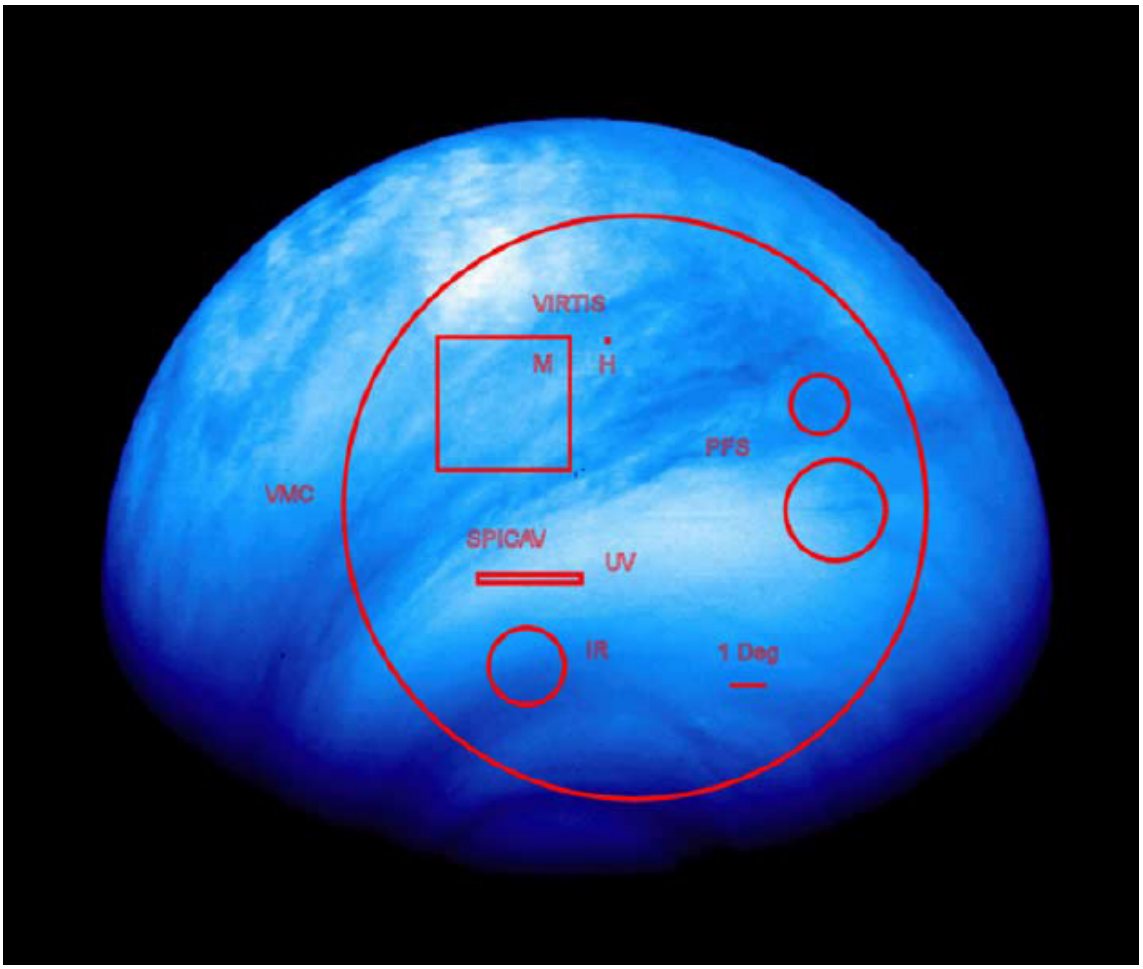

Figure 1.8: The fields of view of the different spectrometers for a distance of 20,000 km from Venus (Svedhem et al. (2009)).

1.2 Planet Venus

Venus is thought to have formed in a similar manner to the other terrestrial planets of our solar system, namely by accretion from planetesimals that contained large amounts of iron and silicate. From seismic measurements on the Earth, we know that our home planet has differentiated into an iron-rich core which makes up about half of its radius, and a crust that is rich in silicates. The core itself consists of a solid inner and a liquid outer core. These detailed measurements have not been conducted on Venus up to the present day, but its bulk density is close to that of the Earth. This means that Venus very probably has a similar internal structure as planet Earth, even though its core might be completely solid.

1.2.1 Surface and geology

The *Magellan* orbiter found that Venus is geologically very different from the Earth, showing no plate tectonics, but strong volcanism. Most of the surface exhibits very little vari-

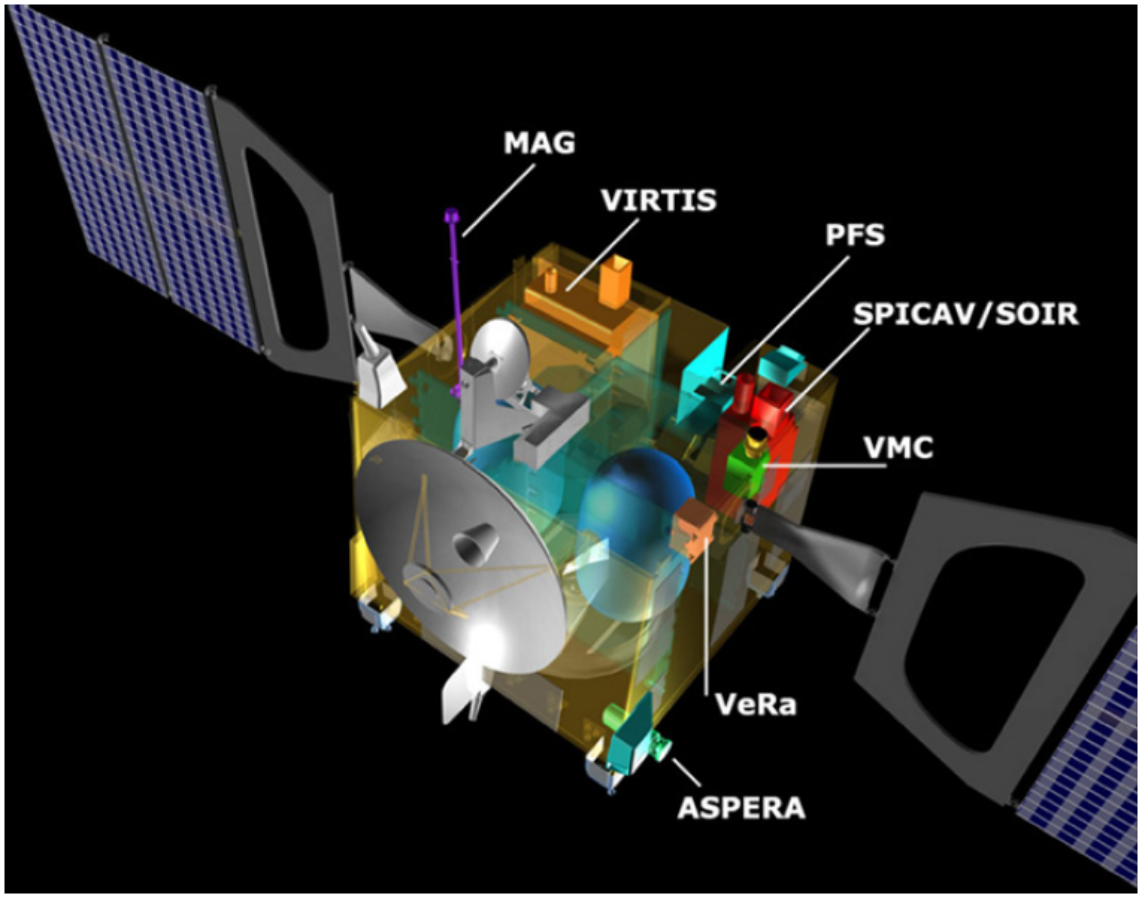

Figure 1.9: The location of the instruments on Venus Express (Svedhem et al. (2007a)).

ations in altitude and seems to be covered by hardened volcanic flows. There are some lowland regions ("Planitiae", about 20% of the total surface), flat plains (70%), and 10% of the surface are taken up by the so-called "terrae", the highlands, as can be seen in Figure 1.10. The terrae show a very interesting feature: every formation higher than 2 km above the mean surface of the planet appears surprisingly bright in radar images. The reason for this must be a thin cover of a material which condenses at these altitudes under Venus conditions. It is still unclear which material this could be; guesses include compound iron pyrites, tellurium or mixtures of lead and bismuth sulphides (Taylor (2006)). Several large shield volcanoes, as well as smaller volcanoes with different shapes, were discovered in the Magellan radar images, which confirms the assumption of volcanism being the main surface-shaping process. Erosion is very weak, making the determination of the age of surface features quite difficult. Even impact craters can hardly be used as an indicator, since the thick atmosphere only permits larger meteorites to reach the surface. Moreover, there are rather few craters, which shows that all of the planet's surface must be geologically rather young and was probably simultaneously covered by volcanic flows everywhere ("global resurfacing") about 500 million years ago. This prevents access to the further geologic history of Venus. It also seems as if geological processes like volcanism and tectonic deformation have been very weak since the global resurfacing event, because most observed craters have hardly undergone any modifications since they were

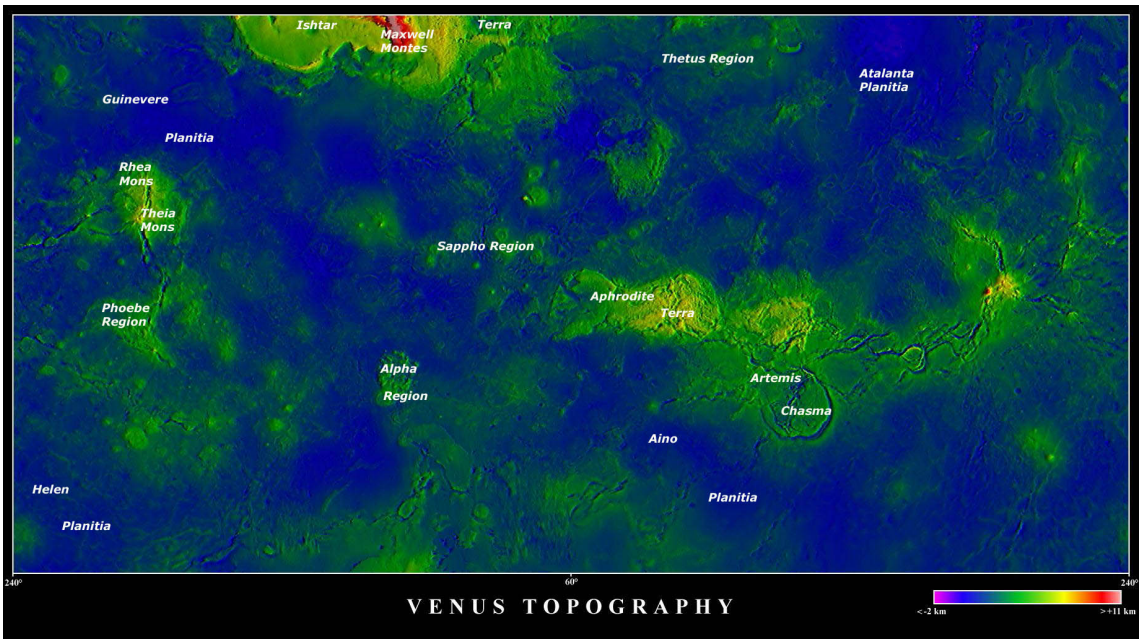

Figure 1.10: The surface of Venus, as investigated by radar measurements (© A. Tayfun Oner). Colours indicate the altitude of surface features.

created (Solomon (1997)). Surprisingly, there are some surface features which look like river beds and deep valleys. These must be due to liquids flowing on the surface. Assuming constant atmospheric conditions on Venus, these liquids could have been minerals like carbonatite, or even lead or tin (Taylor (2006)). An interesting question is whether some of these liquids are still present, maybe flowing underground, or otherwise why they disappeared.

Two surface images of the Venera landers are shown in Figure 1.11. They display strikingly different geological formations, the upper image showing a younger landscape with rocks which are probably fragments of hardened lava flows, while the region in the bottom image contains finer grains and looks much older. The processes which formed these surface structures are still a mystery, since erosion as known from planet Earth is hardly possible on Venus. There is neither liquid water, nor atmospheric water which could contribute to erosion, and the temperature is nearly constant everywhere, independent of seasons or local time. Some more fascinating pictures of this intriguingly variable planetary surface can be found in Solomon (1997).

Presently, Venus does not have any measurable intrinsic magnetic field. PVO measurements led to the conclusion of an upper limit of 10^{-5} times the field of the Earth (Luhmann and Russell (1997)). If one assumes that Venus was accreted similarly to the Earth, it must have possessed an intrinsic magnetic field at least for some time. A planetary dynamo requires a conducting liquid core, convection, and rotation. Even though the rotational period of Venus is rather long, this factor alone cannot explain the lack of a magnetic field (Luhmann and Russell (1997)). This means that there is probably either a general lack of convection in the core, or the core of Venus is already completely solidified. Up to the present day, it is not clear which of these factors applies or whether it is a combination

of both. Nimmo (2002) proposed a connection between the lack of plate tectonics and the missing dynamo effect. He explains that convection can be either thermal or compositional, whereas the latter process is driven by the solidification of the core. While the Earth loses most of its internal heat flux via plate tectonics, this loss mechanism is not possible for Venus. Therefore the loss of heat from the core is so small that no dynamo is created. The possibilities for investigation of the history of the Venusian magnetic field are severely hampered by the fact that the surface temperature is higher than the Curie point for most materials present; therefore no remanent crustal magnetic fields can be found.

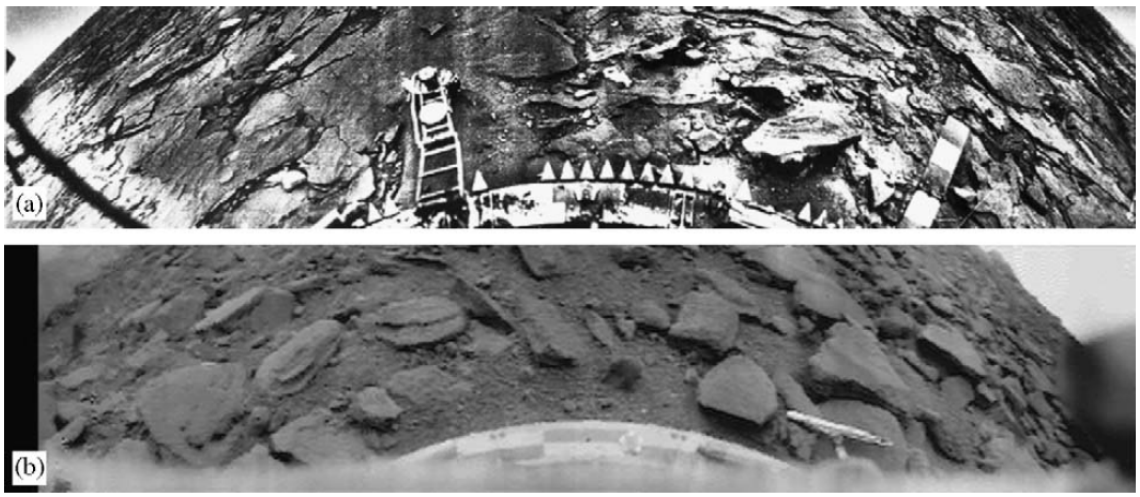

Figure 1.11: Surface photographs taken by Venera 14 (top panel) and Venera 9 (bottom panel) (Taylor (2006)).

1.2.2 Atmosphere

1.2.2.1 Composition

The atmosphere of Venus is radically different from that of the Earth. Its main features are summarized in Table 1.3.

While the atmosphere of Venus contains hardly any water nowadays, it is assumed to have had a similar water inventory to our Earth in the past. During their accretion phase, the terrestrial protoplanets did not contain large amounts of water because the temperature in this part of the solar system was too high. Instead, water was brought later by planetary embryos from the outer solar system, and also (at a smaller rate) by comets. The assumption that Venus was similarly water-rich as the Earth in the past is supported by the fact that the D/H ratio on Venus is more than 100 times higher than on Earth (Grinspoon (1993)). The loss of water on Venus has been an open question for a long time, since simple thermal escape of hydrogen and oxygen is by far not sufficient to explain it. The key to this problem are probably two mechanisms. The first one is the escape of neutral

Surface pressure:	92 bars
Surface density:	~65 kg/m^3
Scale height:	15.9 km
Total mass of atmosphere:	~4.8 x 10^{20} kg
Average temperature:	737 K (464 °C)
Diurnal temperature range:	~0
Wind speeds:	0.3 to 1.0 m/s (surface)
Mean molecular weight:	43.45 g/mole
Atmospheric composition (near surface, by volume):	Major: 96.5% Carbon Dioxide (CO_2), 3.5% Nitrogen (N_2) Minor (ppm): Sulfur Dioxide (SO_2) - 150; Argon (Ar) - 70; Water (H_2O) - 20; Carbon Monoxide (CO) - 17; Helium (He) - 12; Neon (Ne) - 7

Table 1.3: Atmospheric parameters of Venus (Taylor (2006))

atoms and molecules by collisions with hot atoms near and in the ionosphere, and the second is the erosion of ions by the solar wind. Barabash et al. (2007a) report significant escape via the latter mechanism for O^+, He^+ and also H^+. Using VEX ASPERA-4 data, they could for the first time determine exact loss rates. The escape of H^+ was found to be 1.9 times higher than the escape rate for O^+, which means that the ratio of escape rates is very close to the stoichiometric ratio for water (2:1). When escape of atoms is included, the total ratio of loss rates is found to be 2.2:1 (H/O). This is still very close to the expected ratio for water. An explanation for the slightly too high loss rate of H^+ observed by ASPERA-4 is that a part of these ions is of solar wind origin and does not come from the planet's atmosphere. A large amount of water loss is also assumed to have happened during the early time of the solar system, since the young Sun produced more EUV radiation and a stronger solar wind (Kulikov et al. (2006)).

Due to its high albedo, the calculated black-body temperature on Venus is only 232 K, as opposed to 254 K for the Earth (see Table 1.1). These surface temperatures would be found if the planets had no atmosphere and the temperature was constant everywhere on the surface. In reality, the temperatures are higher than this theoretical value due to heating by the so-called greenhouse effect. On Earth, the equilibrium surface temperature is about 34 K higher than the black-body temperature, mainly due to carbon dioxide, but also other greenhouse agents like water vapour or methane. This topic has been under discussion especially in the last few years, since the CO_2 content of the Earth's atmosphere increases significantly due to human influence, which affects our climate. On Venus with its heavy CO_2 atmosphere, the greenhouse effect assumes much more extreme proportions, leading to a surface temperature that is about 500 K higher than the pure black-body equilibrium temperature. Generally the temperature settles at a value for which the incoming short-wavelength solar energy is balanced by infrared cooling. PVO measurements already confirmed that this is the case for Venus. If significant amounts of water were present in the past, they probably even contributed to the greenhouse effect since they could only exist in the form of vapour due to the high temperatures. This water vapour in turn intensified the greenhouse effect and led to even stronger heating of the atmosphere, a so-called runaway greenhouse effect.

A new theory on the history of the water in relation to the geological history of Venus was

presented by Gillmann et al. (2009). The authors start from the assumption that Venus was initially endowed with an amount of water equal to 5 terrestrial oceans (TO), provided by planetary embryos. The Earth itself probably had about 15 TO of water in its early phase. On Venus, due to its proximity to the Sun, all of the initially present hydrogen from the water was then removed by hydrodynamic escape, dragging most of the oxygen away with it. This process led to a dense O_2 atmosphere. However, since the surface still consisted of liquid magma at this time, the O_2 was taken up by the magma due to oxidation of iron. The magma ocean then started to crystallize, much earlier than this was the case on Earth. In this process, large amounts of CO_2 were released from the hardening magma, rapidly changing the composition of the atmosphere. In the period between 100 - 500 Myr after the formation of the planet, about 0.1 TO of water were delivered again by comets. Just like before, the hydrogen contained in the water escaped hydrodynamically, leaving some of the oxygen behind which formed an oxygen atmosphere once more, albeit much less dense than the previous one. The now solid surface took up most of the O_2 by oxidation of iron, especially during volcanic outbursts, a mechanism that is still continuing even today. The remainder of these processes was an amount of water that is estimated not to exceed 10^{-3} TO, which was then gradually lost to space by pick-up ion escape, creating the observed high D/H ratio at Venus and leaving behind only a dense CO_2 atmosphere.
The advantage of this theory by Gillmann et al. (2009) is that it explains the present ratios of neon and argon isotopes found at Venus. An interesting fact resulting from their ideas is that Venus had a very dense oxygen atmosphere for some time in its history. When seen from far away, it would be regarded as a very probable candidate for a habitable planet, even though this is not the case. Thus it is an instructive example that has to be kept in mind when searching for extrasolar habitable planets.
The general temperature profile of today's atmosphere of Venus, together with the main cloud and haze layers, is shown in Figure 1.12. Figure 1.13 illustrates the different thermal properties of the atmospheres of Venus, Earth and Mars. Also given are the theoretical black-body temperatures calculated from the balance between incoming solar radiation and reflected or re-emitted energy from the planet. The larger the difference between theoretical and real surface temperature, the stronger the greenhouse effect is. It is also well visible that all three planets display rather similar temperatures at high altitudes (Venus being even colder than the Earth), and the strong increase in temperature at Venus takes place only towards lower altitudes due to its CO_2-rich atmosphere. The temperature of the upper Venusian atmosphere (above about 100 km) displays strong differences of up to 200 K between dayside and nightside. Therefore, the dayside upper atmosphere is called thermosphere, while the same region on the nightside is named the cryosphere.

1.2.2.2 Dynamics

The cloud motion is one of the many unsolved riddles about Venus. The upper cloud deck (at about 50 - 60 km altitude) moves along the equator at velocities around 100 m/s, which is more than 50 times faster than the planetary rotation (this behaviour is named "superrotation"). The process that causes these speeds is still unknown. Towards lower altitudes, due to the strong increase in density, the cloud velocity decreases rapidly down to only a few m/s at the surface (Taylor (2006)). Moreover, on average there are net wind speeds of a few m/s which transport heat from the equator to the poles, both at 60 km

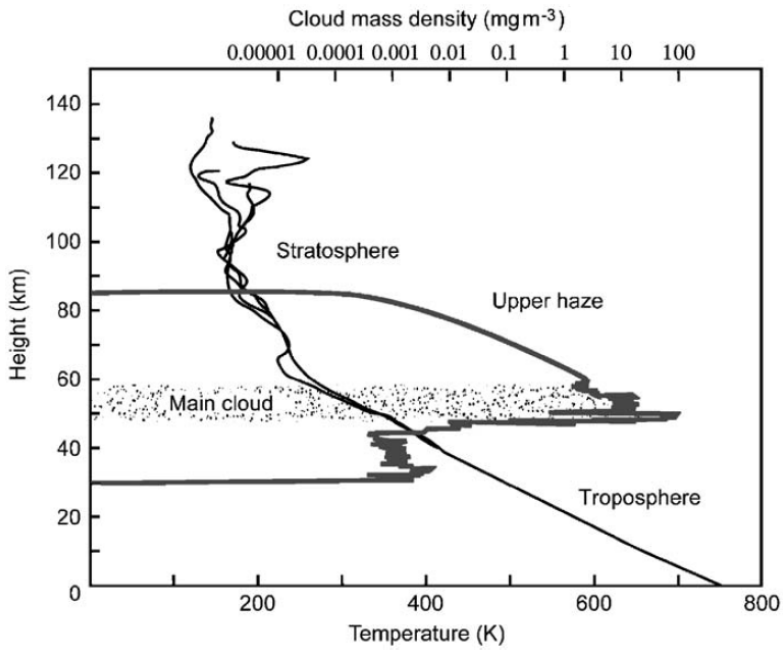

Figure 1.12: The black curve indicates the temperature (given on the bottom scale of the x axis) at different altitudes in the atmosphere of Venus. It starts to increase especially within and below the main cloud deck. The grey curve represents the cloud density (see top scale of x axis). The measurements were taken by the Pioneer Venus Orbiter and Multiprobe (Taylor (2006)).

(cloud tops) and around 45 km altitude (within the main cloud layer). Some basic zonal wind speed profiles can be seen in Figure 1.14. Overall, the cloud dynamics on Venus are very complex and highly structured, with previously unexpected cold regions, polar vortices and many features which still need to be investigated further.

1.2.3 Ionosphere

As solar EUV radiation encounters the dense atmosphere of Venus, it ionizes a large portion of the atoms and molecules, forming a plasma of ions and electrons. The region in which this process dominates is named the ionosphere. It overlaps with the upper parts of the neutral atmosphere (especially the thermosphere), the main ionospheric peak usually being found at an altitude of about 140 km with a typical dayside peak electron density of $5 \cdot 10^5$ cm^{-3} (Shinagawa (2004), Pätzold et al. (2007)). Its lower boundary or base was found to be located near 120 km altitude on the dayside by the VeRa experiment on Venus Express (Pätzold et al. (2007)). The general altitude profile of this plasma region is that of a superposition of two or more Chapman layers, which means that within this region, there is a balance between the production of ions by photoionization and the removal of ions by recombination (Brace and Kliore (1991), for more details see Chapman (1931)). For the Chapman model, the ionosphere is assumed to be isothermal, which is of course not true in reality. Nevertheless, the structure of the Venusian ionosphere can be described

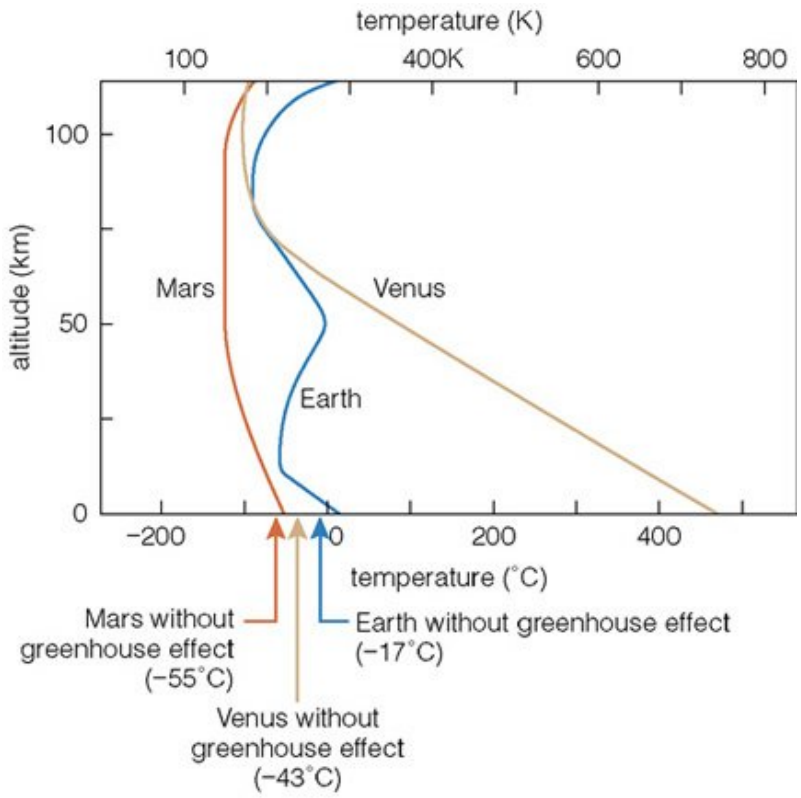

© 2005 Pearson Education, Inc., publishing as Addison Wesley

Figure 1.13: Comparative temperature profiles for Venus, Earth and Mars.

very well by Chapman profiles, even near the terminator[5], as was shown by Fox (2007). This author also modelled the altitude structure and density of the ionosphere for different solar zenith angles[6] between 60 and 90°. Fox (2007) found that the peak densities at different angles agree well with the expected Chapman profile, but the altitude of the peak does not change up to 80°, and even for larger solar zenith angles, it rises only slightly (from 144 km at 85° to 149 km at the terminator). The PVO mission, on the other hand, detected a slight decrease in peak altitude towards the terminator. This deviation from the models is attributed to fluctuations in the thermosphere, as well as a thermospheric temperature decrease with increasing solar zenith angle, so that the theoretical conditions assumed when applying a Chapman function are not true any more.
Due to the high abundance of CO_2, photoionization mainly creates CO_2^+ ions. Below 170 km altitude, these ions react with O in the following way:

$$CO_2^+ + O \rightarrow O_2^+ + CO,$$

making O_2^+ the most common ion in this region. Moreover, ions such as NO^+, N_2^+, CO^+ and CO_2^+ are present in smaller amounts. This composition changes towards higher altitudes, where transport effects play a larger role. Above 200 km, O^+ is the most abundant

[5]The terminator is the boundary between the dayside and nightside of a planet.
[6]For an explanation of the solar zenith angle, see Section 2.1

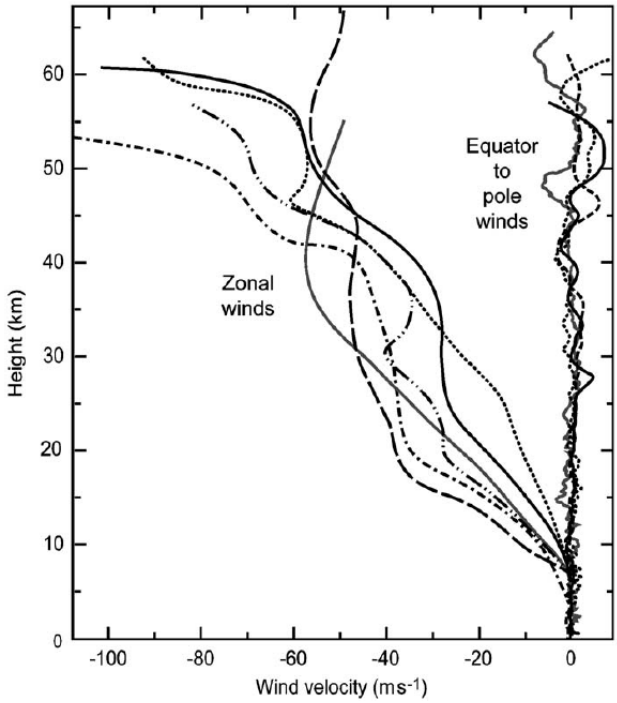

Figure 1.14: Profiles of the atmospheric zonal wind speeds recorded by the Pioneer Venus probes (Taylor (2006)).

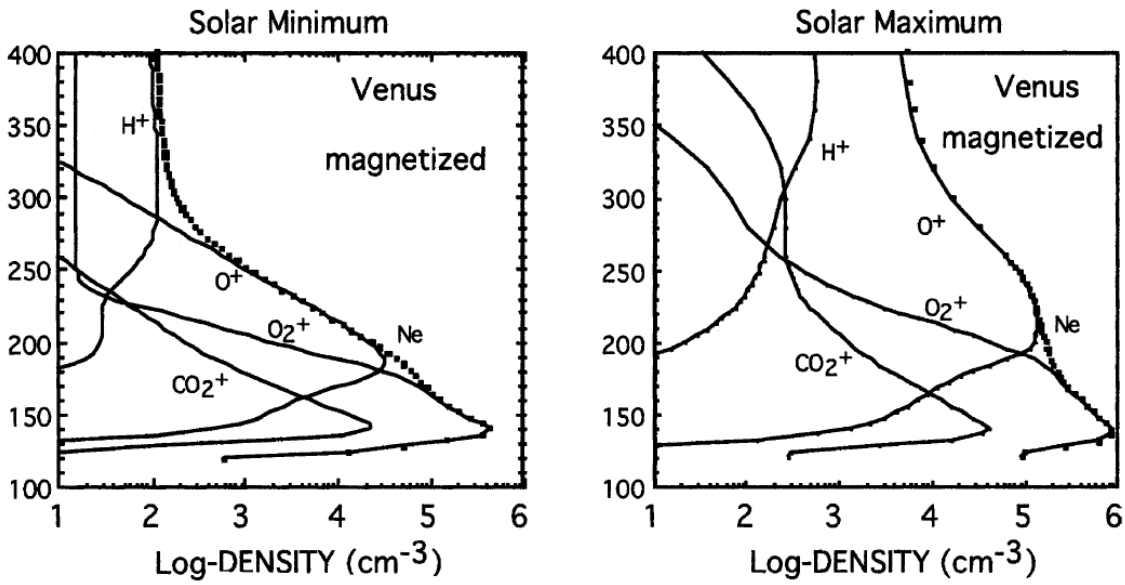

Figure 1.15: Samples of altitude profiles from one-dimensional MHD models (Shinagawa (2004)) for the four major ion species. These profiles were calculated for the case that magnetic field enters the ionosphere of Venus (see Section 1.2.4.3). The left-hand plot is calculated for solar minimum and the one on the right-hand side for solar maximum.

ion (Kar (1996)). According to Fox (2007), large amounts of O^+ are produced especially in the very high- and low-altitude ionospheric regions, but these quickly react with CO_2 to again form O_2^+ within the regions where photochemical equilibrium prevails. Figure 1.15 shows ionospheric altitude profiles for the most abundant ions.
For the investigation of the ionosphere, it is often easier to focus on electrons instead of ions, because the latter have various m/q values. The ability of an instrument to detect particles within this larger range often results in longer sampling times. This is also the case for the ASPERA package on Venus Express, where the temporal resolution of ELS is much higher than that of IMA. Furthermore, electrons themselves do play an important role in ionospheric processes, since they in turn can ionize neutral atoms and molecules or generally lead to heating of the ambient plasma. In Figure 1.16, an electron density profile measured by VeRa is depicted. It consists of two main (Chapman) layers, V1 and V2, and a few additional bulges, some of which cannot yet be explained by models. The lower (V1) peak is actually caused more indirectly, namely by ionization of atoms and molecules by secondary, high-energy photoelectrons ("photoelectron-impact ionization") which themselves have also been created in ionization processes due to soft X-ray photons from the Sun (Fox (2007)). The ionopause, the upper boundary of the ionosphere, is clearly recognizable by a strong decline in electron density at about 260 km.

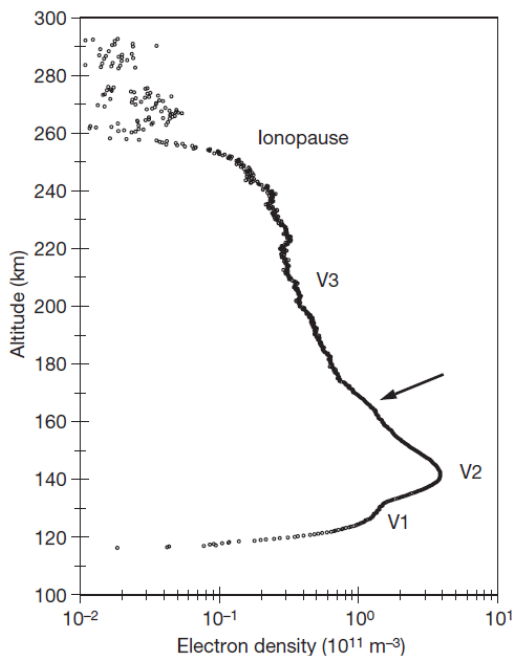

Figure 1.16: A dayside ionospheric profile measured by the VeRa experiment on Venus Express (Pätzold et al. (2007)). In contrast to in-situ instruments, VeRa can determine absolute electron densities.

In Figure 1.17, the general configuration of the ionosphere of Venus is shown. Its scale is expanded by a factor of 2 with respect to the planet and the bow shock. While the creation and maintenance of the dayside ionosphere by solar EUV radiation is rather straightforward, the nightside ionosphere is still not completely understood. Due to the ionospheric

pressure gradient between dayside and nightside, electrons and ions are pushed towards the nightside. There is also a small contribution to the ion population by ionization of atoms by energetic electrons on the nightside of Venus, but the density gradient mechanism plays a more important role (Fox (2008)). Of course, magnetic fields also greatly influence the transport process of charged particles into the nightside hemisphere. The structure of the ionosphere in this region is often very filamentary and in some cases it disappears completely. Some parts of it, the filaments and streamers, extend far into the tail and may even detach from the ionosphere and be swept away along the tail, making them an important possible source for atmospheric loss. Grünwaldt et al. (1997) reported on the detection of Venusian tail rays by the SOHO spacecraft which is located near the Earth's L1 point. At the time when these measurements were taken, SOHO had a distance of $4.5 \cdot 10^7$ km (0.3 AU) from Venus. Firstly, this detection proves that the tail does indeed extend very far behind the planet, and secondly, it is a great possibility to determine the composition of the plasma lost by Venus.

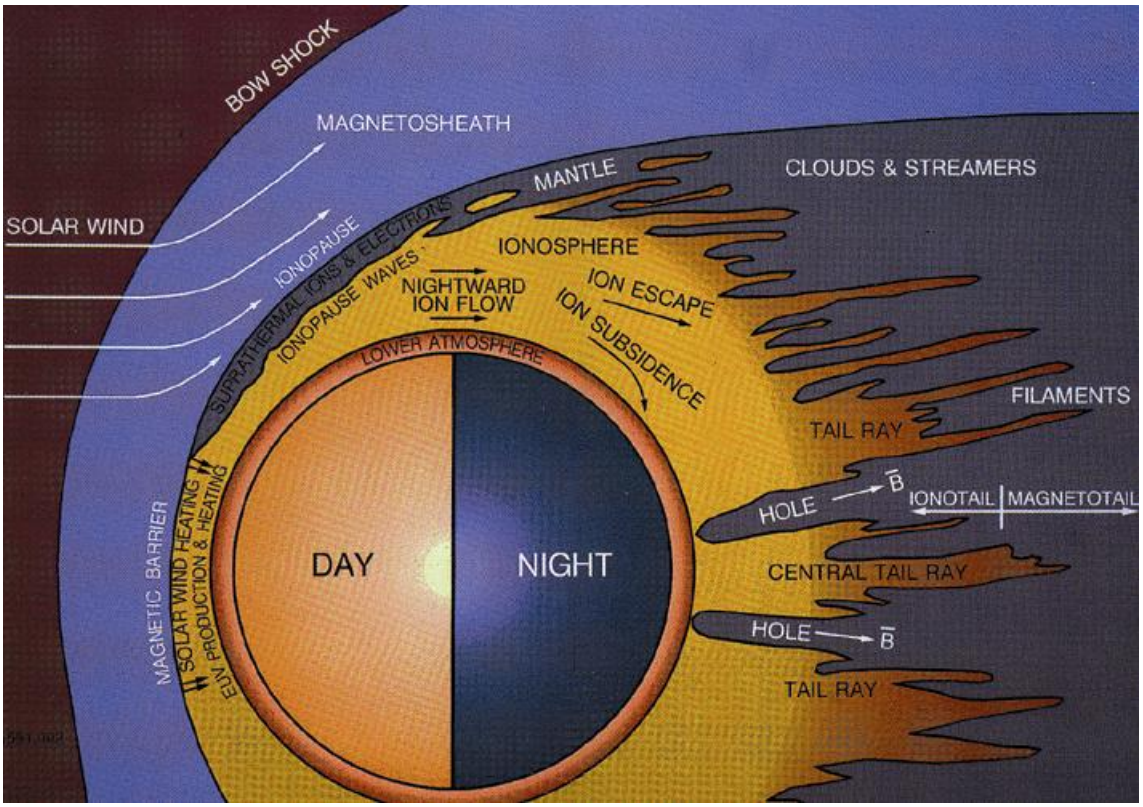

Figure 1.17: A sketch of the most important plasma boundaries and interaction regions in the environment of Venus (Brace and Kliore (1991)).

The varying solar wind conditions provide a highly dynamic environment acting on the atmosphere and ionosphere of Venus. The ionopause forms at an altitude where the external (solar wind) and internal (ionospheric) pressure are equal:

$$n_{\mathrm{SW}} k T_{\mathrm{SW}} + \rho v^2 + B^2/8\pi = n_{\mathrm{iono}} k T_{\mathrm{iono}} \tag{1.1}$$

where n_{SW} denotes the particle number density of the solar wind, k the Boltzmann con-

stant, T_{SW} the temperature of the solar wind, ρ the solar wind particle density, v the solar wind velocity and B the IMF. n_{iono} and T_{iono} are the ionospheric number density and temperature, respectively. The terms in this equation are the solar wind thermal pressure, dynamic pressure, magnetic pressure and the ionospheric thermal pressure. Generally the dynamic pressure is the dominant factor in the solar wind (contributing 98% of the total pressure (Phillips and McComas (1991))), but towards the terminator its component acting radially on the Venus ionosphere decreases so that the other terms will dominate (Brace and Kliore (1991)). As the extent of ionization depends on the intensity of the solar EUV radiation, the internal thermal pressure of the ionosphere is subject to solar variability. Similarly, the dynamic and thermal pressure of the solar wind particles as well as the pressure created by the interplanetary magnetic field depend on the actual solar conditions. If the external pressure contributions are strong or if the ionosphere is weakly developed, the altitude of the ionopause decreases until pressure balance is restored. This is often the case during solar minimum. Near solar maximum, on the other hand, the ionopause is generally located at higher altitudes due to the higher intensity of solar UV radiation. The typical passage time of the solar wind across the magnetosphere lies between 30 and 120 seconds. This means that most of the described influencing factors can change on rather short time scales, although the reaction time of the Venusian plasma environment might be longer. Luhmann et al. (1984) presented a one-dimensional model for the decay of magnetic fields in the ionosphere of Venus, based on diffusion processes and including possible vertical plasma drifts. It relies on simple considerations including the Maxwell equations for the description of the temporal variations of the magnetic field and the momentum equations for the ions and electrons. Furthermore, the authors assumed that the magnetic field in the ionosphere is horizontally orientated and does not vary horizontally, but only in the vertical direction. These equations and assumptions result in an expression for the diffusion time for the field which depends on the collision frequencies between electrons and neutrals as well as between electrons and ions. The vertical motion depends on the vertical drift velocity which is assumed; the authors used various values for this velocity to investigate its influence on the general magnetic field configuration. Keeping the magnetic field amplitude constant at the ionopause as well as at the base of the ionosphere (assumed to be located at about 145 km altitude), magnetic field profiles can then be calculated for varying external field amplitudes and vertical drift velocities. One example is presented in Figure 1.18. Starting from the measured conditions, given by the solid line, the field develops according to the diffusion equations and decays within the few hours shown in this plot. This is only the simplest case; when varying the external field or adding a vertical velocity, realistic conditions can be approached more closely. In Figure 1.19, an additional vertical drift leads to a much faster decay of the magnetic field.

This model successfully explains the typical altitude structure of the magnetic field (see Section 1.2.4.3). It proved more realistic than a model by Cloutier et al. (1981) (see this reference for more details), as was shown in a direct comparison by Luhmann et al. (1987). As was already mentioned when regarding Figures 1.18 and 1.19, the Luhmann et al. (1984) model yields a decay time of ionospheric magnetic fields on the order of a few hours, which may however decrease significantly if the plasma has a non-zero vertical drift velocity. This is an important fact to keep in mind when investigating the statistical properties of ionospheric magnetization states at Venus.

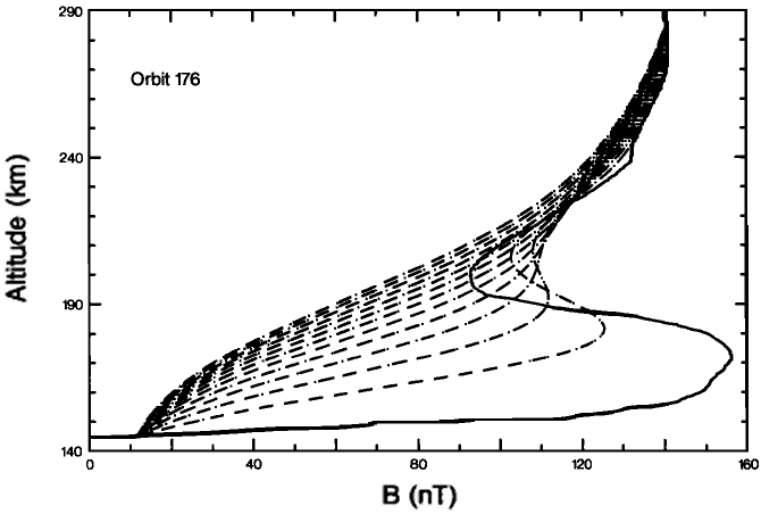

Figure 1.18: A comparison of the measured magnetic field profile on a PVO orbit (solid line) and results of the model by Luhmann et al. (1984) (dashed lines) in intervals of 5000 s, shifting to the left for increasing time. The magnetic field is kept constantly at the measured value at both 145 and 290 km altitude, and the vertical plasma velocity is set to zero.

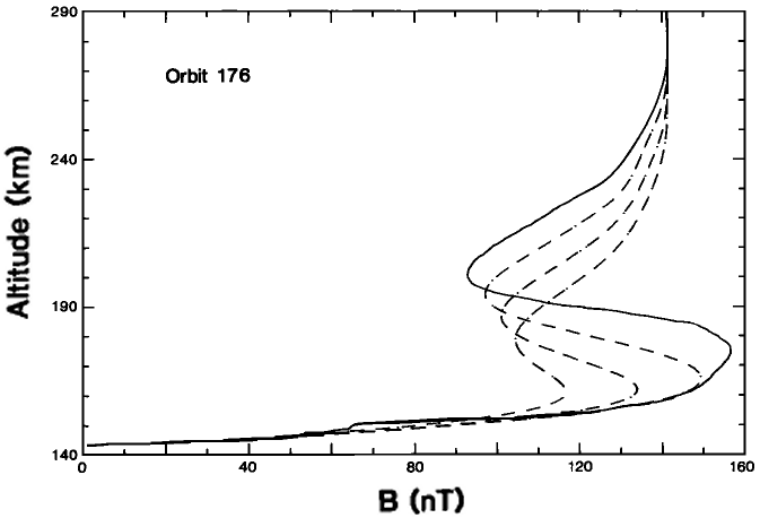

Figure 1.19: The same case as for Figure 1.18, but now with an additional downward plasma drift velocity of 10 m/s. The dashed curves are now shown at time intervals of 1000 s.

1.2.4 Plasma environment

Since Venus does not possess an intrinsic magnetic field, at a first glance it does not have any protection against the incoming solar wind. But one has to take into account that due

to its dense atmosphere which is exposed to solar radiation, a strong ionosphere is formed (see Section 1.2.3), much in the same way as for the Earth. The interaction of charged ionospheric particles with the charged solar wind flow and the interplanetary magnetic field (IMF) leads to the formation of various plasma boundaries which will be described in Section 1.2.4.2. In this way, the solar wind flow is directed around the planet and does not impact the atmosphere directly. This means that even though the solid body of Venus is entirely unmagnetized, it is still protected against strong erosion processes, albeit this protection is weaker than in the case of the Earth. In the following two sections, we will describe the external influences to which Venus and especially its atmosphere are exposed, and the consequences of the resulting plasma interactions.

1.2.4.1 Solar wind and IMF

The solar wind is a plasma flow consisting of charged particles (mainly electrons and protons, and a few percent of He^{++}) emanating from the Sun. Near Venus, it has typical velocities of about 400 km/s. In the solar wind, the plasma β (ratio of kinetic to magnetic pressure) is generally larger than one, which means that the IMF is "frozen" into the solar wind flow and is carried along by it. Due to the solar rotation, the IMF field lines assume the shape of a so-called Archimedean spiral (see Figure 1.20 for a basic two-dimensional visualization of one single spiral arm, and Figure 1.21 for a general sketch), which in the case of the IMF is named the Parker spiral. It was first described, albeit not with today's name, by Parker (1958). While the angle between the solar wind plasma flow direction and the IMF is around 40° at Venus and 45° at the Earth, it increases to nearly 90° at the location of the outer gas giants and ultimately goes to 90° at infinity. Due to its inclination, it causes asymmetries between dawn and dusk side in the plasma distribution, which can be observed in the ionosphere as well as in the shape of the bow shock at Venus. These effects are also known at various other planets, e.g. Earth and Jupiter. However, the IMF direction is not the only effect that is responsible for asymmetries. Other influences include aberration due to the orbital motion of a planet, and additional effects that have not been fully determined yet.
Due to changes in the polarity of the magnetic field, the heliospheric current sheet actually attains a wavy appearance when viewed in three dimensions, and is sometimes compared with a ballerina skirt. An illustration of its shape is given in Figure 1.21. Here it is obvious that the angle between IMF and solar wind flow direction at a given location can vary, leading to changing external field configurations which may influence the plasma processes.

1.2.4.2 Interaction with the solar wind

The interaction between solar wind and planetary plasma leads to the formation of several different interaction regions and boundaries at Venus. The most prominent ones on the dayside are the **bow shock**, the **magnetic barrier** and the **ionopause**. The formation processes leading to these features will be discussed in this and the following section, together with their key properties.

Unlike the Earth, Venus does not have an intrinsic magnetic field. This means that the

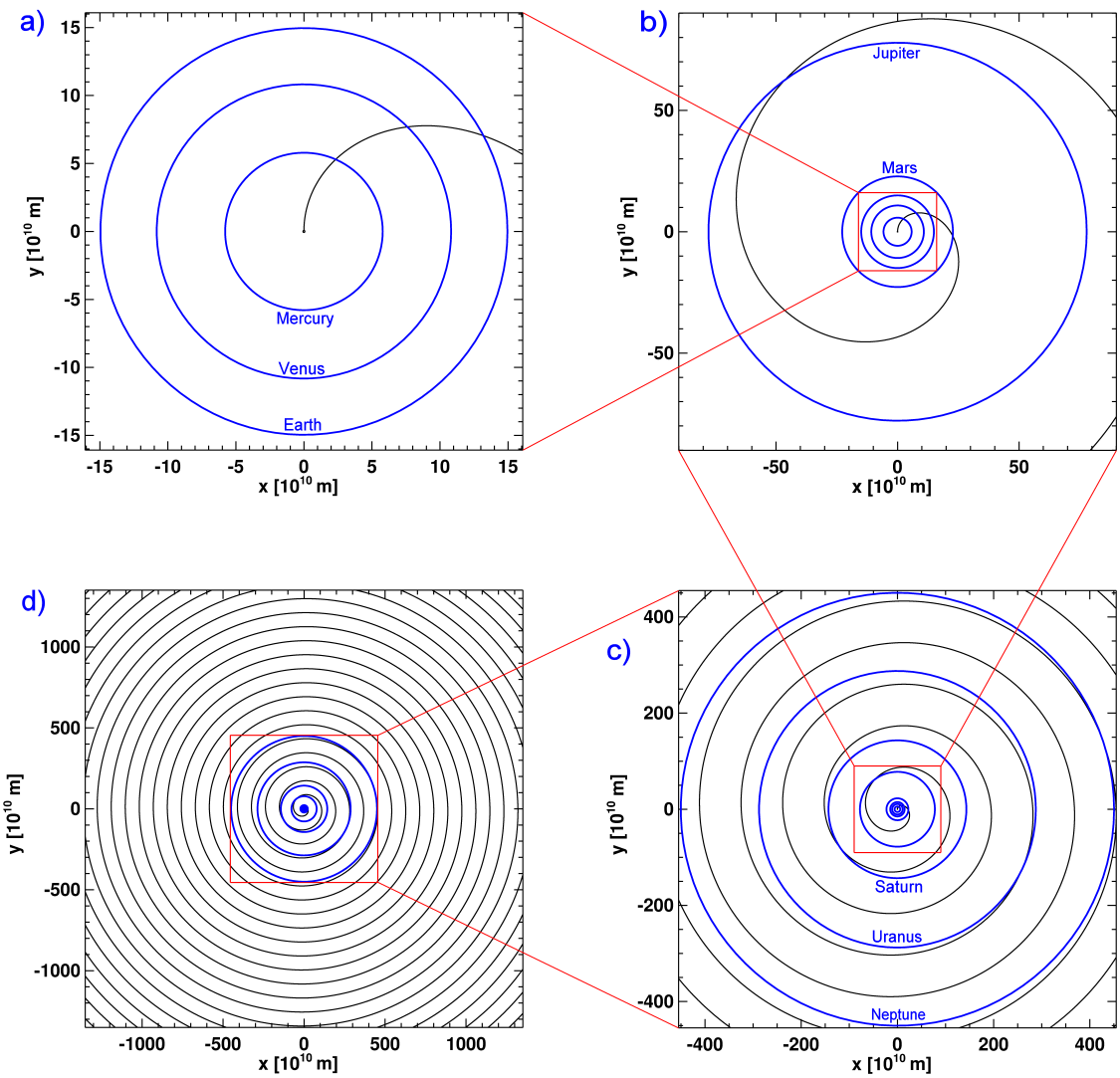

Figure 1.20: The black trace represents one arm of the IMF (Parker) spiral across the solar system seen at various scales for the simple assumption of a solar wind speed of 400 km/s and a solar rotation period of 25.05 days (which is the period at the equator). The blue lines indicate the orbits of the planets around the Sun, approximated as circles with a radius equal to the orbital semimajor axis for simplicity. Starting with the upper left plot and continuing clockwise from a) to d), the view is gradually zoomed outward so that the IMF angle and general field configuration with relation to the orbits of the planets become visible.

planet is not shielded from external influences by a magnetosphere, and the solar wind interacts directly with the near plasma environment of Venus. When the supermagnetosonic solar wind encounters the planetary plasma, a distinct *bow shock* is formed. Its distance from Venus varies with the solar cycle, growing larger with increasing solar activity. This is probably caused by the higher EUV flux near solar maximum, which leads to an increase in the scale height of the neutral atmosphere and consequently to larger mass-loading rates of the incoming solar wind, an effect which shifts the bow shock to larger

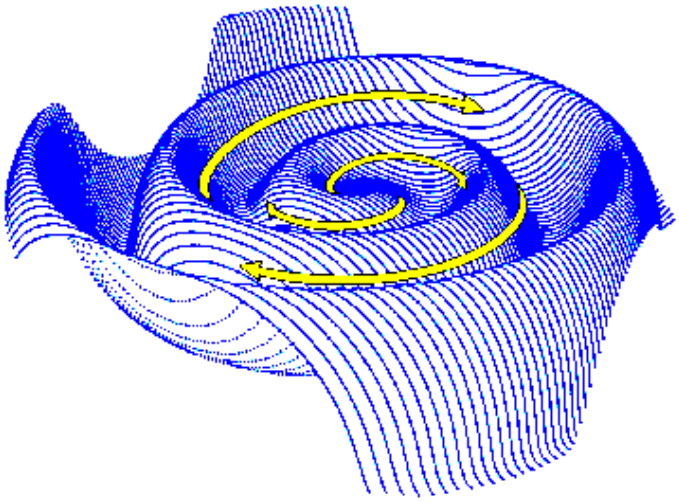

Figure 1.21: The spiral and wavy shape of the heliospheric current sheet which is caused by the combination of the solar wind outward velocity and the solar rotation, together with changes in field polarity (© Wikimedia Commons).

distances from the planet (Phillips and McComas (1991)). At the bow shock location, the solar wind flow is suddenly decelerated and most of its kinetic energy is transformed into thermal energy, leading to strong heating of ions and electrons. The resulting hot, shocked solar wind plasma then encounters the ionosphere, carrying with it the frozen-in magnetic field. This interaction induces shielding currents in the ionosphere, which in turn keep out the external magnetic field and create a pseudo-magnetosphere that deflects the shocked solar wind plasma around Venus. This deflection leads to a draping of the magnetic field lines around the obstacle and the formation of the so-called magnetic barrier. Due to the piled-up field, magnetic pressure dominates in this region, which is largely depleted of plasma. Almost no solar wind particles enter the magnetic barrier, so that solar and planetary particles are separated and there is no direct interaction. Instead, solar wind momentum is transferred indirectly to the ionosphere via the magnetic barrier. Figure 1.22 illustrates the most important plasma boundaries at Earth and Venus in comparison. At a first glance, it becomes immediately apparent that the scales in a) and b) are different, since in reality Earth and Venus are almost equal in diameter. But because the Earth has an internal magnetic field, it is able to stand off the solar wind at a larger distance, leading to a much more extended magnetosphere in which the solar wind is deflected already several Earth radii upstream. In the case of Venus, on the other hand, the interaction between solar wind and planetary plasma takes place much closer to the planet. Beginning at the bow shock, the approaching solar wind is directed around the planet, taking the IMF with it, which as a consequence is draped around the obstacle. The black region represents the magnetic barrier, which forms the boundary between the shocked solar wind plasma flow and planetary ions. The latter are mainly found in the ionosphere, which is indicated by the dotted area. Sometimes the upper boundary of the magnetic barrier is termed the (induced) *magnetopause*. Towards the nightside, a magnetic cavity is formed as the solar wind pushes the magnetic field lines behind the planet

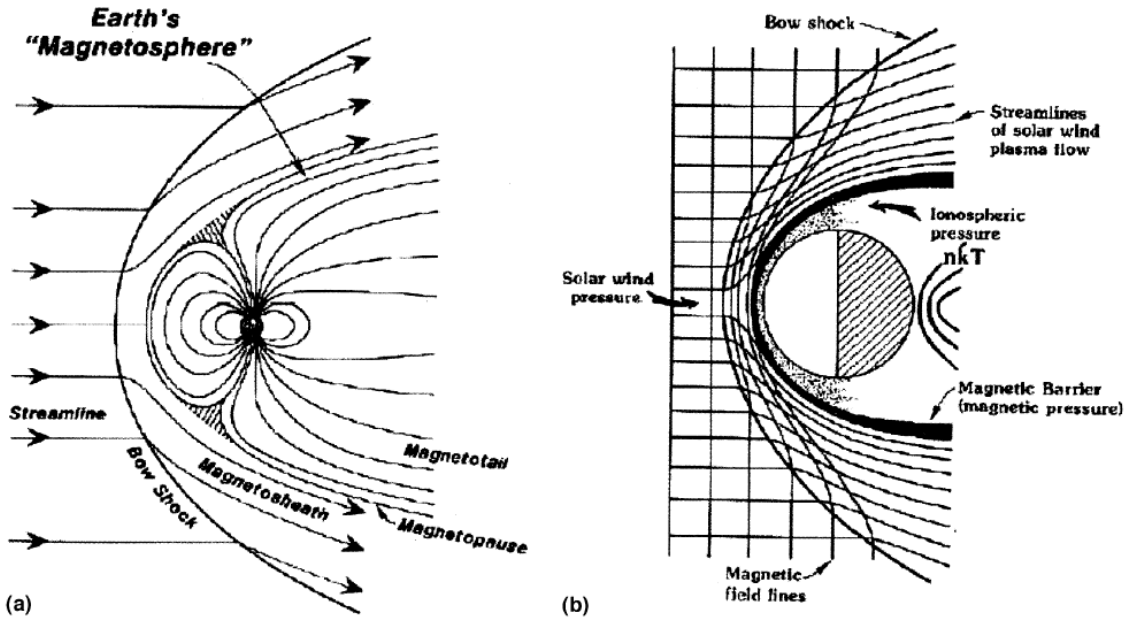

Figure 1.22: A sketch of the plasma boundaries at Earth (left-hand side) and Venus (right-hand side) (Luhmann et al. (2004)).

(Lundin and Barabash (2004)). This leads to a very elongated magnetosphere pointing away from the Sun, which is called the magnetotail.

1.2.4.3 Magnetization states of the ionosphere

The magnetic barrier acts as a "cushion" (Brace and Kliore (1991)) which indirectly transfers the solar wind momentum to the ionosphere. The latter usually keeps out the magnetic field due to ionospheric shielding currents. Only small-scale flux ropes with typical diameters of a few tens of kilometres can enter the ionosphere or are even formed there. As described in Section 1.2.3, the ionopause varies in altitude, depending on internal and external pressure contributions. But this is only true up to a certain point, as can be seen in Figure 1.23: above about 4 nPa, a saturation effect takes place, thus the ionopause altitude remains the same even though the external pressure increases. This is due to the fact that at these low ionopause altitudes, the particle density is so high that the solar wind is quickly decelerated by mass loading (Brace and Kliore (1991)). In this situation, the ionosphere is not able any more to maintain pressure balance by decreasing its upper boundary altitude. Therefore magnetic field will enter the ionosphere, which in turn adds to the total internal pressure, restoring pressure balance (Luhmann and Cravens (1991)). According to Luhmann et al. (1984), the ionospheric magnetic field itself is actually caused by currents which are induced by the external magnetic field.
Already the early PVO results revealed that the ionosphere often displays magnetized states, but on the other hand, it is also often largely field-free (unmagnetized) with the exception of the small-scale flux ropes mentioned above (Luhmann and Cravens (1991)). Figure 1.24 shows examples for both of these states. The upper panel, orbit 175, is a clearly unmagnetized case, since the magnetic field within the ionosphere is very low

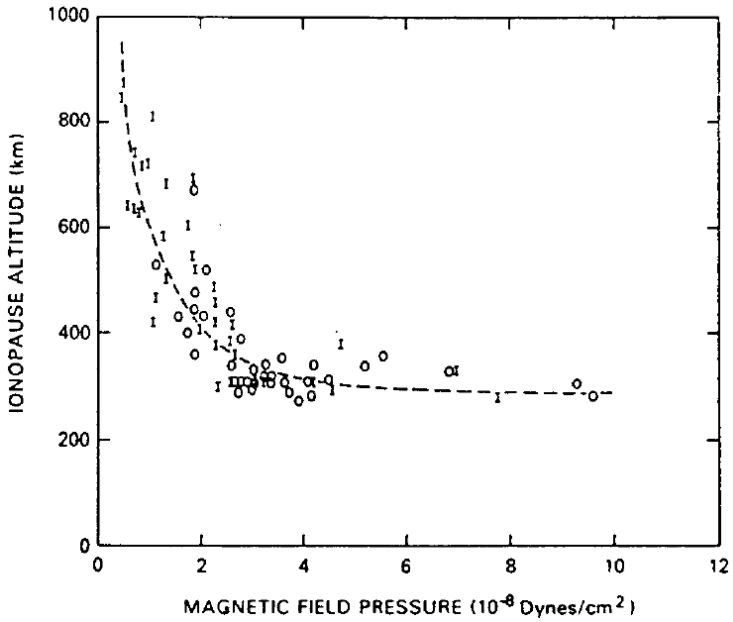

Figure 1.23: PVO ionopause altitude measurements versus the magnetic pressure inside the magnetic barrier (Brace and Kliore (1991)). The letters *I* and *O* stand for inbound and outbound measurements. All data reproduced in this figure were recorded on the dayside and rather far from the terminator (at a solar zenith angle of $< 64°$). 10^{-8} dynes/cm^2 = 1 nPa.

and this region is threaded by flux ropes. On orbit 176, on the other hand, the field only shows a slight decrease upon entry into the ionosphere and then grows again up to 150 nT. This field configuration is characteristic of a magnetized state. An interesting fact is that the transition from a completely unmagnetized to a strongly magnetized ionosphere takes place within only one day in this example. This is due to an interplanetary shock which reached Venus between the times when these two profiles were recorded (Elphic et al. (1980)). Accordingly, the magnetic barrier field strength increased, exerting more pressure on the ionosphere and magnetizing it.

The flux ropes which often appear in the unmagnetized ionosphere were described in detail by Russell and Elphic (1979) and Elphic and Russell (1983b). Basically they are approximately cylindrical regions containing twisted magnetic field lines. They have a diameter of only a few tens of kilometres, while their typical length scale is much larger, though not yet fully investigated. The authors of the two mentioned articles used PVO measurements to infer the theoretical structure of a flux rope, which is given in Figure 1.25. Depending on how a spacecraft crosses such a region, it will see varying magnetic field strengths and orientations, as illustrated in Figure 1.26. Closer to the flux rope centre, the field is much more axial and also stronger than in its outer parts. Flux ropes are assumed to be created by ionospheric shear flows or viscous flows at the ionopause (Russell and Elphic (1979)). Moreover, it was found that flux ropes tend to be more common at lower altitudes, which means they either pile up in this region or they are produced preferentially at lower altitudes. Generally, they seem to have a lifetime which

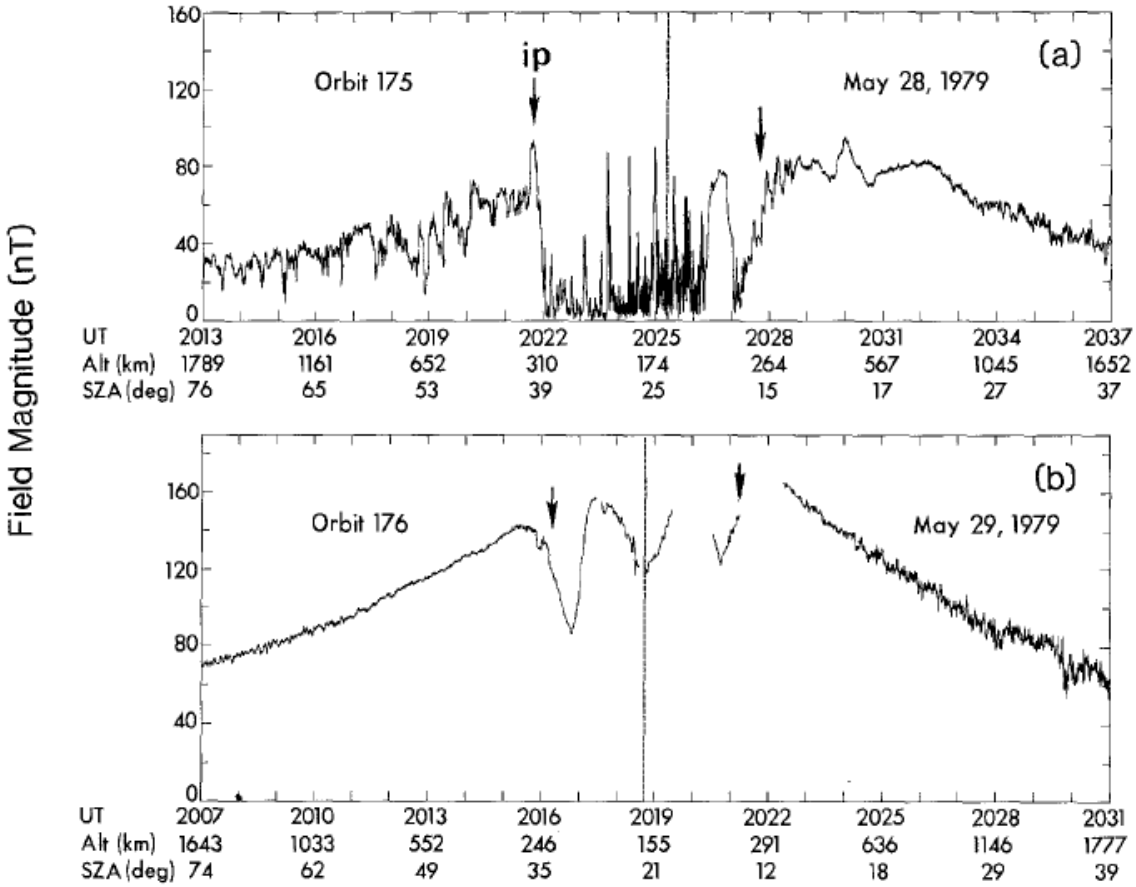

Figure 1.24: Magnetic field measurements during two subsequent dayside ionospheric crossings by PVO (Luhmann and Cravens (1991)). Ionopause locations are indicated by arrows.

is long enough for them to be swept from the dayside to the terminator. This is important because these flux ropes might contribute to the creation of nightside ionospheric holes (cf. Figure 1.17).

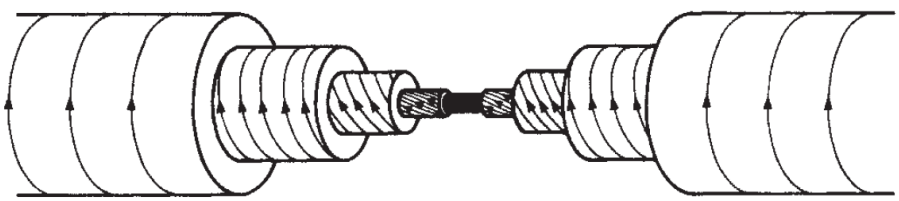

Figure 1.25: A typical flux rope magnetic field configuration, derived from PVO data (Russell and Elphic (1979)).

Of course, there are also transitional ionospheric magnetization states with weaker large-scale fields, or a mixture of large-scale fields and flux ropes. These are presumably formerly magnetized states with an already partially diffused magnetic field. In a typ-

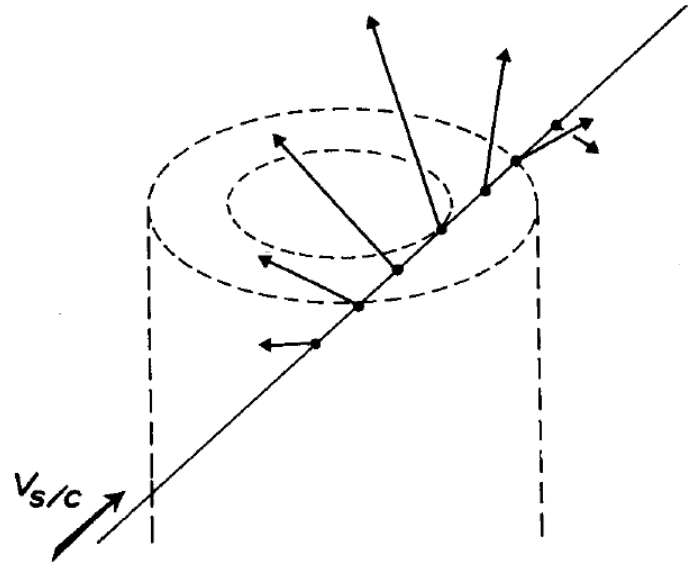

Figure 1.26: Illustration of a spacecraft trajectory crossing a flux rope off-centre, and the magnetic field vectors which will be recorded by the spacecraft (Elphic and Russell (1983b)).

ical magnetized case, according to Luhmann and Cravens (1991), the dayside ionopause is located at rather low altitudes (below 300 km for PVO measurements), and the ionopause region itself is broad (around 80 km). The large-scale fields that were found in these cases are horizontally orientated, reaching values up to 150 nT. The vertical distribution of these fields always had the same structure, displaying a minimum around 190 km altitude and a maximum near 170 km. The increase in thickness that was observed for the ionopause in those cases where its altitude was low can be explained by the fact that it is pushed to the exobase under these conditions. Consequently, collisions between neutral and ionized particles lead to a broadening of the interaction region (Elphic et al. (1981)). In the unmagnetized PVO cases, on the other hand, the ionopause layer was found to be rather narrow (around 20 km) and located above 300 km altitude throughout the full dayside, as far as this could be observed. These different ionopause altitudes for magnetized and unmagnetized states are in accordance with the pressure balance explanation given above.

In the 1980s, there was a controversy about these magnetization states, since Luhmann et al. (1980) claimed that the ionosphere of Venus is generally either magnetized or unmagnetized. They reported that for solar wind dynamic pressures larger than 8 nPa, the ionosphere was always magnetized. For lower pressures, they found mostly unmagnetized states, but also some magnetized cases which were due to remanent magnetic fields after periods with high solar wind dynamic pressure. This interpretation is also supported by the model of Luhmann et al. (1984). However, Kar and Mahajan (1987a) stated that there must be magnetic states between the fully magnetized or completely unmagnetized cases, and suggested a smooth transition rather than the dichotomy postulated by Luhmann et al. (1980). By analyzing a similar set of data, they proved a linear relation

between the peak magnetic field acting on the ionopause[7] and the magnetization states of the ionosphere. This investigation had already been conducted by Luhmann et al. (1980), who however did not comment on the fact that there are data points across a large range of ionospheric magnetic field (10 - 160 nT) without any clear gap that would indicate a dichotomy. Kar and Mahajan (1987a) also failed to understand that magnetized states can exist even below a dynamic pressure of 8 nPa due to the decay time of the magnetic field, as described by Luhmann et al. (1980).
In a comment on Kar and Mahajan (1987a), Luhmann (1988) replied that their statement concerning the dichotomy of magnetization states (Luhmann et al. (1980)) had been misinterpreted. Regarding the model of Luhmann et al. (1984), it is quite obvious that the magnetic field decays within several hours and thus there will be observable transitional cases. These were also seen by us in the VEX data, as will be described in Section 2.5.2.2.
Ionospheric magnetic fields are a very interesting research topic because they significantly influence particle transport between different altitude layers as well as from the dayside to the nightside, and therefore have a strong effect on the structure of the ionosphere as well as on atmospheric loss processes.

1.3 Magnetospheres in our solar system

There are various types of magnetospheres in our solar system, depending on the atmospheric properties of a particular object and on the presence of an intrinsic magnetic field. Figure 1.27 shows the sizes and shapes of magnetospheres for different solar system bodies. The four left-hand and middle panels illustrate the bow shocks for planets with an intrinsic magnetic field, and their basic field configurations. Different field strengths as well as different distances from the Sun influence the bow shock distance, so that the size of the magnetosphere relative to the respective planetary diameter varies. A striking aspect is the sheer size of the gas giants' magnetospheres, which especially in the case of Saturn and Jupiter far exceeds the diameter of the Sun. The two right-hand plots show the magnetospheres of unmagnetized celestial bodies. Due to the lack of a magnetic field, they are not able to stand off the solar wind at large distances from their surface, so that the bow shock forms very close to the planet or nucleus. One exception is comet Halley; this typical property of cometary bow shocks will be explained in Section 1.3.2.1.

1.3.1 Magnetized bodies

1.3.1.1 Earth

The magnetic field of our home planet is the best-explored among all planetary magnetic fields. People have been using compasses to find the northward direction for several centuries already, starting with the Chinese. The western countries began utilizing compasses around the 12th century, but at that time it was still not clear what was the reason that a magnetic needle pointed towards the north. There were various ideas about the occurrence

[7] In Kar and Mahajan (1987a), the authors first equated the solar wind dynamic pressure to the peak magnetic pressure, which is not true especially towards the terminator (see Section 1.2.3). This error was criticized by Phillips (1987), and a corrected version was published by the authors (Kar and Mahajan (1987b)). But this nomenclature mistake has no effect on the issue discussed in this controversy.

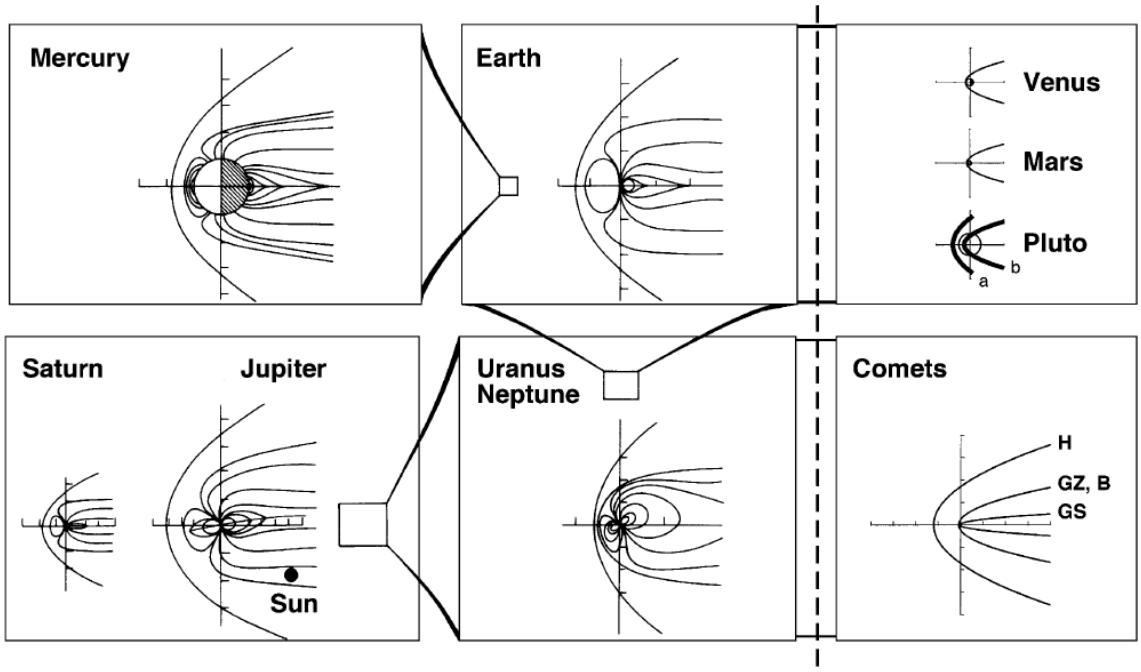

Figure 1.27: The bow shock shapes and distances, together with intrinsic magnetic fields, for all solar system planets, Pluto and comets (Coates (2004)). In the case of Pluto, due to its highly elliptic orbit around the Sun, the bow shock differs significantly between aphelion (a) and perihelion (b). The circle indicates the orbit of Charon, which is thus partially outside Pluto's magnetosphere near perihelion. The abbreviations in the comet figure stand for Halley (H), Giacobini-Zinner (GZ), Borrelly (B) and Grigg-Skjellerup (GS), which have been investigated by spacecraft.

of this phenomenon, e.g. an attractive force exerted by the polar star, or a region close to the north pole which contained large amounts of magnetite. From the 17th century on, scientists came up with better explanations, already involving the composition of the terrestrial core and the effects that it has due to the Earth's rotation (Langlais et al. (2010)). Nowadays it is known that the magnetic field has a dipolar structure, with the magnetic south pole located near the geographic north pole and vice versa. This field is assumed to be created and maintained by an internal dynamo due to the Earth's rotation and its liquid outer core. The basic field configuration, without taking into account external influences, is shown in Figure 1.28. Seen from far away, this field has a very simple dipolar structure. The field strength at the surface of the Earth lies between 20 μT (magnetic equator) and 70 μT (magnetic poles). It is known that there were several field reversals in the past. They take place at random intervals, the last one having happened 780,000 years ago. Since rocks are magnetized by the terrestrial field, they preserve information about past reversals. The presence of these magnetized rocks also influences the Earth's bulk magnetic field today, adding or subtracting a few nT locally, as measured from space. During a field reversal, the magnetic field amplitude is very low over a period of several thousands of years. This situation is very similar to the one observed at Venus nowadays, so we can also learn a lot about our home planet by investigating the Earth's sister planet.

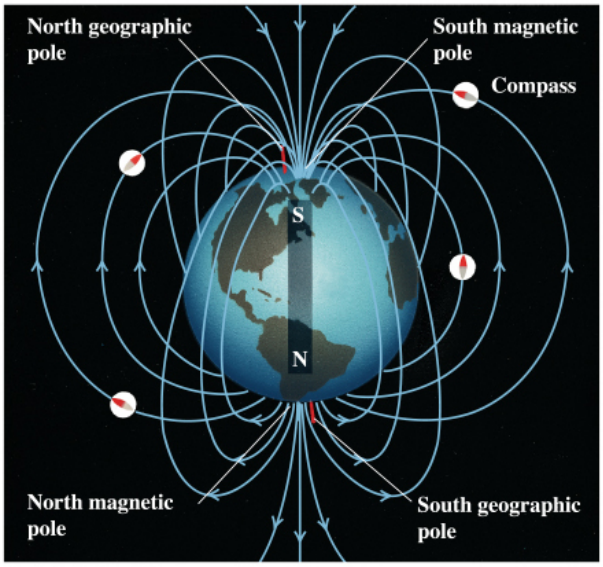

Copyright © Addison Wesley Longman, Inc.

Figure 1.28: Field lines of the Earth's intrinsic magnetic field (© Addison Wesley Longman, Inc.). This is how the configuration would look if there was no external influence from the solar wind and IMF.

The terrestrial intrinsic magnetic field acts as a shield as the solar wind encounters the Earth. The shocked solar wind plasma is strongly decelerated and kinetic energy is transformed into thermal energy. These processes create a clear bow shock, similar to Venus, but much further away from the Earth due to its magnetic field (see also Figure 1.22). In response to the external pressure, the sunward part of the terrestrial magnetic field lines is compressed, while the field lines on the nightside extend into a long tail (see Figure 1.29). While the dayside magnetic field lines are closed, which means that both of their ends are connected to the planetary surface, the field lines in the tail are open and extend into space. In the transition regions between closed and open lines, near the magnetic poles, charged particles can enter the Earth's atmosphere, which leads to the creation of aurorae visible from the surface. Because the magnetic axis of the Earth is inclined with respect to its rotational axis, the northern- and southern-hemisphere aurora regions form collars around the poles. At a distance of a few Earth radii from the surface, the so-called van Allen belts are located. They were discovered by Explorer I, the very first satellite sent into space by the United States. These belts are toroidal accumulations of energetic charged particles which are trapped by the terrestrial magnetic field and probably contribute to aurorae. Already after a more detailed investigation by the Explorer-III satellite in 1958, the general structure of these particle belts was recognized, as illustrated in Figure 1.30. A modern illustration is given in Figure 1.31. As can be seen, these belts consist of two toroidal regions, the inner belt containing mainly protons, but also some electrons, while the outer belt consists almost exclusively of electrons. All of these particles have very high energies on the order of keV to several hundred MeV; therefore these regions are often termed the van Allen radiation belts. They have to be taken into account for satellites

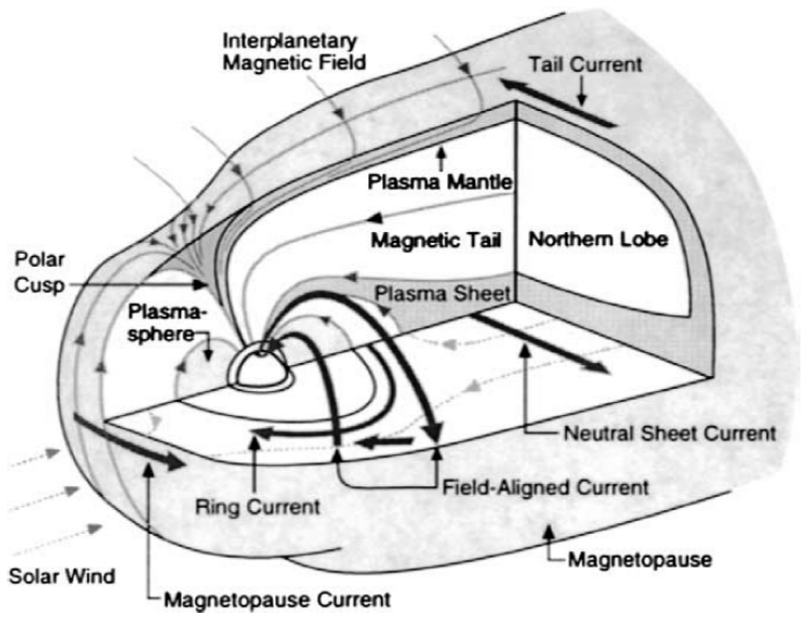

Figure 1.29: The overall configuration of the magnetosphere of the Earth (Russell (2004)). The polar cusp is the region in which aurorae are created (see description in this section). Due to the variable magnetic field structure, currents are created within the magnetosphere and at its boundary.

that orbit the Earth at higher altitudes, since the resulting radiation can saturate or even damage sensors.
Due to the charged particle populations, currents are flowing within the terrestrial magnetosphere. Inside the van Allen belts, the current is often termed “ring current”, and it is also included in Figure 1.29. In the magnetotail of the Earth, the so-called “tail current” flows transversely to the magnetic field lines and divides the tail into two lobes with opposite magnetic field polarities. Therefore it is also named the “neutral sheet current” (Russell and Luhmann (1997)).

1.3.1.2 Mercury

Mercury has a dynamo which maintains an intrinsic magnetic field, albeit three magnitudes weaker than that of the Earth (Zurbuchen et al. (2004)). Since Mercury is also much closer to the Sun, the incident solar wind pressure is ten times stronger than at the Earth. These two factors lead to a magnetosphere which is eight times smaller in comparison to the planetary diameter than that of the Earth (see Figure 1.32). However, it is still able to stand off the solar wind above the surface, except in cases of strong solar activity. Another important difference compared to the Earth case is that Mercury does not have an atmosphere and therefore no ionosphere either. It only possesses a very thin exosphere that consists mainly of atoms and ions sputtered from the surface by impacting solar wind and magnetospheric particles. The most abundant exospheric species are O^+, Na^+, K^+ and Ca^+ (Killen et al. (2004)). The average time that a particle remains in the exosphere

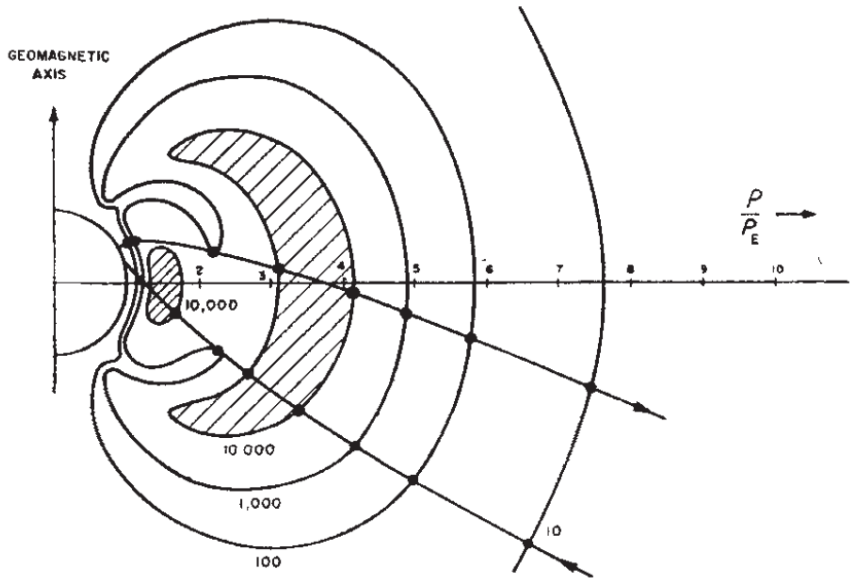

Figure 1.30: The van Allen belts, as registered by the Geiger-Müller counter on Explorer III (van Allen and Frank (1959)). The two shaded regions indicate where the counters of the spacecraft were saturated, corresponding to more than 10,000 counts (electrons or gamma rays) per second. The x-y plane of this plot lies within the geomagnetic meridian plane, its y axis is therefore inclined with respect to the Earth's rotational axis.

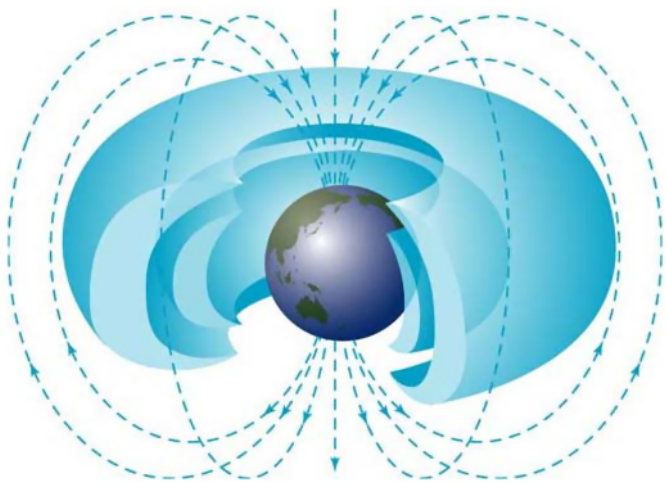

Figure 1.31: The overall toroidal structure of the two main van Allen belts (© NASA).

is of the order of only a few hours, since they are quickly removed by thermal escape and losses associated with photo-ionization and charge exchange. Generally, the atoms that are sputtered from the surface of Mercury are quickly ionized and picked up by magnetospheric plasma flows. Magnetospheric ions can in turn impact the planet again and cause subsequent sputtering. Therefore there is a large degree of interaction between magneto-

sphere and surface (Slavin (2004)), especially since the planet occupies a relatively small amount of its forward magnetosphere.

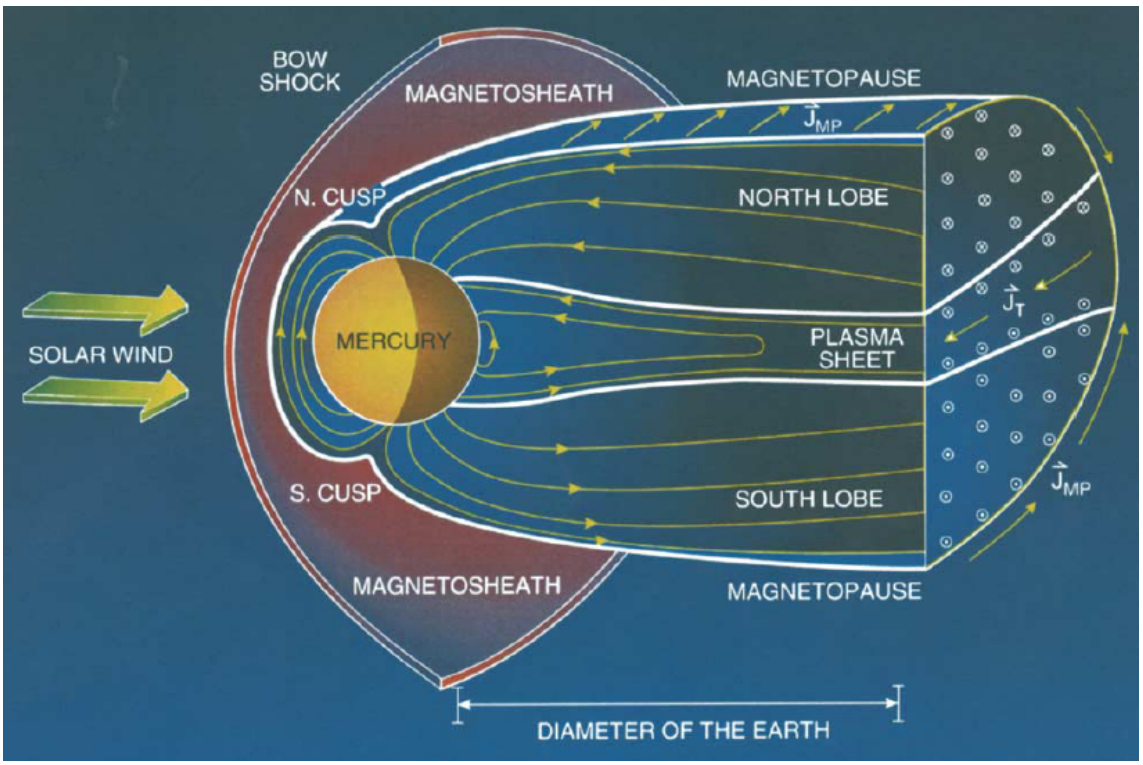

Figure 1.32: The magnetosphere of Mercury (Slavin (2004)). Its general structure is very analogous to that of the Earth, including a current sheet in the tail, but the spatial extent of all features is smaller relatively to the planetary diameter.

1.3.1.3 The gas giants in our solar system

Because of their strong magnetic fields and small incident solar wind pressure in comparison to Earth, all four gas giants display large magnetospheres. In the case of Jupiter, for example, the dayside magnetopause has a standoff distance from the centre of the planet that is about 100 times larger than the distance of the cloud tops (Russell (2004)). There are similar boundaries and current systems as in the Earth's magnetosphere, including analogues to the terrestrial van Allen belts. However, due to gas loss from moons, especially at Jupiter (Io) and Saturn (Enceladus), the magnetospheric plasma content is much higher. In the case of Io, volcanism releases about one ton of gas per second, producing a permanent gas torus along Io's orbit, as illustrated in Figure 1.33 (Baumjohann et al. (2010)). These neutral atoms are then ionized and make a significant contribution to the Jovian magnetospheric plasma. Electric currents flow along the flux tube shown in the picture, creating aurorae near the poles of Jupiter (Kivelson (2004)). In a similar way, Saturn's moon Enceladus produces a torus of water due to its surface geysers, and adds large amounts (about 100 kg/s) of plasma to the Kronian magnetosphere. Generally, this plasma is then accelerated by the co-rotating planetary ionosphere and due to this fast rotation, it

experiences a centrifugal force which draws it outward, giving the whole magnetosphere an overall oval cross section. As a consequence of this "streamlined" obstacle, the solar wind flow passes this region faster than it would for a non-stretched magnetosphere. This leads to a smaller relative distance between bow shock and magnetopause than for example at the Earth. Due to the high amounts of plasma present in the gas giants' vicinity, their magnetospheres are probably strongly influenced by plasma effects. Also the weaker solar wind (compared to the Earth's location) increases the tendency for other processes to dominate. Most of the described phenomena are known only for Jupiter and Saturn, since Uranus and Neptune have not been investigated in detail by spacecraft. However, the Voyager missions found that both planets have an intrinsic magnetic field, and similar processes are expected to play a role.

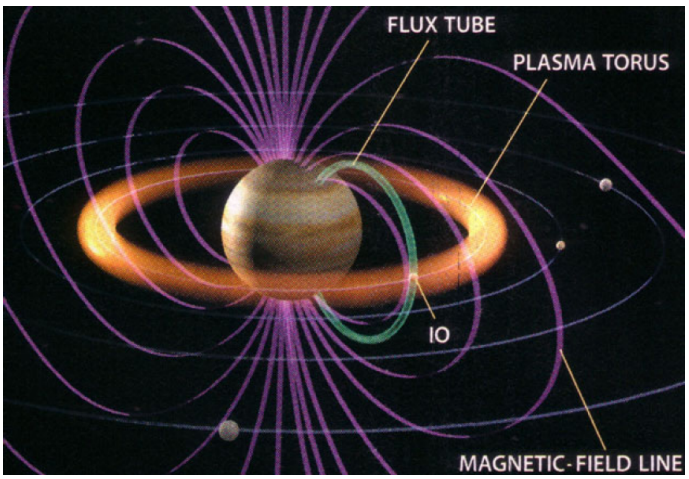

Figure 1.33: The orbit of Io within the Jovian magnetosphere, and the plasma torus which it produces (Baumjohann et al. (2010)).

1.3.1.4 Ganymede

It was a surprise when the Galileo spacecraft detected an intrinsic magnetic field at the Jovian moon Ganymede because one had expected that its core was already fully solid and therefore no dynamo could be active. Actually its magnetic moment is even twice as large as that of Mercury, and its intrinsic field amplitude also exceeds the value of Jupiter's field at the location of Ganymede by a factor of 7 (Kivelson (2004)). Ganymede's orbit lies within the magnetosphere of Jupiter. Thus it is not exposed to the solar wind, but to the magnetospheric plasma flows, which can be much more variable due to changes in the extent of the magnetosphere or Ganymede's orbit crossing different parts of this region. Nevertheless, the approaches used to describe the interaction of planets with the solar wind can also be applied for the interaction between moons and magnetospheric flows, which is just a miniature version of the former. The only important difference is that the flow inside a magnetosphere is sub-magnetosonic, so that no bow shock is formed in case of interaction with an ionosphere or intrinsic magnetic field. Ganymede is the only known celestial body that presents a magnetosphere inside another magnetosphere. While its shape looks slightly different from that of the Earth (see Figure 1.34), its basic

configuration is the same. It also has open magnetic field lines at the poles, the boundary between closed and open field lines, through which energetic particles can enter. A flux tube connects Ganymede and Jupiter, similar as for Io, leading to a particle flow that manifests as aurorae near the pole of Jupiter.

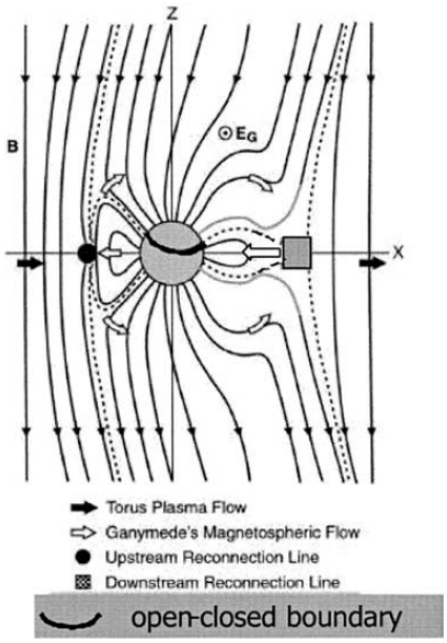

Figure 1.34: The magnetosphere of Ganymede (Kivelson (2004)). The magnetic field lines are strongly deformed by the ambient plasma and magnetic field of Jupiter, and reconnection takes place with Jovian field lines instead of the IMF. Independently from these special conditions, Ganymede presents a very clear case of an intrinsic magnetosphere.

1.3.2 Unmagnetized bodies

Since the plasma environment of Venus has been described extensively in Section 1.2.4, we will skip it here and just present other unmagnetized solar system bodies for an overview.

1.3.2.1 Comets

Similar to planet Venus, comets are generally assumed not to have an intrinsic magnetic field. The composition of their solid nucleus is rather different from all planets; comets are often popularly described as “dirty snowballs” since they consist of a mixture of dust and ice. As they approach the Sun, the ice starts to sublimate, leading to the escape of gases which take dust particles with them. Due to the low gravitation of a typical comet-sized body, a very extended atmosphere forms, which is called the *coma*. Solar EUV radiation ionizes atoms and molecules, creating a kind of “ionosphere” and enabling electromagnetic interaction with the solar wind. Since the plasma extends so far from the

cometary nucleus in all directions, ion pickup already occurs at large upstream distances, slowing down the solar wind plasma locally due to mass loading. For each field line, the section close to the comet picks up more ions and is decelerated more strongly than the sections with a larger distance from the nucleus. This effect leads to a draping of the IMF lines around the nucleus and the formation of an induced magnetosphere. The cometary bow shock itself is rather weak since the solar wind slows down gradually in the extended plasma cloud, an effect which also leads to a relatively large distance of the bow shock from the nucleus. Still, analogously to Venus, a magnetic barrier and magnetotail are formed (Cravens and Gombosi (2004)). These cometary plasma boundaries are illustrated in Figure 1.35.

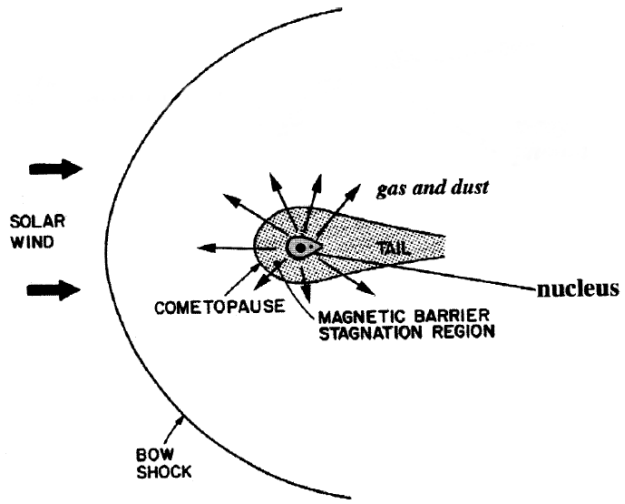

Figure 1.35: The solar wind interaction with the cometary plasma leads to the formation of a clear bow shock, albeit weak, as well as a magnetic barrier and magnetotail (after Cravens and Gombosi (2004)).

While planetary magnetospheres cannot be seen in telescopic images, the plasma outflow from comets is so intense that the magnetotail appears very clearly and is called the comet's "ion tail". Since it always points radially away from the Sun, it can be clearly distinguished from the second tail, the so-called "dust tail", which is due to the outflow of evaporating neutrals and accompanying dust. This dust tail is generally curved, since it trails behind the comet on its orbit. The tails of comets which pass by the Earth at small distances and have a strong particle outflow, e.g. Hale-Bopp in 1997 (see Figure 1.36), can even be seen with the naked eye. This is the only case in which a magnetosphere becomes directly visible, and it can be a great opportunity to convey this concept to the public.

1.3.2.2 Moons

The plasma environment of the different planets' moons can have various characteristics. Except for Ganymede, all moons in the solar system that were investigated so far were found to possess no permanent intrinsic magnetic field. The Earth's moon is a very simple

Figure 1.36: Comet Hale-Bopp in 1997 (`http://www.astronomie2009.at`). One can clearly distinguish the yellowish dust tail and the blue ionotail.

case since it is outside the terrestrial magnetosphere and thus only exposed to the solar wind, and moreover has no significant atmosphere which would interact with the solar wind. Thus its surface is the only obstacle that the incident solar wind encounters. There are no charged lunar particles to interact with, so the solar wind is simply absorbed by the surface of the Moon. This absorption creates a small wake at the nightside, whereas the IMF lines are hardly disturbed at all (see Figure 1.37). The situation is different at

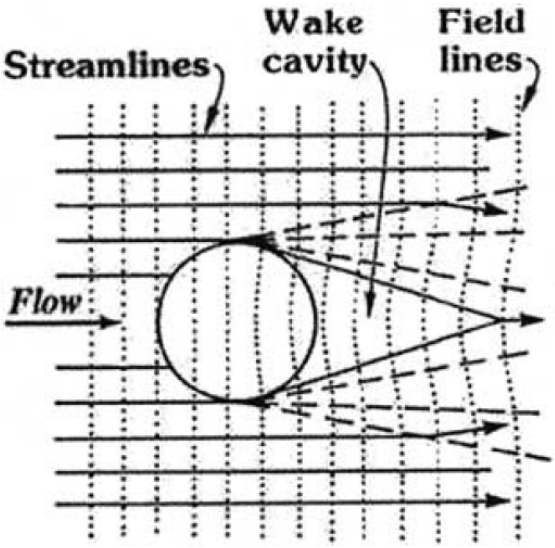

Figure 1.37: The interaction of the solar wind with the Earth's moon (Luhmann et al. (2004)). A small cavity is created on the nightside, but there is no draping of the magnetic field.

the gas giants' moons, since many of their orbits lie within the magnetosphere of their respective host planet. The implications of this configuration were already described in Section 1.3.1.4. Within the gas giants' magnetospheres, there are many moons that, like our Moon, have no significant atmosphere and therefore their plasma interaction is very simple. On the other hand, some of them, like Io and Enceladus, exhibit various processes influencing the magnetosphere of their host planet, as was described in Section 1.3.1.3. Titan, the largest moon of Saturn, is a very interesting case since it is the only moon in our solar system that has a dense atmosphere. Solar radiation and cosmic rays ionize atoms and molecules, leading to the formation of an ionosphere that provides interaction with the external plasma and creates an induced magnetosphere. In this way, Titan is very similar to Venus. In contrast to the four Galilean moons of Jupiter, however, Titan is not always located inside the magnetosphere of its host planet, but is sometimes exposed to the solar wind directly, namely when the Kronian magnetosphere is strongly compressed in response to high solar wind pressure. Its atmospheric composition (mainly N_2, a few percent of methane (CH_4), and trace gases) is similar to that of the young Earth, containing organic haze and heavy hydrocarbon species (Baumjohann et al. (2010)). It is assumed that the induced magnetosphere is at least partially responsible for the creation of complex organic molecules at Titan.

1.3.3 Partially magnetized bodies

1.3.3.1 Mars

In the past, the Red Planet had a dynamo which created an intrinsic magnetic moment; however, nowadays the dynamo is not present any more and all that remains are weak magnetic fields inside the Martian crust. They are heterogeneously distributed on the surface (see Figure 1.38), reflecting geologic processes on Mars in the past. These fields are about ten to 100 times larger than the crustal fields found on the Earth. At some large impact sites, the magnetization is much lower than in the surrounding terrains. This can be due to surface material removed by an impact, but also due to heating which pushed the temperature above the respective Curie temperature for the present materials. Additionally, the high pressure created during such an event can either de-magnetize or magnetize minerals. A similar effect can take place due to plasmas created during the impact, which generate strong magnetic fields (Langlais et al. (2010)). Not all of the Martian impact sites show magnetic anomalies, a fact which probably relates to the question whether the internal dynamo was still active at the time of the impact. Age determinations of these areas can therefore help to narrow down the time until which the dynamo was working. It has been estimated that it already stopped more than 4 Ga ago, thus very early in the history of our solar system.

To first order, Mars has no intrinsic magnetic field to withstand the incoming solar wind and therefore presents a similar case as Venus. Since its atmosphere is much thinner (two orders of magnitude less than the Earth's atmosphere (Lundin and Barabash (2004))), the density of the Martian ionosphere is also significantly lower than at Venus. Still, it is sufficient to cause a clear bow shock in interaction with the solar wind, albeit located within the atmosphere, as well as a draping of the magnetic field lines around the obstacle. When looking at the induced magnetosphere of Mars in more detail, however, it becomes appar-

ent that the crustal magnetic fields produce a clear signature in the ionosphere and the regions above it, causing local asymmetries that have been termed “mini magnetospheres” (Lundin and Barabash (2004)). This effect is illustrated in Figure 1.39. Therefore the detailed configuration of the Martian plasma environment is rather complex, appearing Venus-like in the general picture and Earth-like at certain locations.

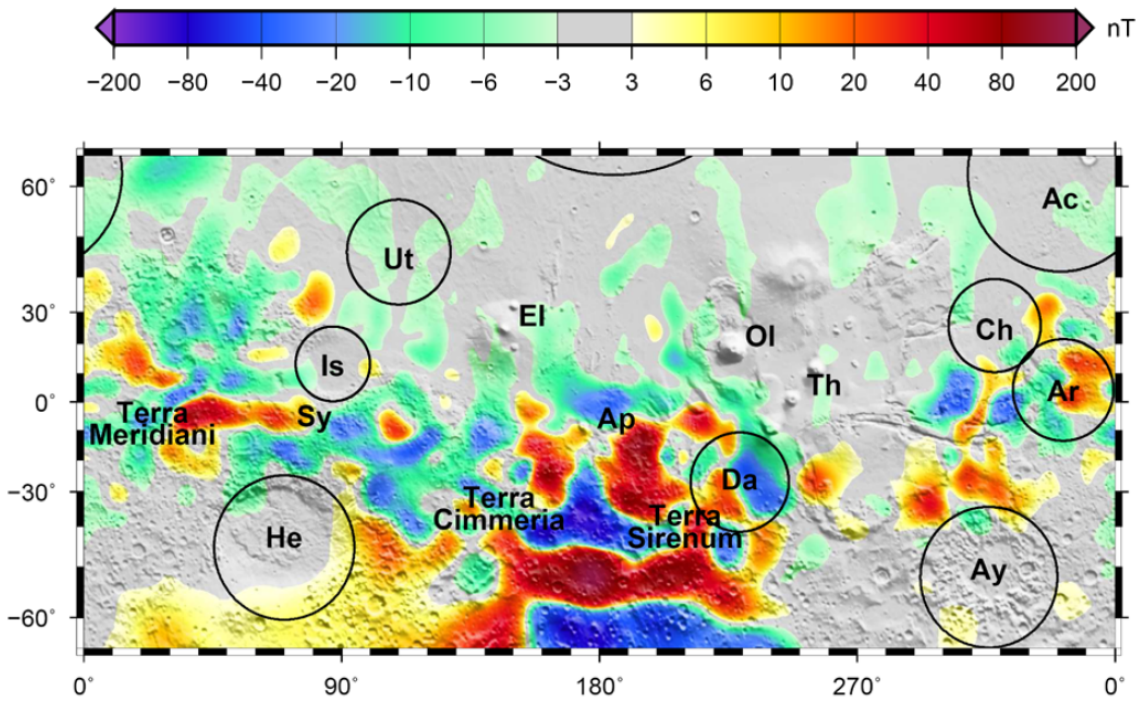

Figure 1.38: The remanent crustal fields on Mars seen from an observation altitude of 400 km, as inferred from measurements by the Mars Global Surveyor (Langlais et al. (2010)). The regions marked with abbreviations alone represent volcanic areas, while the circled areas stand for large impact basins.

1.3.3.2 Induced magnetic fields in moons

Europa and Callisto, two of the Galilean moons of Jupiter, have an icy surface which probably covers an ocean (Kivelson (2004), Baumjohann et al. (2010)). Since the magnetic dipole axis of Jupiter is inclined with respect to its rotational axis and therefore also to their orbital plane, they are exposed to varying magnetic fields which in turn induce time-dependent magnetic moments within their conducting sub-surface oceans. This makes them a very special case in the solar system. The fields are rather small (though detectable), thus these moons are still essentially unmagnetized with respect to their interaction with the ambient plasma. Measurements of their induced magnetic fields can yield a large amount of information on the liquid parts of their interior, giving a whole new aspect to the possibilities of magnetic field investigations in the solar system.

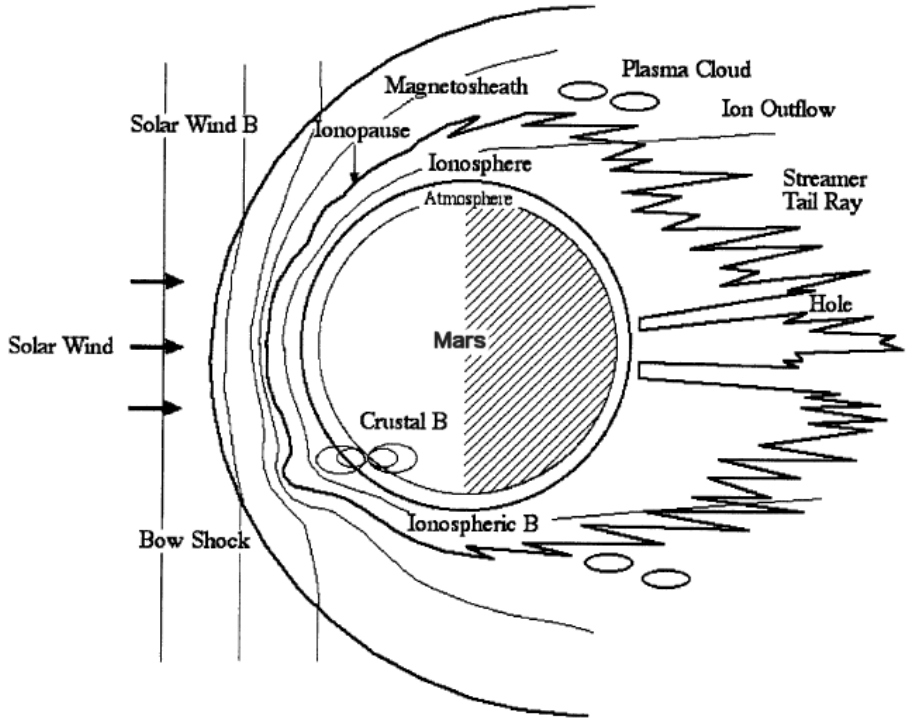

Figure 1.39: The effect of the crustal magnetic fields on the structure of the ionosphere and induced magnetosphere of Mars (adapted from Shinagawa (2004)). Since the strongest fields can be found in the southern hemisphere of the planet, the effect is larger in this region.

2 Data analysis

This chapter consists of a description of the methods which were used for the research presented in this thesis, and the results which we obtained. These include a determination of plasma boundaries in the environment of Venus, general statistics of magnetic fields in the near-Venus plasma regions and the detailed investigation of magnetization states of the ionosphere. Some of these results have previously been published in Angsmann et al. (2011).

2.1 Coordinate systems

The coordinate system which we will use for some representations of the data we analyzed is the so-called VSO (Venus Solar Orbital) System. The origin of this coordinate system lies in the centre of Venus. The x axis is pointing towards the Sun, the y axis is orientated opposite to the direction of the orbital motion of Venus around the Sun, and the z axis is directed northward, perpendicular to the two other axes. For some plots, we are using a slightly modified version of these coordinates, in which the x axis remains the same, but the y axis (usually named R_{cyl} because cylindrical symmetry is assumed) combines the VSO y and z coordinates: $R_{cyl} = \sqrt{y^2 + z^2}$. In this way, R_{cyl} represents the total distance of a given point from the Sun-Venus line and often provides a better overview of the geometry of the VEX trajectory. Furthermore, it allows an easy determination of the so-called solar zenith angle (SZA). The SZA of the VEX position at a given time, for example, describes the angle between the Venus-VEX line and the Venus-Sun line. Thus the SZA is zero at the subsolar point, 90° at the terminator and 180° at the antisolar point, deep in the nightside.
Figures 2.1 and 2.2 show examples of a part of a single Venus Express orbit in the two described representations. The first figure is plotted in the x-z plane of the VSO system, where the electron count rates are just provided to give a better overview of the location of Venus Express with respect to the plasma boundaries. High electron count rates usually occur near the bow shock crossing. In this representation, it is however not clear what is the inclination of the VEX orbit with respect to the plane used for the plot, so the high electron count rates occur at seemingly random locations. In Figure 2.2, on the other hand, all important aspects of the orbit are clearly recognizable since the y axis of the plot now represents the general distance of a point from the Sun-Venus line. The strong increase in electron count rates at the dayside bow shock can be found very close to the average bow shock, and also the more diffuse nightside bow shock is in an appropriate location. It is now also very simple to read off the solar zenith angle of a specific location of VEX; here the SZA is equal to the angle between the x axis and the line connecting

VEX to the centre of Venus.

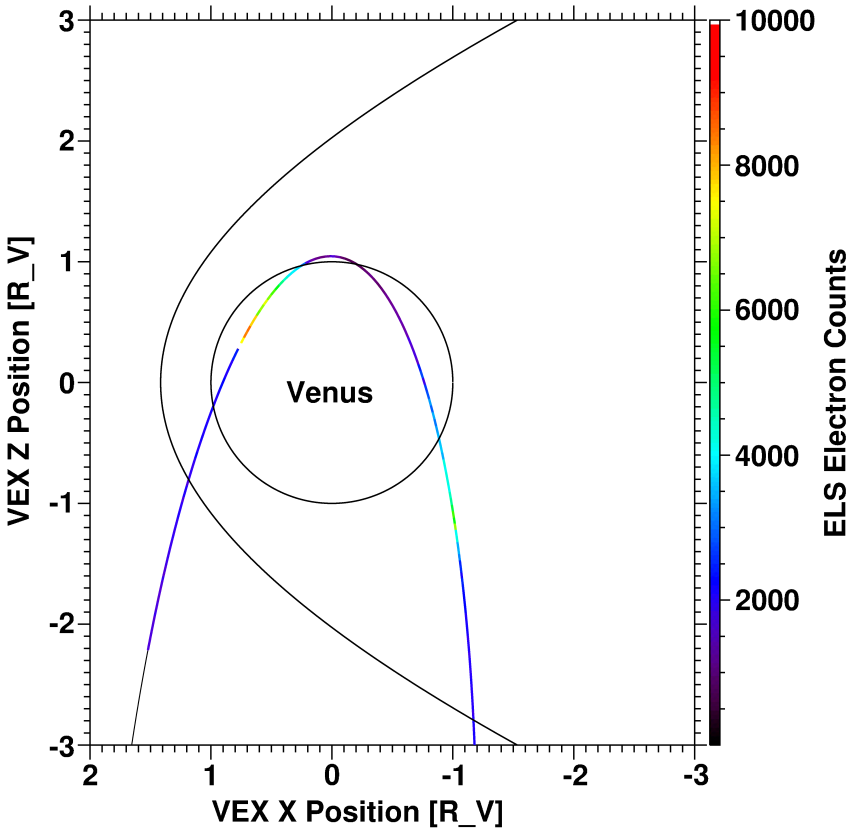

Figure 2.1: The orbit of Venus Express, as seen in the VSO *x*-*y* plane. The circle is planet Venus, the hyperbola represents the average bow shock location (taken from Martinecz et al. (2009)) and the coloured line corresponds to the trajectory of VEX. The colours indicate the electron count rates over all energies, as measured by ELS.

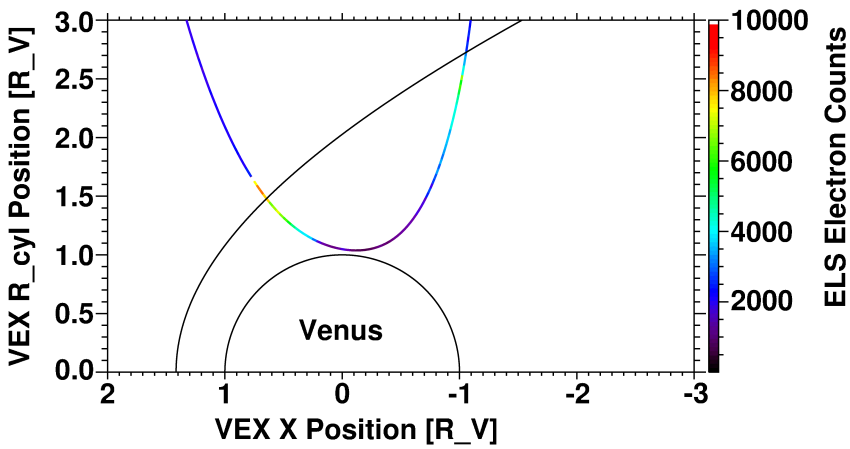

Figure 2.2: The same orbit as shown in Figure 2.1, but now using R_{cyl} instead of z_{VSO}.

2.1.1 Aberration

Since Venus is moving around the Sun on its orbit at a mean velocity of about 35 km/s (see Table 1.2), an observer on the planet would see the solar wind having an additional negative velocity component in the VSO y direction, as shown in the left-hand part of Figure 2.3. If both the solar wind intrinsic velocity and this y component are combined, assuming a mean solar wind speed of about 400 km/s, the solar wind effectively seems to flow along an axis which is inclined by $\alpha = 5°$ relatively to the VSO x axis. For the plasma boundaries which are subject to changes due to the influence of the solar wind, it is very important to take this so-called aberration into account because otherwise, asymmetries will appear. Therefore the VSO x and y axes were rotated by the aberration angle α, keeping the z axis constant (see right-hand part of Figure 2.3):

$\vec{x'} = \vec{x} \cdot \cos\alpha - \vec{y} \cdot \sin\alpha$

$\vec{y'} = \vec{x} \cdot \sin\alpha + \vec{y} \cdot \cos\alpha$

$\vec{z'} = \vec{z}$

In this new coordinate system, the solar wind is thus flowing along the x' axis and cylindrical symmetry can be assumed again. In the following sections, we will use these coordinates to describe the locations of the bow shock and the magnetopause, but not for the ionopause crossings, since the solar wind does not play a significant role in this region any more; instead, solar radiation effects prevail and these are only symmetric in the original VSO system.

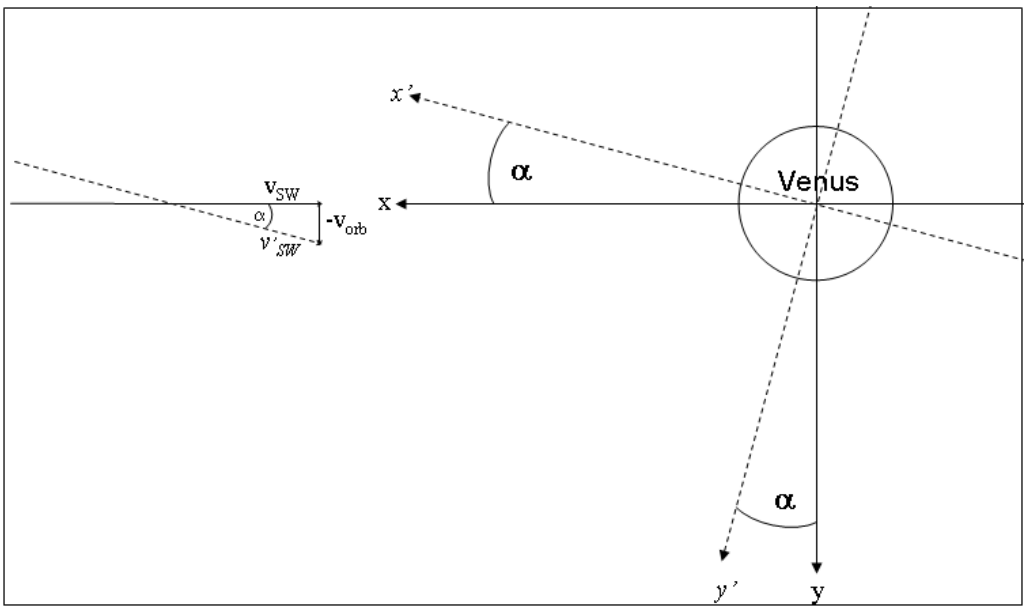

Figure 2.3: The origin of the solar wind aberration at Venus. The planet is moving in the $-y$ direction on its orbit around the Sun, leading to an additional velocity component $\vec{v}_{\mathrm{orb}}$ of the incoming solar wind which aberrates it by an angle of $\alpha = 5°$, seen from Venus (left-hand part of the image). The right-hand side shows the new coordinate axes, x' and y', which are rotated by α with respect to the original VSO axes in order to compensate this aberration effect.

2.2 Interpretation of Venus Express plasma data

The raw data coming from the VEX sensors cannot be used immediately for science purposes, but they first have to be processed and calibrated. We are very thankful to the people who dedicate their time to this task and therefore make it possible for us (and many others) to successfully investigate the scientific facts hidden in these data. Even after calibration, it is important to keep in mind the specific properties of each detector, since these can still have an impact on the data. Knowing at least the basic configuration and underlying physical principles utilized by the instruments is an essential key to prevent false interpretation of occurring patterns in the recorded data. In this section, we will describe the measurements delivered by the ELS and MAG sensors, and the basic conclusions which can be drawn from them.

2.2.1 ELS measurements

The ELS on Venus Express detects electrons between 5 eV and 20 keV (see Section 1.1.3.2), usually at a temporal resolution of 4 s, but in some cases also in 1-s intervals, and yields a full energy spectrum. One example of ELS measurements is presented in Figure 2.4.

Before 06:22, VEX is just measuring electrons in the solar wind which have a low-energy spectrum constant over time. At 06:22, however, VEX enters the dayside bow shock, which is clearly recognizable by the sudden increase of electron count rates within a large energy range from about 30 to 200 eV[1]. This is the region in which strong heating takes place due to the rapid deceleration of the solar wind. As Venus Express further approaches the planet, these high-energy electron counts gradually decrease until there is a clear drop at 06:40. This marks the entry into the magnetic barrier, the region which separates the solar wind from the ionospheric plasma, and in which the plasma density is low since the compressed magnetic field creates a high magnetic pressure. Shortly after this crossing, at 06:45, lower-energy electrons between about 18 and 25 eV appear. These are ionospheric photoelectrons, produced by solar EUV ionization of atmospheric species. Therefore these electrons display a very typical energy range, visible as a clear band in the figure. Coates et al. (2008) reported on two distinct energy peaks in VEX ELS photoelectron spectra, which they attribute to photoelectrons created in the ionization process of O and possibly also CO_2 by solar He 30.4 nm photons. Their findings are shown in Figure 2.5. Due to the negative spacecraft potential at the time of the measurements, the real electron peak energies are shifted in relation to the figure and lie at 21 - 24 eV and 27 eV, respectively. Another interesting feature is the strong decline in electron counts above 50 eV. This effect was already predicted by Gan et al. (1990), and is also visible in Figure 2.4. Further following the trajectory of VEX in Figure 2.4, it can be recognized that the spacecraft crosses the same boundaries again on its way outward, even though these are less distinct due to the fact that the crossings now take place on the nightside.

While the dayside ionosphere is created by photoionization, the nightside ionosphere is formed in a more indirect way, generally by transport of charged particles from the dayside across the terminator. This means that the plasma configuration and properties probably differ largely between dayside and nightside. Usually the nightside ionosphere is

[1] The counts visible below 30 eV are due to photoelectrons expelled from the spacecraft surface.

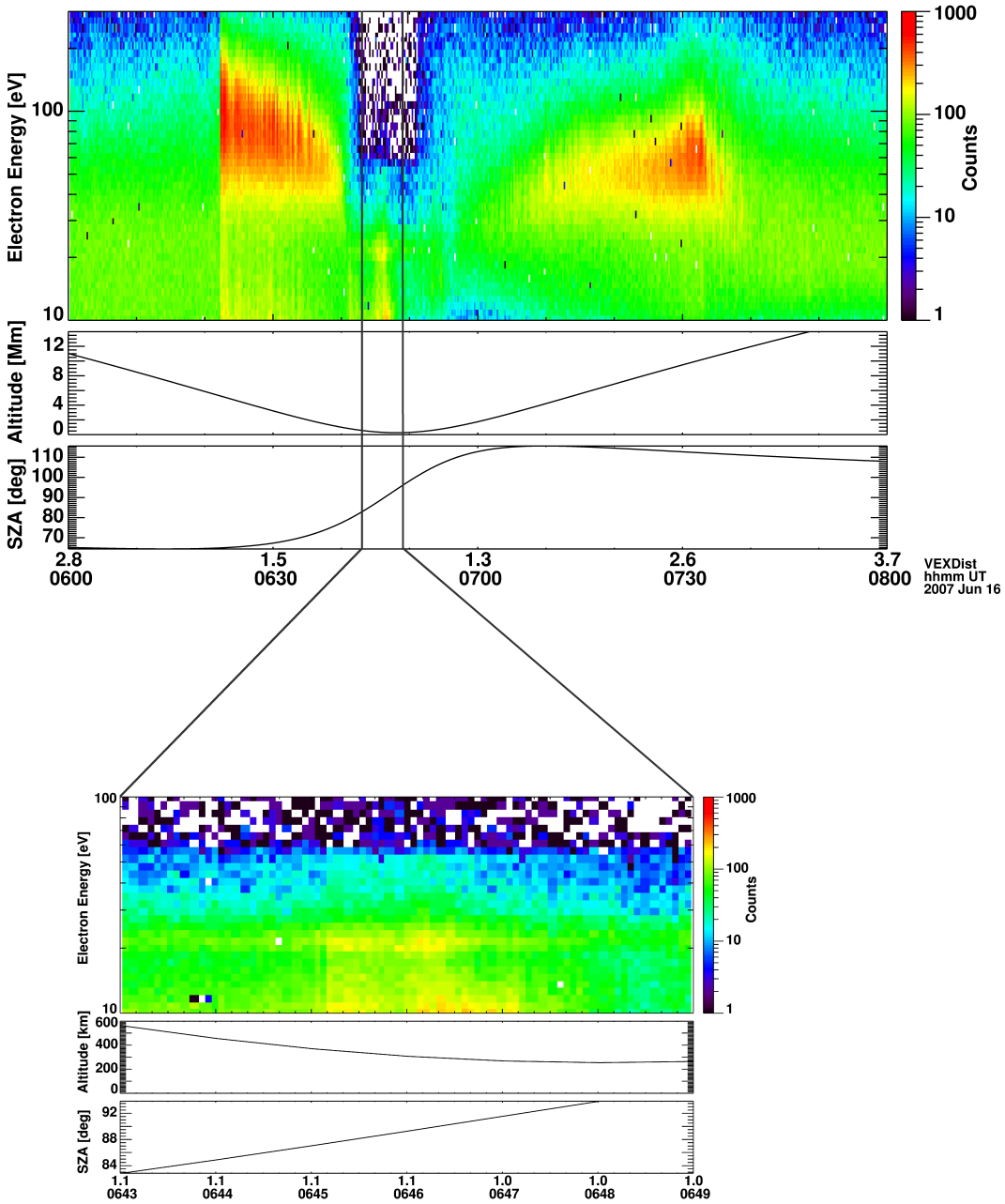

Figure 2.4: ELS electron spectrum versus time together with orbital parameters of Venus Express (altitude above the surface in Mm and solar zenith angle in degrees) for a full magnetosphere crossing. The lower part of the figure shows a magnified view of the ionospheric region. It is clearly visible that this in-situ ionospheric investigation takes place almost exactly at the terminator (SZA = 90°).

much more patchy, with electron clouds that may even be detached from the ionosphere (cf. Figure 1.17). Therefore the term "ionopause" might seem misplaced for nightside passes, and we decided to use the expression *photoelectron boundary* (PEB) instead.

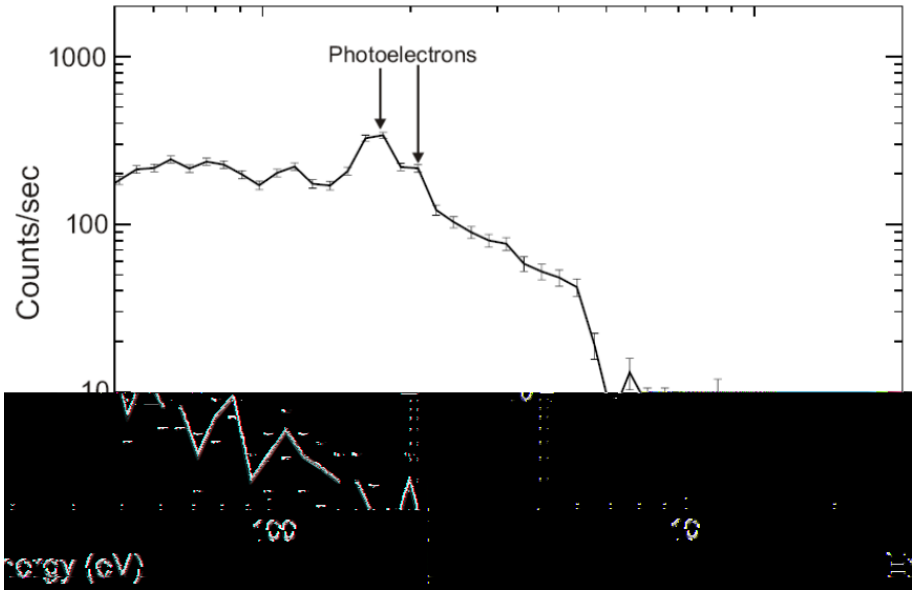

Figure 2.5: Photoelectron counts averaged over four minutes (60 spectra) from Coates et al. (2008). There are two very clear peaks, which generally constitute the typical ionospheric photoelectron band visible e.g. in Figure 2.4. Due to its high energy resolution, ELS was the first instrument able to detect these energy peaks at Venus, which had already been predicted in the past.

2.2.2 MAG measurements

In contrast to ELS in its normal operation mode, MAG is able to conduct three-dimensional measurements. This enables a thorough analysis of the direction of the magnetic field vector in different regions near Venus, including the configuration of the draped magnetic field. In our work, however, we often utilized only the absolute field magnitude measured by MAG, since this value is the most important indicator for the distinction of magnetized and unmagnetized ionospheric states. Figure 2.6 shows a typical set of MAG data, recorded during the same time range as for Figure 2.4 (upper panel). The coordinates are in the VSO system. One can also clearly recognize the plasma boundaries described for Figure 2.4 in the magnetic field data. The dayside bow shock crossing causes a strong jump, and the subsequent draping of the magnetic field lines appears as a gradual increase in field amplitude. Within the ionosphere, the magnetic field shows one single, sharp peak. This kind of configuration will be discussed in Section 2.5. The nightside bow shock is much less distinct than on the dayside also in the MAG data. Some field oscillations are visible near the bow shock crossing around 07:35, which might be due to Kelvin-Helmholtz instabilities or waves created by other mechanisms, which cause VEX to cross the fluctuating bow shock boundary several times.

It is difficult to recognize draping effects in VSO coordinates, since in the most helpful representation using the $x_{\mathrm{VSO}} - R_{\mathrm{cyl}}$ plane, $\mathrm{R_{cyl}}$ is always positive and therefore no negative vector components can be displayed. Thus another system proved more useful, namely the so-called CTP (cylindrical-tangential-planetary) coordinates. Any VSO vector is described in this system in the following way:

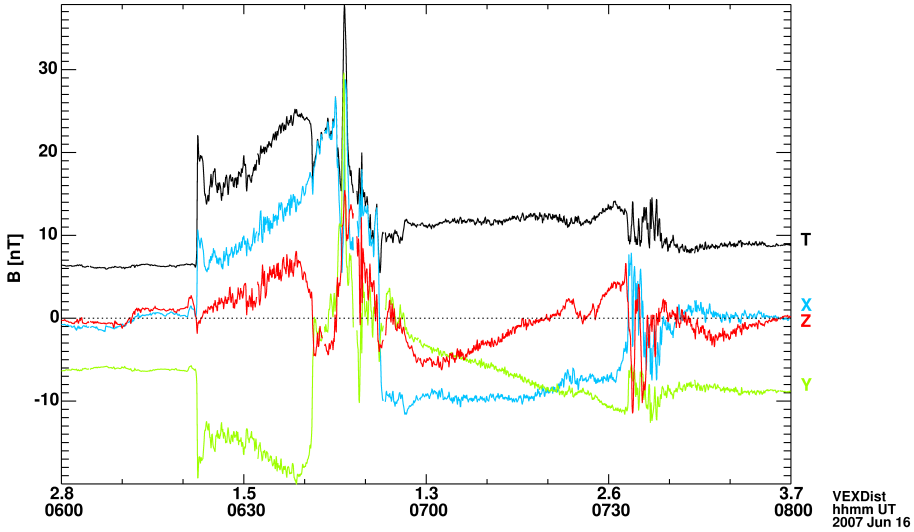

Figure 2.6: Magnetic field measurements over a full crossing of the magnetosphere. T indicates the total magnetic field amplitude, while X, Y and Z stand for the vector components in VSO coordinates.

$$\vec{x}_{\mathrm{CTP}} = \vec{x}_{\mathrm{VSO}}$$
$$\vec{y}_{\mathrm{CTP}} = \overrightarrow{\text{Venus-VEX}} \times \vec{x}_{\mathrm{VSO}}$$
$$\vec{z}_{\mathrm{CTP}} = \vec{x}_{\mathrm{CTP}} \times \vec{y}_{\mathrm{CTP}}$$

This means that if one plots the spacecraft trajectory within the x_{CTP}-z_{CTP} plane, it will be exactly the same as an x_{VSO}-R_{cyl} plot (cf. Figure 2.2). But in the CTP coordinate system, there is the additional advantage that now the magnetic field vectors measured along the orbit can be displayed as a projection onto the plane containing the Sun, Venus and VEX. The draping of the field lines is much clearer in this coordinate system, since the x_{CTP}-z_{CTP} plane is "attached" to the Sun-Venus line and just rotates around it, following the position of VEX. Assuming cylindrical symmetry of the plasma boundaries, the usage of this plane simplifies the view without neglecting any information delivered by MAG. Figures 2.7 and 2.8 show examples of magnetic vector plots within the mentioned plane. The draping of the field lines near Venus is clearly visible, but near the terminator and at low altitudes, some turbulence emerges. One should keep in mind that this figure does not show the amplitude of the magnetic field, but only its direction. These turbulent field configurations near periapsis were also observed in the PVO data (Elphic et al. (1980)), but only at times of high solar wind pressure. These results fit our present observations at solar minimum, where the solar wind pressure is relatively high as well.

2.2.3 Plasma boundary identification

Using the ELS and MAG in-situ data, one can now determine the different plasma boundaries. It is most helpful to combine both data sets to ensure a more precise identification of the boundaries. The most salient features visible in the data were already described in Sections 2.2.1 and 2.2.2. However, to give a complete overview, Figure 2.9 shows

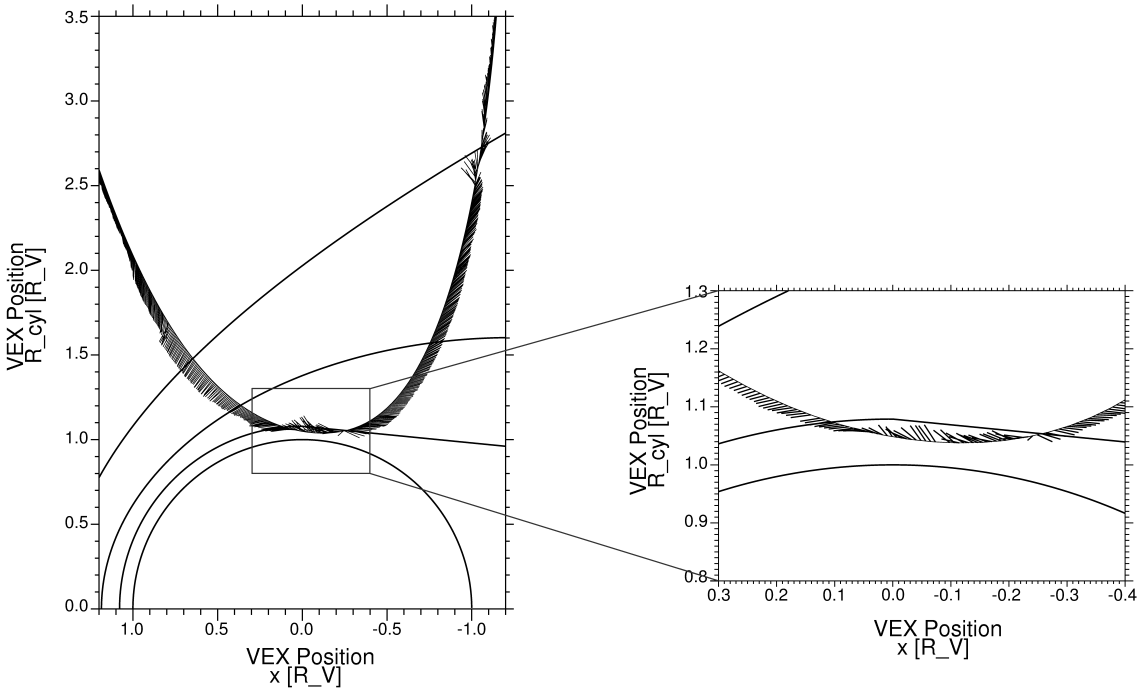

Figure 2.7: Magnetic field direction measured along the trajectory of VEX for the same time range as in Figures 2.4 and 2.6, displayed in the x_{CTP}-z_{CTP} plane. Spacecraft motion is from left to right, the periapsis lies 254 km above the surface. Each single line starting out from the VEX trajectory represents the magnetic field vector averaged over 12 seconds, each of them normalized to the same length. This means that the length of a vector projection indicates the true inclination of the vector with respect to the given plane. The semicircle in the plot on the left-hand side represents the surface of Venus, the three boundaries above (from bottom to top) correspond to average locations of the ionopause, the induced magnetopause (the upper boundary of the magnetic barrier), and the bow shock, taken from Martinecz et al. (2009). The plot on the right-hand side is a magnified view of the region near the Venus north pole.

both data sets together with the determined boundaries. Because this thesis focuses on magnetic fields in and near the ionosphere of Venus, the bow shock locations which we determined were not taken into account for our further research. Instead, we only used magnetic barrier and ionospheric measurements. Figure 2.10 shows all boundary locations determined from ELS and MAG data for the time range from May 2006 to August 2010. Generally, the magnetopause crossings are located above the ionopause/PEB in altitude, and the bow shock lies far above both of these boundaries. Because of the measurement limitations due to the orbital configuration of VEX, no data can be collected for the areas below the dashed line. Consequently, it is not possible to analyze the distribution of PEB locations on the dayside, since VEX does not sample these very low altitudes at some distance from the terminator. However, it can be seen that the PEB as well as the magnetopause seem to approximately follow a straight line extending into the tail of Venus. Since MAG data were only available until December 2009 at the time when this thesis was written, the boundaries after this date were determined only based on ELS data.

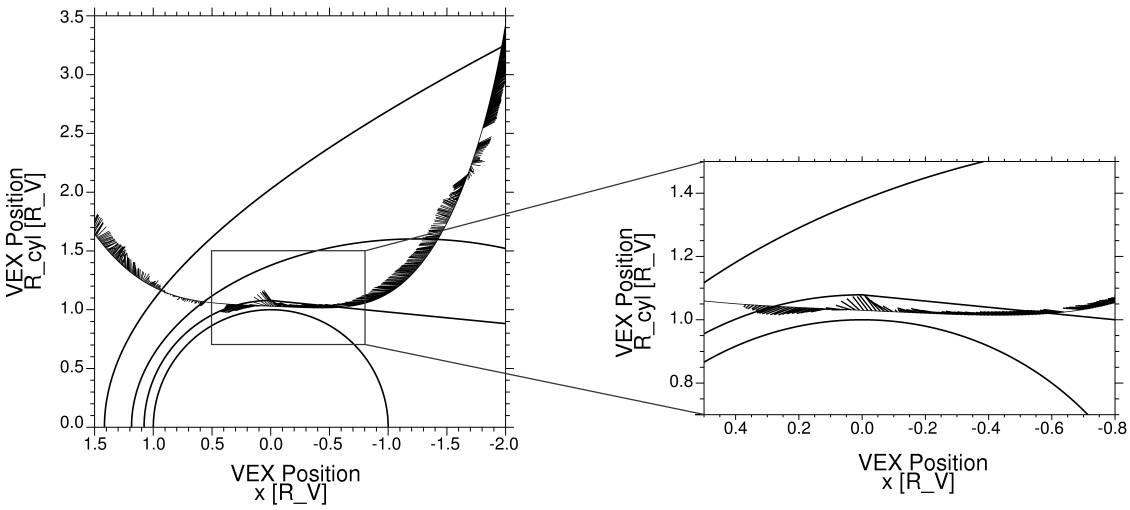

Figure 2.8: Another plot of magnetic field direction in CTP coordinates, measured along the VEX trajectory on 19th of October, 2009. This orbit had a much lower periapsis than the one in Figure 2.7 (174 km). Spacecraft motion is from right to left.

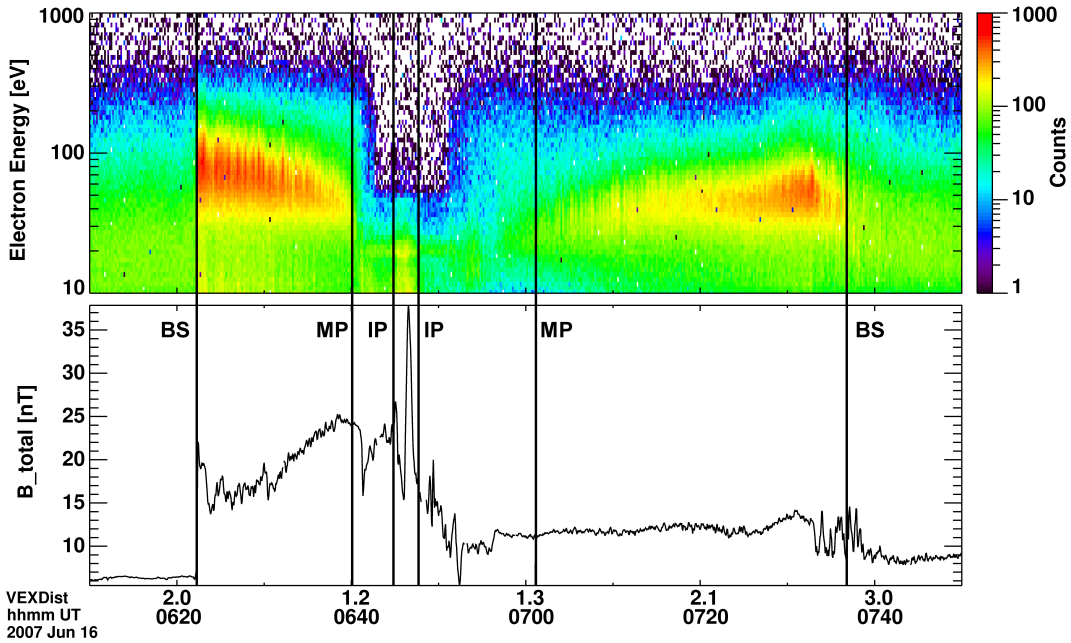

Figure 2.9: ELS electron spectrum and MAG total field amplitude. BS denotes the bow shock location, MP stands for the magnetopause and IP is the ionopause/PEB.

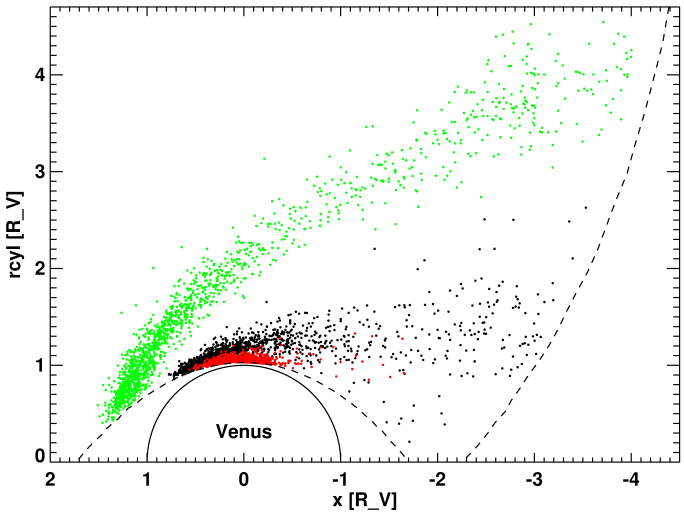

Figure 2.10: Bow shock (green), magnetopause (black) and ionopause (red) crossings in the VSO cylindrical system, the former two having been corrected for the solar wind aberration. The regions below the black dashed line were not sampled in situ by VEX.

As it is commonly done in the present scientific literature when handling larger amounts of data (e.g. Zhang et al. (1991) or Martinecz et al. (2008)), median values were used to identify the general trend underlying the scattered data points. The advantage of the median, compared to mean values, is that median values are less sensitive to single outliers, which often occur with Venus Express plasma data (e.g. in Figure 2.12).
For the determination of the median values, we always chose equally-sized intervals along the x axis. Within these intervals, the median of the x as well as of the y values of the data points was calculated and then plotted as a filled circle. Due to this procedure, the median values do not appear equally spaced along the x axis in the figure, but the interval size is actually constant within each plot.

2.2.3.1 Bow shock

The bow shock location can be identified as described in Sections 2.2.1 and 2.2.2. On the dayside it is usually very clearly defined, while on the nightside it looks more filamentary and less distinct. In Figure 2.11, only the bow shock crossings are displayed, together with the corresponding median values. These follow the typical planetary bow shock shape very well.

2.2.3.2 Induced magnetopause

Since the magnetic barrier separates the solar wind plasma flowing around Venus from the planetary plasma, its upper boundary, the magnetopause, can be identified both in the ELS and MAG data. As described in Section 2.2.1, on an inbound crossing, there is a clear decrease in higher-energy electrons ($\geq$ 30 eV), which marks the end of the solar wind plasma and thus the location of the magnetopause. Similarly, magnetic field effects are recognizable in the MAG data. As long as VEX is inside the magnetosheath, oscillations

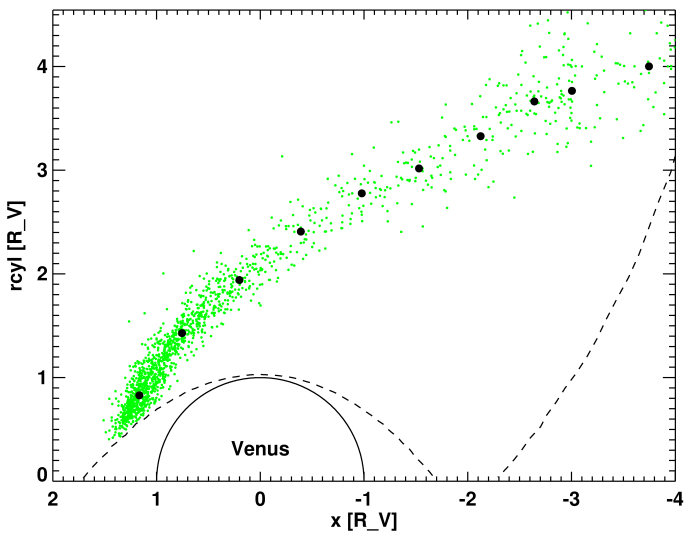

Figure 2.11: Aberration-corrected bow shock crossings (green) and median values (black).

in magnetic field amplitude are visible. These are due to waves embedded in the field which the solar wind plasma carries with it. At the inward crossing of the magnetopause, these waves suddenly disappear because almost no solar wind plasma enters this region[2]. This effect is sometimes not very pronounced, but it can be seen in Figure 2.9 especially for the inbound magnetopause crossing.

One might expect that the IMA detector on Venus Express is also helpful in identifying the transition region between solar and planetary plasma. However, since its temporal resolution is much lower than for ELS and MAG, it is not sufficient to resolve features during the brief crossings of the magnetic barrier and ionosphere. Therefore it was not taken into account for this study.

Figure 2.12 shows the same magnetopause crossings as Figure 2.10, but now with additional median values of the data which confirm the linear trend on the nightside. There are some outliers among the data points, which can be due to the misinterpretation of the measurements on some VEX orbits, but might also have physical reasons. These outliers can be found at larger SZAs as well as inside the tail. Since the magnetopause position is determined using higher-energy electrons as well as the magnetic field amplitude, one possible explanation is that sometimes energetic electrons and magnetic field lines are pushed into these regions for a short time. As VEX does not cross both the outlier region and the usual magnetopause range on one orbit, it is not possible to investigate the spatial distribution of plasma and magnetic field and find out why these unusual magnetopause positions are found. According to Figure 2.10, they are clearly below the bow shock, so there is no inherent contradiction.

[2]Depending on the direction of the IMF relative to the local bow shock, this is not always true. For a quasi-parallel bow shock configuration, these magnetosheath waves can invade the magnetic barrier region.

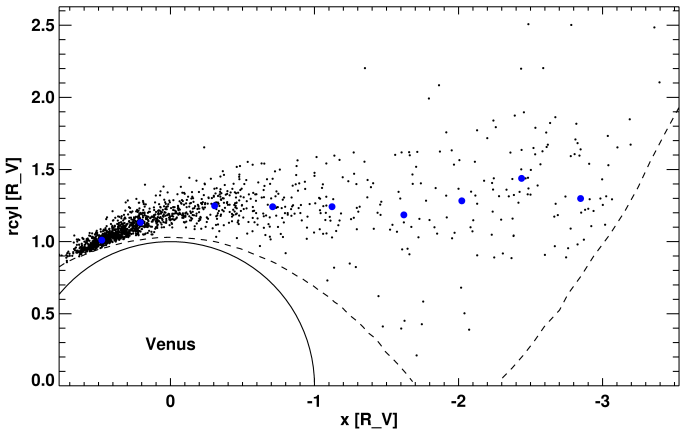

Figure 2.12: Aberration-corrected magnetopause crossings (black) and median values (blue).

2.2.3.3 Ionopause/PEB

As described in Section 2.2.1, we identify the ionosphere as the region in which the typical photoelectron band at energies between about 18 and 25 eV becomes visible. Since photoelectron production is correlated with plasma density, these electrons are expected to yield a general estimate of ionospheric particle density. Duru et al. (2009) proved that for the Martian ionosphere, the Mars Express ASPERA-3 ELS photoelectron band near 20 eV corresponds to a clear increase in electron density measured by MARSIS[3]. This sharp increase is also known from Venus observations and is generally accepted as a clear mark of the ionopause (Schunk and Nagy (2009)).
Figure 2.13 shows the PEB crossings alone, the blue circles representing median values again. As there are rather few data points on the nightside, the relation is not as certain, but similar to the magnetopause crossings, a linear trend seems probable. Especially the PEB altitude determination suffers from the limitations by the VEX trajectory; it is not possible to determine minimum or even average PEB altitudes towards the dayside using ASPERA-4 data.

2.3 Relations between plasma parameters

The plasma interaction processes at Venus are manifold and very complex. In this section, we attempt to shed light on some aspects by investigating possible relations between various parameters. Firstly, we looked at the heavy ion counts (these comprise all ions with $m/q \geq 8$, thus O^+ and heavier elements) detected by IMA below 700 km altitude above the planetary surface. They are displayed in Figure 2.14 for the whole time range from May 2006 to August 2010. There are some sinusoidal oscillations in the general course of these heavy ion counts in time, which according to their regularity must be due to spacecraft orbital effects. In Figure 2.15, the VSO x component of the spacecraft velocity at

[3]Mars Advanced Radar for Subsurface and Ionospheric Sounding (low-frequency radar instrument on Mars Express)

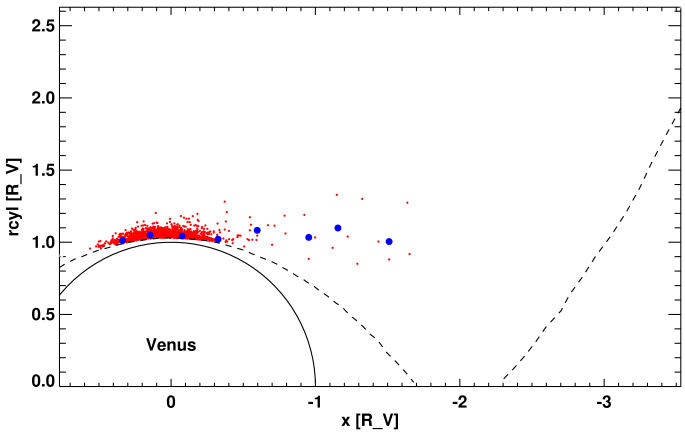

Figure 2.13: PEB crossings (red) and median values (blue).

its orbital periapsis is scaled to a similar range and then plotted over the heavy ion counts (black curve). Since the absolute velocity of VEX is very similar for all periapsis passes, we decided to use only the x component. We expect ion transport to mainly happen along the VSO x direction near the terminator, therefore it is important whether the spacecraft is flying with their direction of motion, in which case it will detect less ions due to the lower limit of the IMA energy range, or whether it is moving in the opposite direction and will thus collect also lower-energy ions. The spacecraft x-velocity variations at periapsis do indeed show a sinusoidal variation with about the same frequency as the one in the measured heavy ions. Therefore we subtracted the function represented by the black curve from the red data points, yielding the green points. While during the first part of the time range, until mid-2008, the green data points appear smoother than the original measurements, towards the end of the range some oscillations with a phase opposite to that of the black curve emerge. This means that the subtraction of the black curve removes a too large amount from each data point. However, there are other possible influencing mechanisms, for example the solar zenith angle of VEX at its periapsis, which is shown in Figure 2.16. In Figure 2.17, it is overlaid on the heavy ion data as a black curve, again scaled to an appropriate amplitude, and in analogy to the previous case, the green points represent the original data adjusted by subtraction of the SZA function. This time, the resulting points are much smoother, indicating that the variations are mainly induced into the heavy ion count rates by varying measurement SZAs, and that they depend only to a small degree, if at all, on the x velocity of Venus Express. Figures 2.18 and 2.19 also show a clear correlation of the median heavy ion counts with both the spacecraft x velocity and the periapsis SZA.

These figures already show the limitations that we will have to cope with in the coming sections: the data points are always very scattered, so one has to focus on mean or median values, and it is difficult to separate the influences of several external factors acting on the measured variables simultaneously.

Next, we investigated a possible relation between the heavy ion count rates and the magnetic field near Venus, since plasma transport is related to the magnetic field configuration. Therefore we determined maximum, minimum, mean and median magnetic field

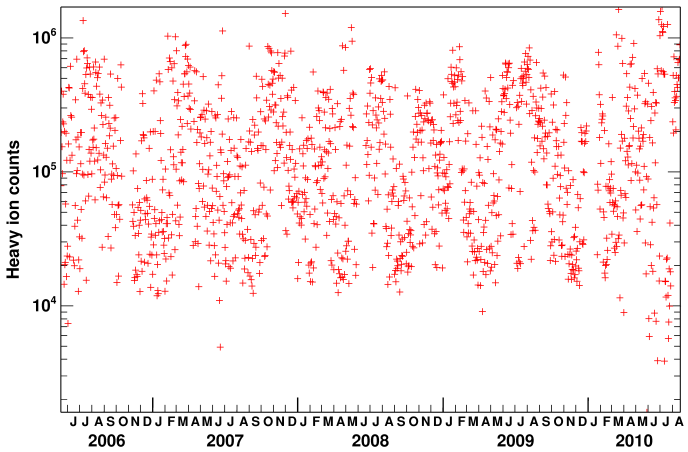

Figure 2.14: Heavy ions detected by IMA in the time range from May 2006 to August 2010. The numbers on the y axis correspond to the counts below 700 km altitude, each data point representing the measurements taken on one single orbit. The respective months are given as letters on the x axis for each of the given years.

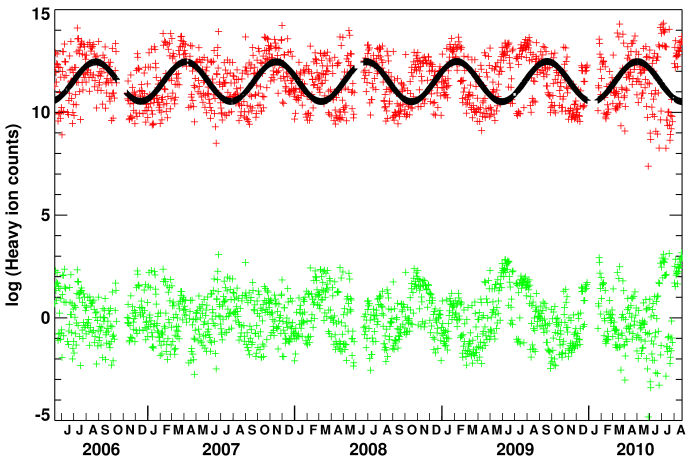

Figure 2.15: The red crosses indicate the same heavy ion counts as in Figure 2.14, whereas the black line stands for the x velocity of the VEX spacecraft, multiplied by a factor of -0.15 and increased by 25 in order to scale it to the heavy ion counts. In this way, the dependence between these two variables is better visible. The green crosses represent the result of the subtraction of the spacecraft x velocity from the heavy ion counts.

amplitudes within the altitude range from 700 km above the surface down to the VEX periapsis. While for three of these four variables, we did not find a correlation with the heavy ion counts, the maximum magnetic field does have a slight influence, as can be seen in Figure 2.20. The stronger the maximum field is, the more ions are seen by IMA. This probably means that these heavy ions are transported along the field lines, and thus trace the regions with large field amplitudes.
In Figure 2.21, we investigated the dependence of the heavy ion count rates on the $\vec{v} \times \vec{B}$ (Lorentz) force. The values on the y axis represent the absolute value of the cross

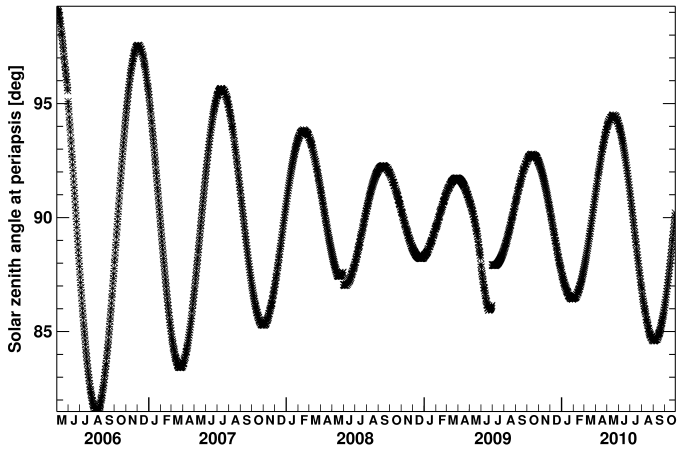

Figure 2.16: Variations of the solar zenith angle at the orbital periapsis of Venus Express.

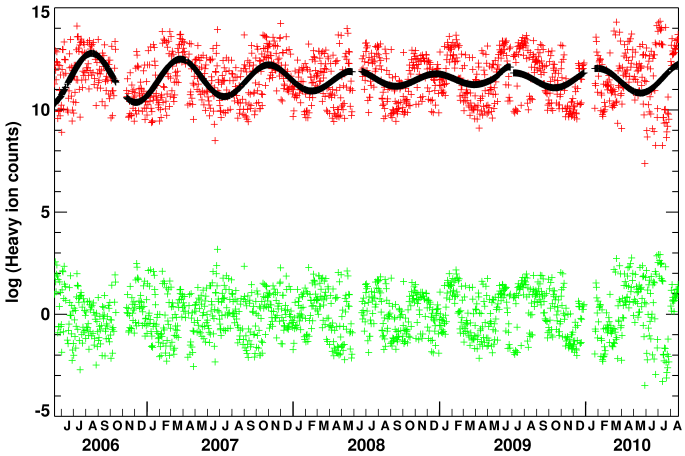

Figure 2.17: A similar plot as in Figure 2.15, but this time the black line represents the solar zenith angle of VEX at its orbital periapsis, scaled to fit the heavy ion data. Again, the green crosses correspond to the red crosses (heavy ion counts) minus the black line.

product of the solar wind velocity $\vec{v}$ and the IMF field vector $\vec{B}$, where the solar wind is assumed to propagate only along the Sun-Venus line. Both variables were averaged over two measurements (inbound and outbound) per orbit before their product was computed. As can be seen in the plot, there is no detectable dependence of the heavy ion counts on $|\vec{v}\times\vec{B}|$, which means that there is at most a very weak effect and other processes dominate in the investigated regions.

As described in Section 1.2.3, the ionopause/PEB of Venus varies in altitude, depending on the internal ionospheric thermal pressure and the external pressure acting on it. This can be clearly seen also from the ASPERA data, as shown in Figures 2.22 and 2.23. The external pressure consists of the dynamic pressure (inferred from IMA data) plus

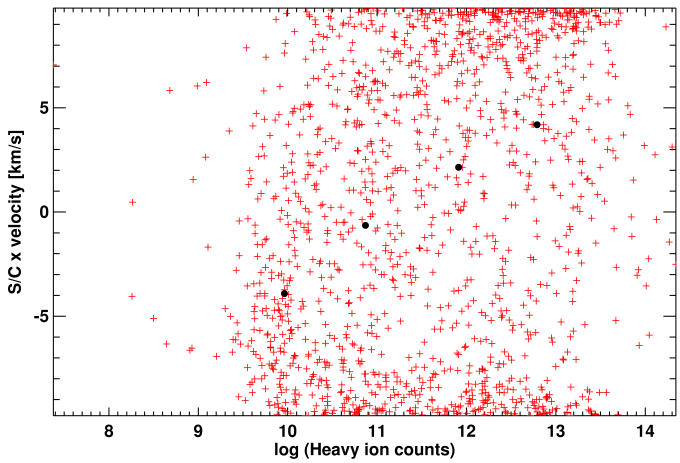

Figure 2.18: A direct plot of heavy ion counts versus the spacecraft x velocity.

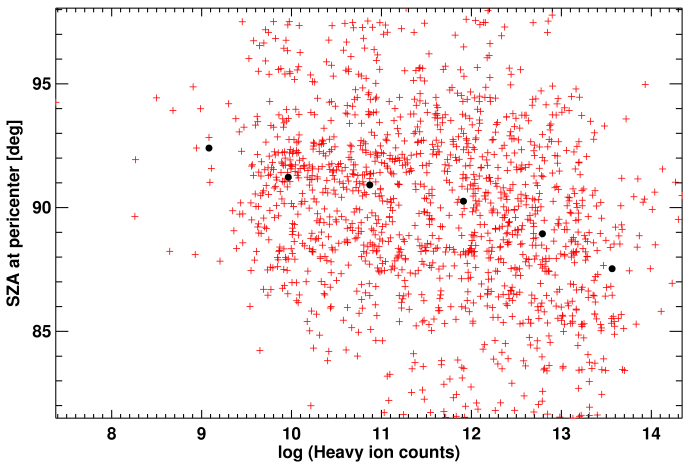

Figure 2.19: The dependence of the IMA heavy ion counts on the SZA of VEX at its periapsis.

IMF magnetic pressure (derived from MAG measurements)[4]. The EUV flux is based on measurements by the SEM instrument on the SOHO spacecraft (located near the Earth's Lagrangian point L1) which are then corrected for the location of Venus relative to the Sun. In the first of the two figures, there seems to be a strong dependence of the ionopause altitude on the external pressure for lower values, which then levels off at about 5 - 6 nPa. This saturation effect was already explained in Section 1.2.4.3. For the EUV dependence, a similar saturation occurs from about $2 \cdot 10^{10}$ photons/cm^{2}s upwards. Thus it seems as if the thermal ionospheric pressure does not increase any more above a certain radiation

[4]There is a third pressure contribution, namely the thermal pressure of the solar wind ($P_{thermal} = n_{SW} k T_{SW}$, see Equation 1.1). However, it is not possible to determine reliable values for the thermal pressure using VEX data. Furthermore, Burlaga and Ogilvie (1970) reported that its contribution to the total solar wind pressure is about the same as that of the IMF. This means that it constitutes only a small part of the bulk solar wind pressure which is dominated by the dynamic pressure (cf. Section 1.2.3).

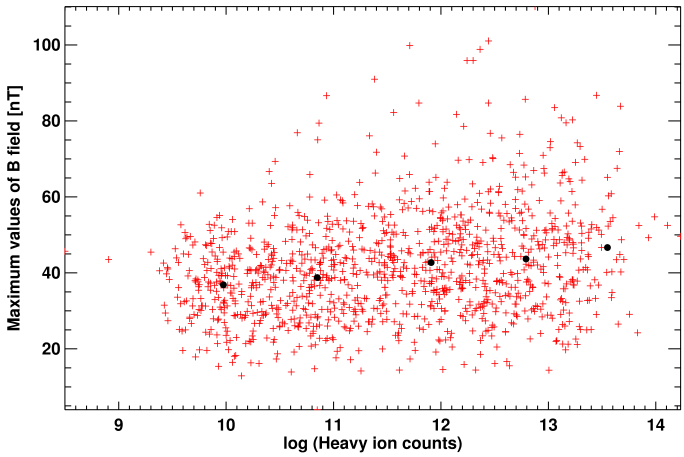

Figure 2.20: Heavy ion counts versus the maximum magnetic field detected near Venus. The red crosses correspond to the data points, while the black circles represent median values.

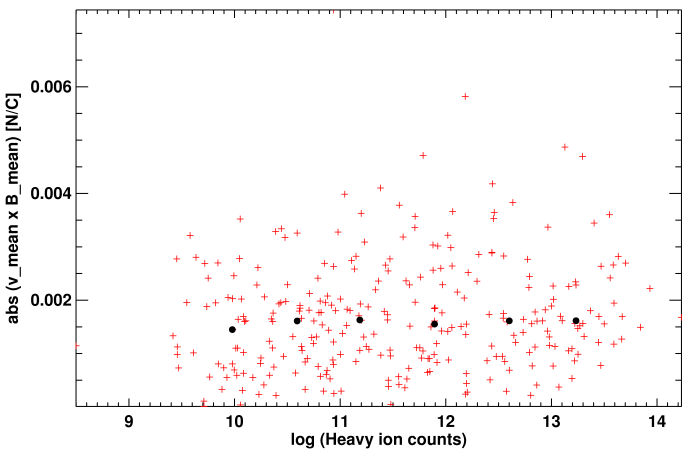

Figure 2.21: The absolute value of $\vec{v} \times \vec{B}$ (in Newton per Coulomb) versus the heavy ion counts detected by IMA. Red crosses are data points, black circles stand for median values.

energy input. Probably ionization is then balanced by losses, e.g. by recombination, such that the total amount of ions does not exceed this level. Theoretically, if the solar EUV flux was related to the inbound solar wind pressure, the limit in ionopause altitude for rising EUV radiation levels could be connected to an increase in external pressure, which in turn pushes the ionopause down. However, firstly there is no reason why these two variables should depend on each other, since the solar wind plasma takes several days to reach the Earth, while the radiation arrives after a few minutes, and secondly, we did not find any correlation between them in our data either. It is also known from solar physics that there is no straightforward correlation between the EUV flux and the solar wind.

Since VEX is conducting its in-situ measurements at varying planetary latitudes, the external pressure acting radially on the observed region is of course subject to changes, de-

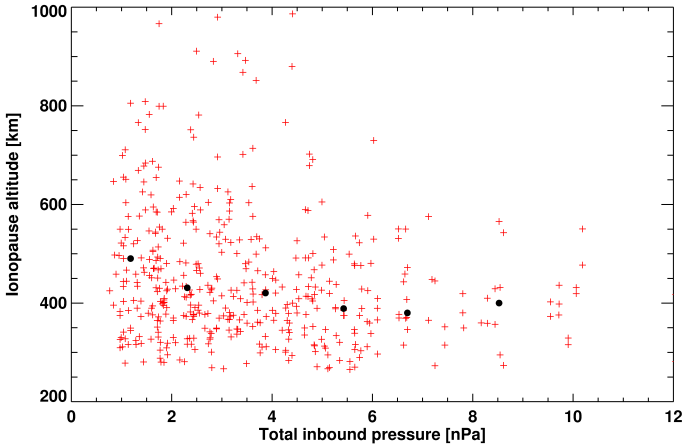

Figure 2.22: The dependence of the ionopause altitude on the external pressure contributions (solar wind dynamic plus IMF magnetic pressure). The data are given as red crosses, median values are black circles.

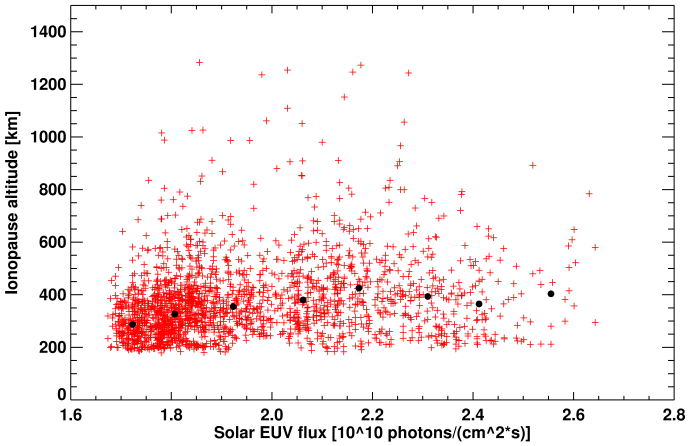

Figure 2.23: The dependence of the altitude of the ionopause on the solar EUV radiation intensity.

pending on the actual solar zenith angle. Figure 2.24 shows the ionopause altitude versus the external pressure, like in Figure 2.22, but now the plot extends to higher altitudes, and additional colours indicate the solar zenith angle at the respective ionopause position. This demonstrates that extremely high ionopause altitudes only occur on the nightside (SZA > 90°) and at the same time at low external pressures (which usually prevail on the nightside). Figure 2.25 represents a similar relation, but now with the magnetic field inside the magnetic barrier on the x axis. Again, the ionopause altitude clearly depends on the solar zenith angle as well as the external magnetic field. In Section 1.2.4.3, it was mentioned that the magnetic barrier takes up most of the incident external pressure, largely transforming it into magnetic pressure, which then acts on the ionosphere. This is why these two figures look very similar, even though they do not comprise exactly the same data points because it was not possible for all orbits to calculate both the external pressure

and determine the location of the magnetic barrier region. This relation brings us to the next plot, Figure 2.26. It shows all crossings separately, i.e. $P_{total} = P_{dyn} + P_{mag}$ was not averaged over inbound and outbound measurements, but taken directly, resulting in two values of P_{total} per orbit. Of course, if either P_{dyn} or P_{mag} were zero, the measurement was discarded because it would have resulted in unusually low pressure values otherwise. The colours clearly indicate that there is a separation in the dependence of external and magnetic barrier internal pressure at about 100°. It seems thus that a linear relation holds not only on the dayside, but even until shortly behind the terminator. From then on, however, a much lower fraction of the external pressure contributions is transformed into magnetic pressure, and there is at most a very weak dependence. This confirms once more that other processes dominate on the nightside, but up to and around the terminator region, the pressure balance scenario seems to apply, just like near the subsolar point. Unfortunately, the non-averaged (only either inbound or outbound) dayside pressure estimations are very scattered, but in order to compute average values, one would need two measurements per orbit, one of which is nearly always located on the nightside. This leaves us with either a small number of data points, or a rather scattered range of measurements due to zenith angle effects or to local and temporal fluctuations. Figure 2.27 shows our data set for the first case, i.e. only orbits were used for which both inbound and outbound measurements were available, and those were averaged to deliver only one mean value per orbit to reduce scattering.

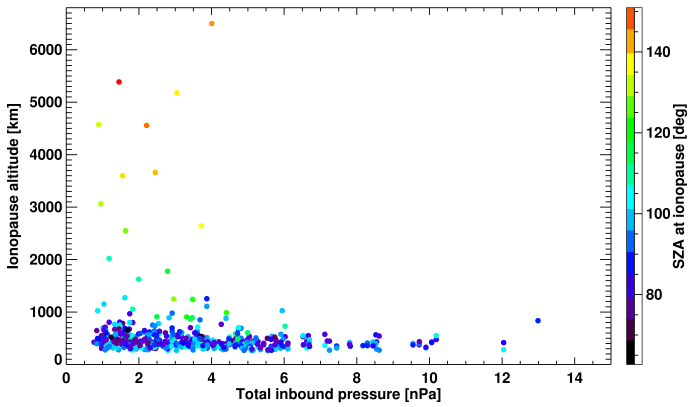

Figure 2.24: The altitude of the ionopause versus the external pressure (solar wind dynamic plus IMF magnetic pressure). The colours represent the solar zenith angle at each given ionopause location.

One can now establish a contrast by looking at the actual external pressure acting perpendicularly on the magnetic barrier. In Figure 2.27, there is a clear relation between the magnetic barrier field amplitude and the external pressure in the solar wind, even though the latter was not corrected for the mentioned zenith angle effect. This is shown again in Figure 2.28, where the magnetic pressure inside the magnetic barrier has been calculated from the measured field amplitude. This was done by averaging the magnetic field between the ionopause and the induced magnetopause, and then using the equation $P_{mag} = \frac{B^2}{2\mu_0}$, where B stands for the magnetic field amplitude, μ_0 is the vacuum permeab-

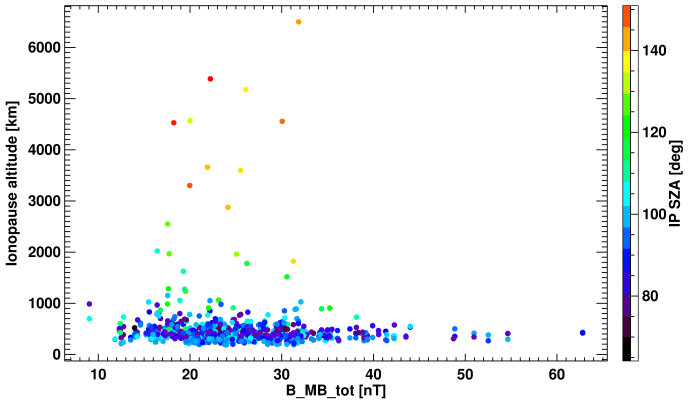

Figure 2.25: The dependence of the ionopause altitude on the magnetic field acting directly on it within the magnetic barrier region. Colours again stand for the SZA.

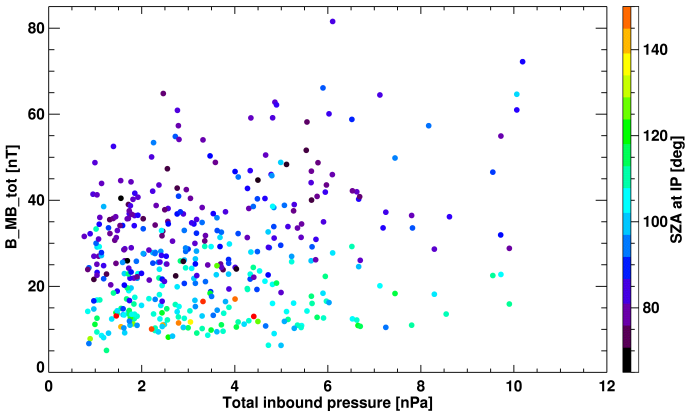

Figure 2.26: Magnetic barrier field strength versus external (solar wind dynamic plus IMF magnetic) pressure. Colours indicate the solar zenith angle, measured at the respective ionopause location, thus at the lower boundary of the magnetic barrier.

ility constant, and P_{mag} is the resulting magnetic pressure[5]. Its amplitude is found to be much lower than the solar wind pressure, only amounting to about 10% of its value. This confirms the general notion that the magnetic barrier is less strong at high solar zenith angles. However, the external pressure still has to be corrected for the appropriate solar zenith angle. The perpendicular component of the solar wind velocity is given by $v_\perp = |\vec{v}| \cdot \cos(\mathrm{SZA})$, thus the solar wind dynamic pressure ($P_{dyn} = \rho v^2$, with ρ the solar wind density and v its velocity) has to be multiplied by $\cos^2(\mathrm{SZA})$. For this calculation, we use the solar zenith angle at the magnetopause crossings of VEX which was calculated after taking the aberration into account. The IMF magnetic pressure is assumed to be independent of the angle of observation; however, directional effects will be discussed later (see Figure 2.32 and Section 2.6).

In Figure 2.29, the dependence of the magnetic barrier internal pressure on the SZA-

[5]In Equation 1.1, the magnetic pressure was given as $B^2/8\pi$, which is the correct form when using cgs units. In this case, however, we use SI units and therefore μ_0 has to be taken into account.

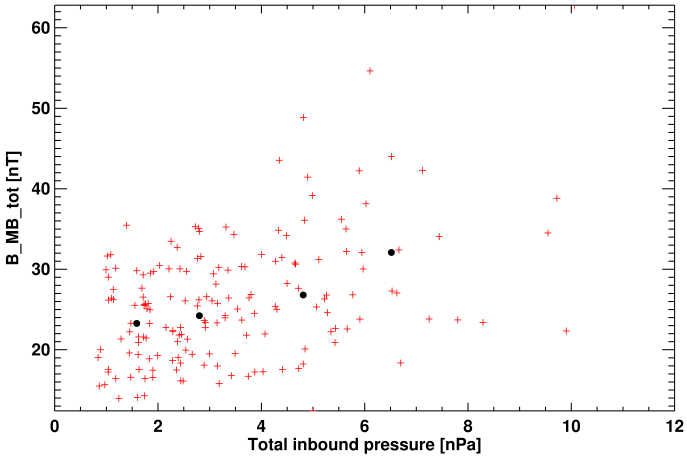

Figure 2.27: The magnetic field inside the magnetic barrier versus the external pressure measured in the solar wind. Red crosses stand for the data points and black circles for median values. The solar wind dynamic pressure was calculated from IMA data directly before the inbound and after the outbound bow shock crossing, while the IMF pressure is based on the magnetic field in the time range from 2.5 to 1.5 hours before and after the periapsis flyby of VEX.

corrected external pressure is displayed. Interestingly, there is no visible correlation any more. Our first idea to explain this was that the IMF pressure starts to dominate near the terminator, so that the total external pressure does not decrease as strongly with the rising SZA in this region as expected. However, while in the solar wind itself, according to our data, the mean contribution of the IMF is less than 1% of the dynamic pressure, even in the SZA-corrected data set the mean dynamic pressure is about 20 times as strong as that of the IMF. Thus there must be other contributions playing a role, e.g. solar wind thermal pressure or more complex processes like plasma instabilities. Surprisingly, the relation which was found between non-corrected external pressure and ionopause altitude (Figure 2.22) still holds after the SZA correction, as can be seen in Figure 2.30. This supports the hypothesis that the magnetic barrier is weakly developed near the terminator and the external pressure is transferred to the ionosphere via other mechanisms. Still, the magnetic barrier field does have a visible effect on the ionopause altitude, which is shown in Figure 2.31. We suppose that the draping near the pole creates a strong magnetic field which depends on the solar zenith angle, but not on the external pressure. The ionosphere in turn corresponds to this draping field as well as to changes in external pressure. In this scenario, the magnetic barrier pressure is created mainly by draping and does not depend strongly on the external pressure contributions, and most of the the external pressure is transferred to the ionosphere more directly and only a small fraction via the magnetic barrier as on the dayside. Furthermore, it is possible that the variations in the perpendicular component of the dynamic pressure are small due to the relatively small angular region being sampled by Venus Express. This can explain why both the external pressure as well as the magnetic barrier pressure have an influence on the ionopause altitude, even though they show no correlation with each other.

Because the orientation of the IMF also influences the penetration of magnetic fields into

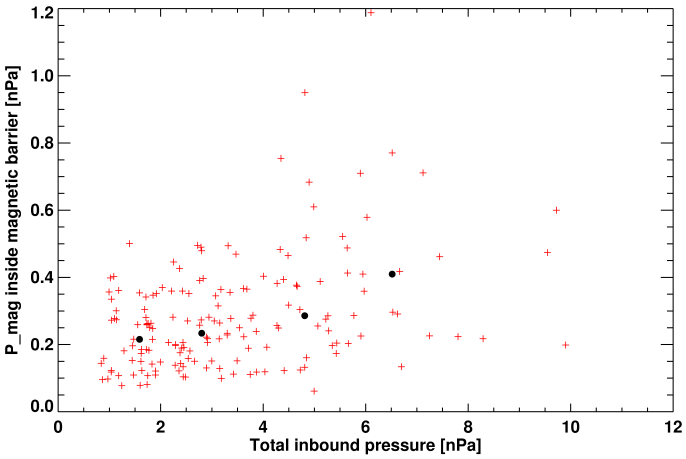

Figure 2.28: The dependence of the magnetic barrier internal pressure on the external solar wind and IMF pressure.

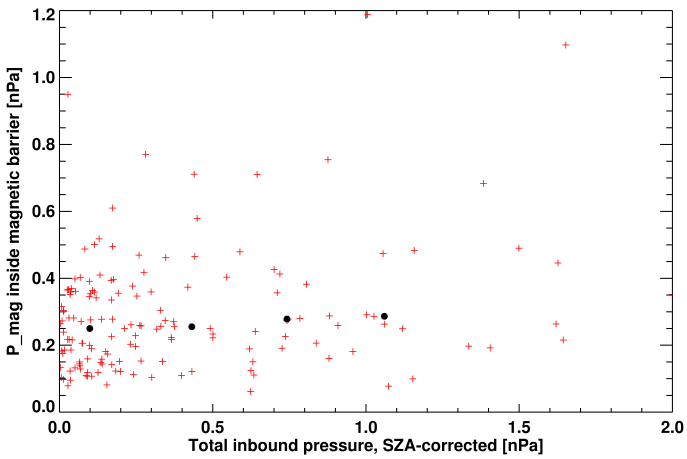

Figure 2.29: The same plot as in Figure 2.28, but now with the SZA-corrected external pressure displayed on the x axis.

the magnetosphere, we further investigated whether it has an effect on the altitude of the ionopause. However, as Figure 2.32 illustrates, there is no difference in ionopause altitude for changing IMF angles.

2.4 VeRa electron density profiles

In this section, a short introduction to the possibilities of a comparison between VeRa and ASPERA data will be given, including some examples. A real comparison is still to be done in the future when more density profiles are available.
VeRa is the radio-science experiment on Venus Express. In contrast to ASPERA-4, it is a remote-sensing instrument. When VEX is behind Venus, as seen from the Earth, its antenna emits a radio signal with a fixed frequency which then crosses the atmosphere

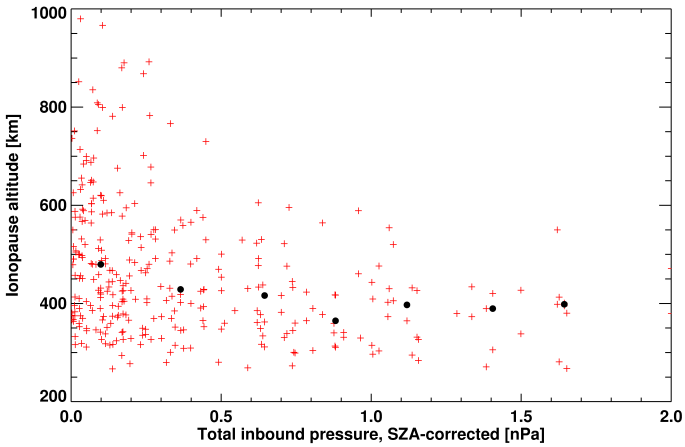

Figure 2.30: The dependence of the ionopause altitude on the SZA-corrected external pressure contributions.

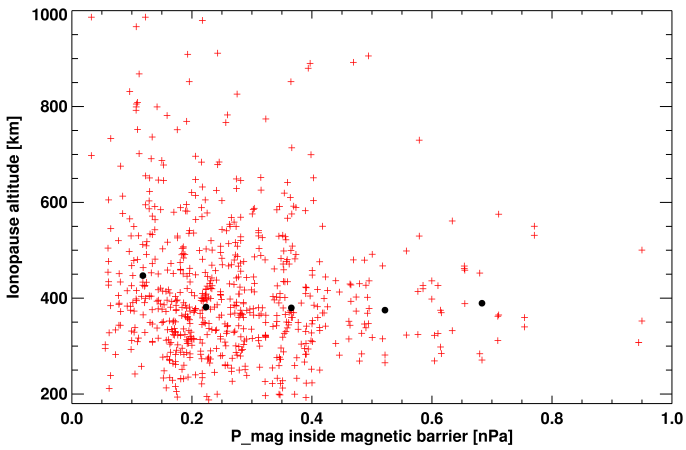

Figure 2.31: The response of the ionopause altitude to the magnetic barrier field acting on it.

and ionosphere and is finally received at Earth, as illustrated in Figure 2.33. This crossing affects the angle and frequency of the radio ray, and therefore allows the derivation of various atmospheric properties, e.g. density, pressure and temperature. In this way, density profiles can be measured not only for the neutral atmosphere, but also for the ionosphere, down to its base near 120 km, as in the example shown in Figure 1.16. Thus the ionosphere can be investigated down to much lower altitudes than in situ with ASPERA, and moreover, a clear ionopause location can often be determined. However, the geometrical conditions are very different for both measurement techniques. While ASPERA can only investigate the ionosphere around the orbital periapsis of VEX, and thus always near the terminator, VeRa measurements are conducted at various solar zenith angles. Furthermore, the in-situ measurements usually span an SZA range of several degrees already within the ionosphere because this region is crossed almost sidewards. With VeRa, on the other hand, the spacecraft does not move significantly during the short scan through all

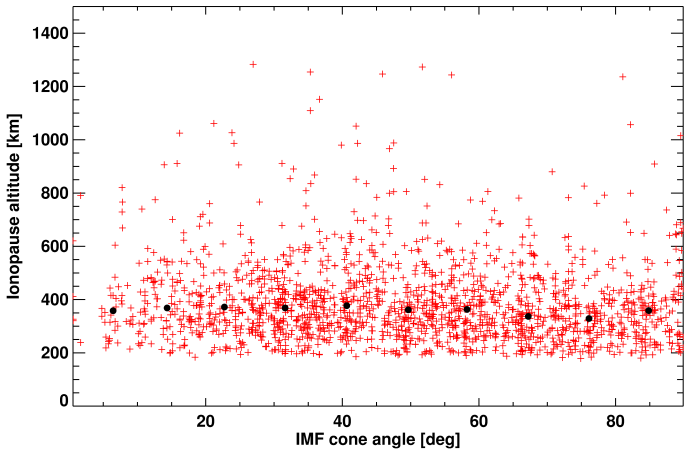

Figure 2.32: Ionopause altitudes and the angle between the IMF and the VSO x direction, the so-called IMF cone angle.

altitudes, which means that these measurements are done at an approximately fixed solar zenith angle instead of a broader range. Of course, the VeRa measurements usually focus on regions far away from the typical ASPERA investigation range. This puts severe constraints on the possibilities of a direct comparison of both techniques. Moreover, VeRa mainly detects electrons below the 5 eV threshold of ELS, so that no direct electron density comparison for the same energy range is possible. Nevertheless, the relative particle densities in different regions might be similar even for different energies, and since both methods can be used to determine the ionopause, a comparison of these locations is feasible.

Martin Pätzold and his group at the RIU (Rhenish Institute for Environmental Research) at the University of Cologne (Germany) provided us with eleven ionospheric electron density profiles derived from the VeRa radio occultation measurements. Two of them are shown in Figure 2.34. The ionopause is recognizable as a strong decrease in electron counts, visible at an altitude of about 255 km in the left-hand part of the figure and about 350 km in the right-hand panel. On the day when the first of these two profiles was recorded, the in-situ PEB crossings of VEX took place at an SZA of 91° and an altitude of 418 km (inbound) and at 83° and an altitude of 317 km (outbound). For the second profile, the in-situ PEB locations are at 470 km at 83° (inbound) and 1243 km at 108°. The ionopause is thus located at higher altitudes in the second case for both the ELS and VeRa data. While the ELS ionopause locations were originally identified in the same way as described in Section 2.2.3.3 (see also Figure 2.9), it is also possible to represent them in a similar way as the VeRa data, which is shown in Figure 2.35. The PEB locations mentioned in this paragraph can be recognized as a distinct decrease in electron counts, but in our impression, they are more clearly visible in the usual electron spectrum representation.

In Figure 2.36, it can be seen that the individual ionopause locations found with the ELS and the VeRa data both generally do not differ strongly, but it is not possible to give a more detailed statement yet without further analysis, especially since there is hardly any overlap between the data in the figure.

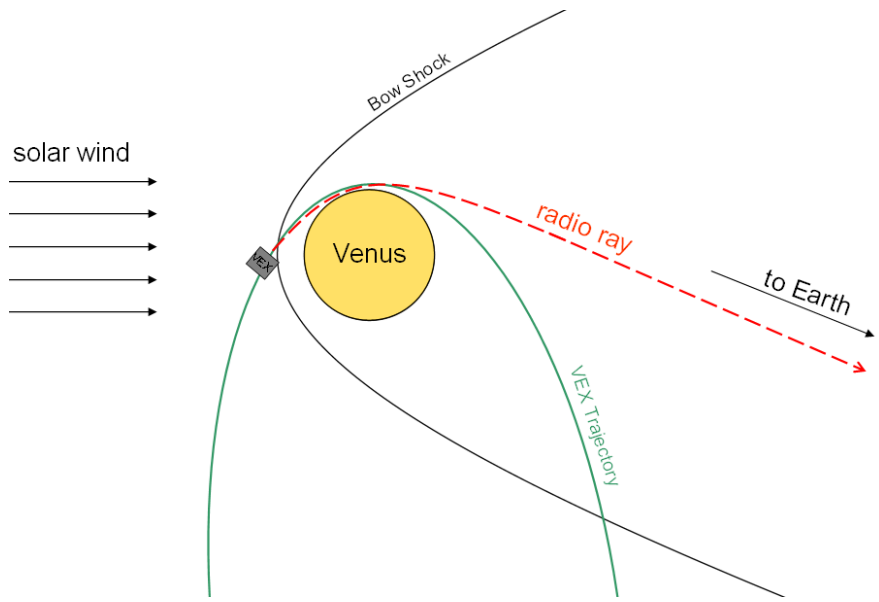

Figure 2.33: Sample geometry for a VeRa measurement near the terminator. The Venus Express spacecraft sends a radio signal into the atmosphere of Venus, which is then refracted and bent towards the Earth, where it is received and processed.

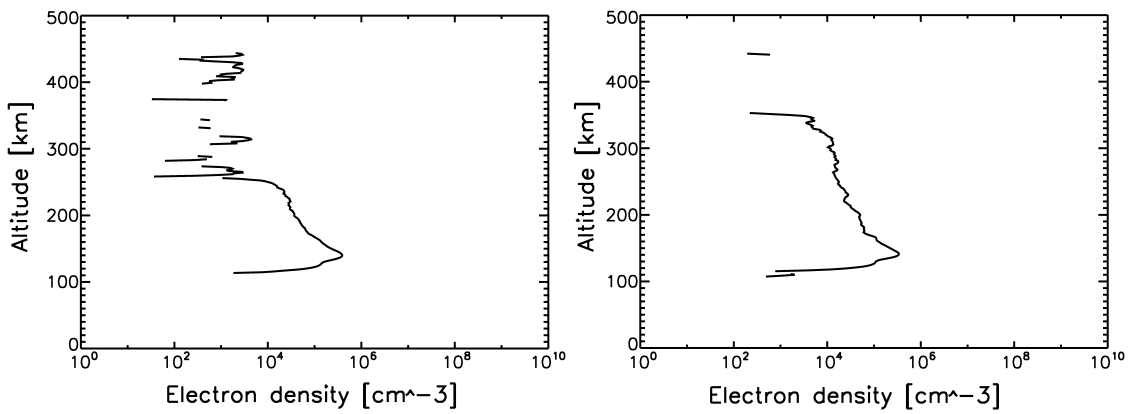

Figure 2.34: Two ionospheric density profiles derived from VeRa measurements. The left-hand profile was taken on July 15th, 2006 at a solar zenith angle of about 50°, while the right-hand data are from January 24th, 2007 (SZA = 60°). Note that VeRa, in contrast to ASPERA-4, is able to determine absolute electron densities.

2.5 Magnetization states of the ionosphere

In Section 1.2.4.3, a brief overview of the possible magnetization states of the ionosphere was given. This section is now dedicated to the description of our results regarding ionospheric magnetic fields by analyzing ELS and MAG data. We employed three different approaches, which will be explained below. It is important to keep in mind the orbital configuration of Venus Express, which allows access only to some parts of the most interesting plasma regions, and only to a thin region along the trajectory on each single

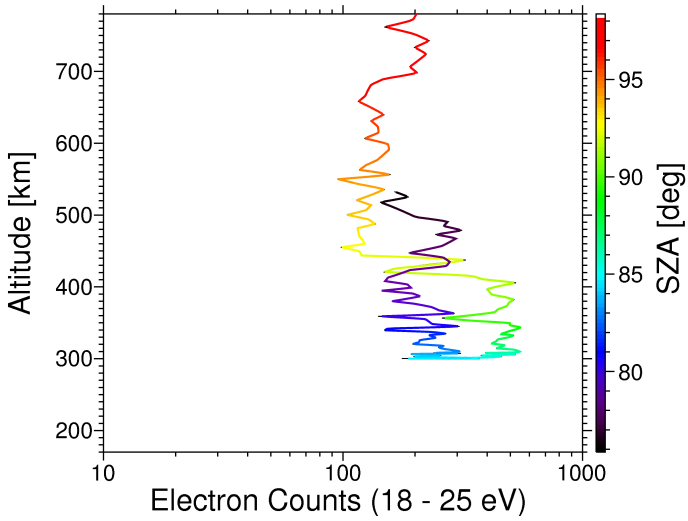

Figure 2.35: ELS data from July 15th, 2006 (the same orbit for which a VeRa profile was shown in the left-hand panel of Figure 2.34), plotted in the same representation as the VeRa profiles. Only electrons in the energy range between 18 and 25 eV were counted. Since the solar zenith angle range is very large compared to the radio-occultation measurements and therefore plays a significant role, the SZA was included in the figure as a colour scale.

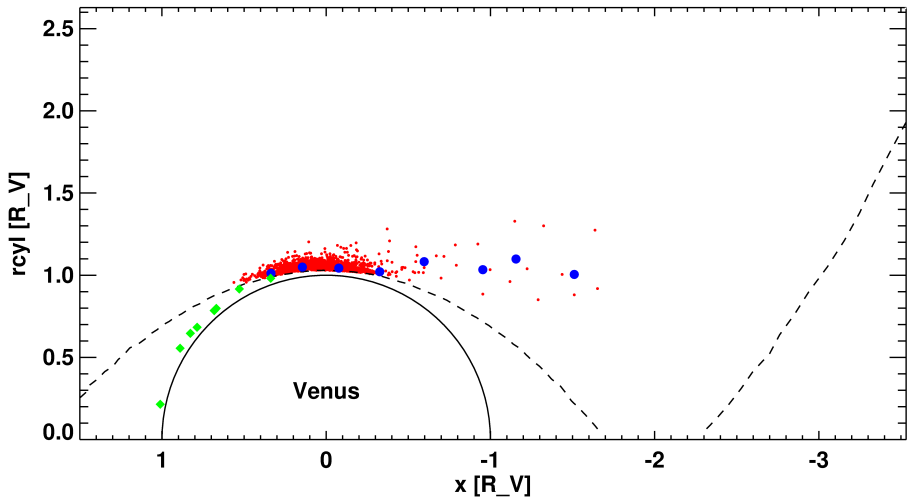

Figure 2.36: A plot of the same PEB locations as in Figure 2.13, but additionally including the VeRa ionopause altitudes (green diamonds) which we identified in the profiles. All of them are located in the dayside hemisphere.

orbit. A sample orbit of Venus Express was already presented in Figure 1.3, but this trajectory is not always constant and varies in periapsis altitude and solar zenith angle (cf. Figure 1.4). Before looking at the general statistics of magnetic fields in the ionosphere of Venus, or even single orbits, one should consider these variations. Figure 2.37 shows the VEX periapsis altitude over the whole measurement range from the beginning of the

mission. Letters stand for the months of the respective year, and the dashed line indicates December 31st, 2009. No offset-corrected MAG data after this date were available at the point when this thesis was written.

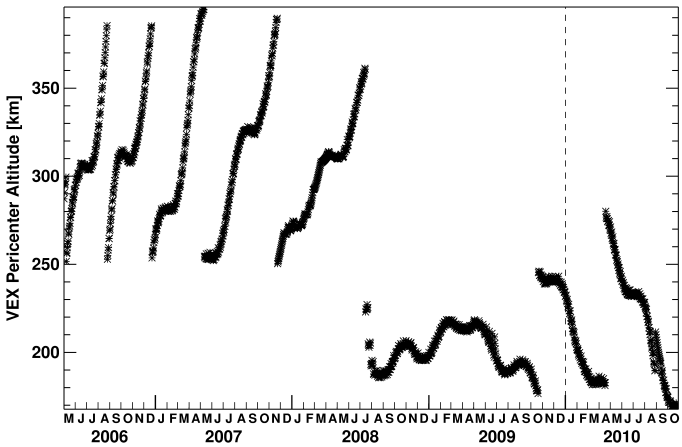

Figure 2.37: Variations of the VEX periapsis from May 2006 to October 2010.

2.5.1 Long-time averaged B fields

Our first ansatz to investigate the occurrence and strength of magnetic fields in the ionosphere of Venus was to use the MAG data to calculate long-time median magnetic field values in relation to the spacecraft sampling location. First, we created a plot of VEX SZA versus altitude, with bins of 50 km × 2° in size (Figure 2.38, left-hand side). For each single orbit, B/B_{max} is calculated for every bin crossed by Venus Express, and the median values of all measurements are displayed as colours for each bin in the figure. We decided only to regard measurements at SZA ≤ 90° since the pressure balance mechanism described in Section 1.2.4.3 probably does not apply on the nightside.
There is a clear tendency for strong magnetic fields to appear at low altitudes. Within this low-altitude range, the observable solar zenith angle values are restricted to ≥ 50°. Figure 2.39 is very helpful in interpreting the general median magnetic field value distribution, since the detected fields in the bins can now be set into relation to the measured ionopause altitudes. Firstly, in the solar zenith angle range under consideration, practically all ionopause locations of Figure 2.39 lie below 1000 km in altitude. Thus the strong magnetic fields found in the median bins very likely relate to the ionosphere, either directly via ionospheric magnetization, or indirectly in the form of magnetic pressure acting on the ionosphere from above. While the median value of these ionopause locations even decreases between 60 and 90° due to a selection effect because of the orbital configuration of Venus Express, the scattering gradually grows towards the terminator, which means that there are more ionopause locations found at higher altitudes. This is due to the fact that the local radial component of the solar wind dynamic pressure strongly declines towards the terminator. Thus the total external pressure acting on the ionopause decreases, exacerbating the penetration of magnetic fields into the ionosphere. For the high-SZA regime, the largest relative magnetic field values in Figure 2.38 are not found at the lowest

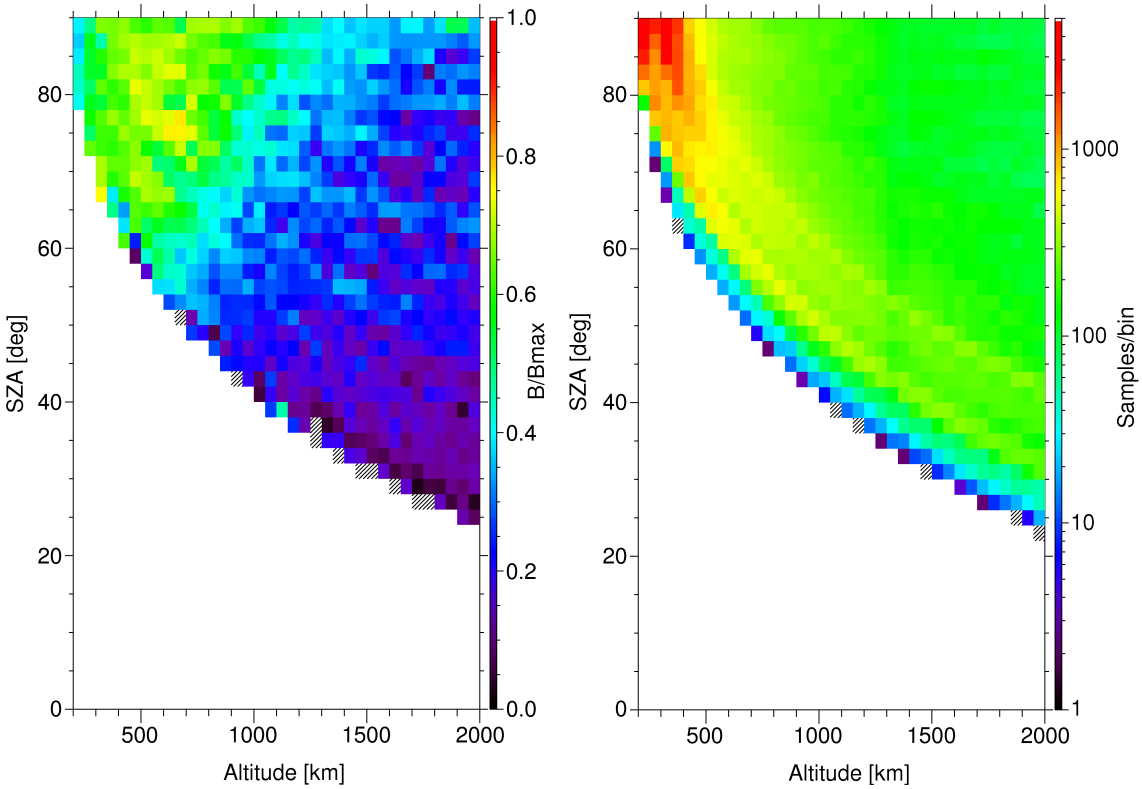

Figure 2.38: Left-hand side: median values of B/B_{max} for all orbits from May 2006 to December 2009, where B_{max} stands for the maximum magnetic field value on the respective orbit. The bin size is 50 km$\times$2°. Right-hand side: number of measurements taken into account for each bin in the left-hand figure. This representation indicates which median values are statistically significant.

altitudes any more. Instead, it appears as if either only the upper part of the ionosphere is magnetized, leaving its lower portion field-free, or the full ionosphere is magnetized by a different mechanism than the pressure balance only when the ionopause reaches high altitudes. From this figure, we cannot determine which of the two possibilities applies, although the first one seems more probable. Since the number of measurements per bin is very high in the low-altitude, high-SZA region, this effect must be real.

Figure 2.40 shows a magnification of the region containing strong magnetic fields, using smaller bin sizes. The general structure of the magnetic field distribution remains the same, but more fluctuations become visible. In order to separate the dependence of the magnetic field on altitude and solar zenith angle, we created plots of the magnetic field versus altitude for a fixed solar zenith angle (Figure 2.41) as well as representations of magnetic field versus SZA for a fixed altitude (Figure 2.42) by making horizontal and vertical cuts across Figure 2.40. This yields some hints about the regions in which strong magnetic fields are located on average, but it is not possible to directly separate the coordinate dependence. Nevertheless, these illustrations of the median magnetic field give a good impression of the distribution of these fields in and near the ionosphere, and also of their strong variability. Therefore it makes sense to look at individual orbits and try to

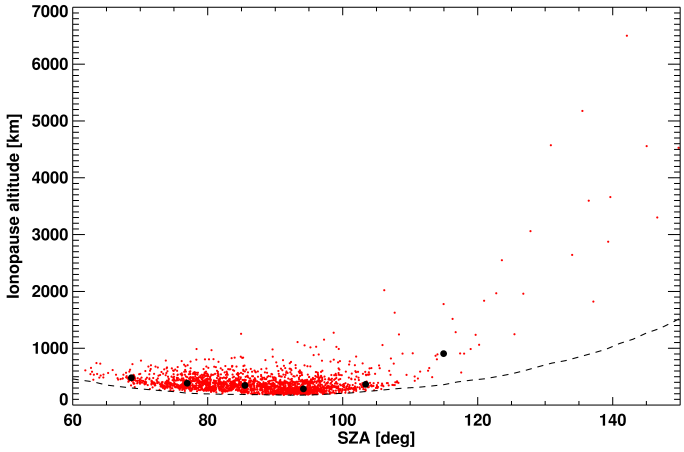

Figure 2.39: The same ionopause crossings as in Figure 2.13, but now simply plotted in terms of altitude and solar zenith angle instead of VSO coordinates. Red dots are the data points, black circles indicate the median values and the black dashed line represents the boundary below which Venus Express did not conduct any in-situ measurements.

find characteristics and the dependence of these magnetic fields on internal and external influencing factors. This will be done in the following section. To give a measure of the absolute field amplitude, Figure 2.43 shows the distribution of median values of B_{total}. Again, higher field values (30 - 45 nT) are found near lower altitudes, but at SZA > 80°, where altitudes down to 200 km become accessible, the magnetic field declines in this low region. The area with even stronger magnetic fields (50 - 60 nT) on the margin of the measurements is statistically not well covered (see right-hand panel of Figure 2.38), and therefore it is unclear whether this effect is real.

2.5.2 Manual sorting and cross-correlation method

Going back to the direct comparison of the detection of relative photoelectron density and magnetic field amplitude as presented in Figure 2.9, there is a very simple and straightforward way of investigating magnetization states. In this kind of plot, one would expect to detect high electron count rates in the energy range of 18 - 25 eV (indicating that VEX is crossing the ionosphere) and at the same time measure either low (unmagnetized case) or high (magnetized case) magnetic field amplitudes. This configuration was indeed observed in many orbits, and we used it to manually sort these cases by their magnetization states. In order to get a more quantitative measure for this classification, we added five new panels to the plot of Figure 2.9. Two of the new panels simply show the altitude and solar zenith angle of VEX to give an impression of the observation geometry. The third new panel splits up the magnetic field into one radial and one horizontal component, seen with respect to the surface of Venus. The fourth additional panel contains the electron counts only within the energy range of 18 - 25 eV, together with a smoothed version of these data. Finally, the fifth new panel represents a *cross correlation* between these smoothed electron counts and the magnetic field amplitude. For a magnetized iono-

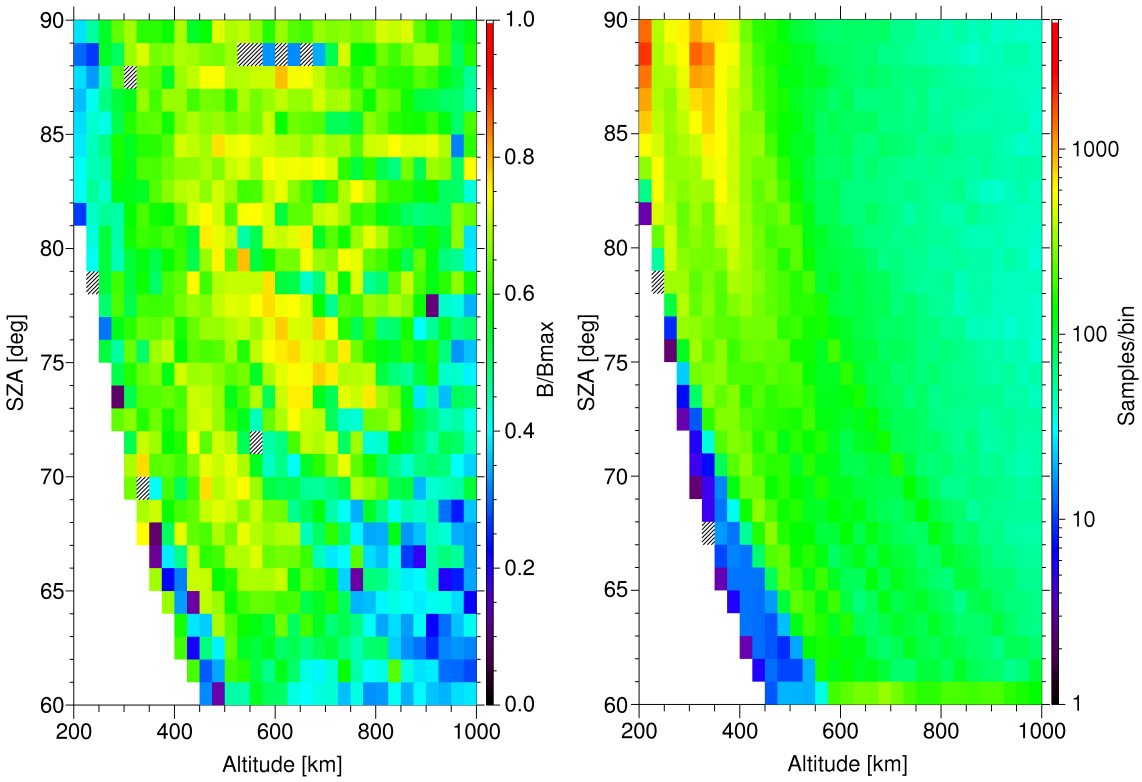

Figure 2.40: The same plots of B/B_{max} and the number of data points for each bin as in Figure 2.38, but now focusing on the region containing the most interesting magnetic features. The bin size is 25 km $\times$ 1°.

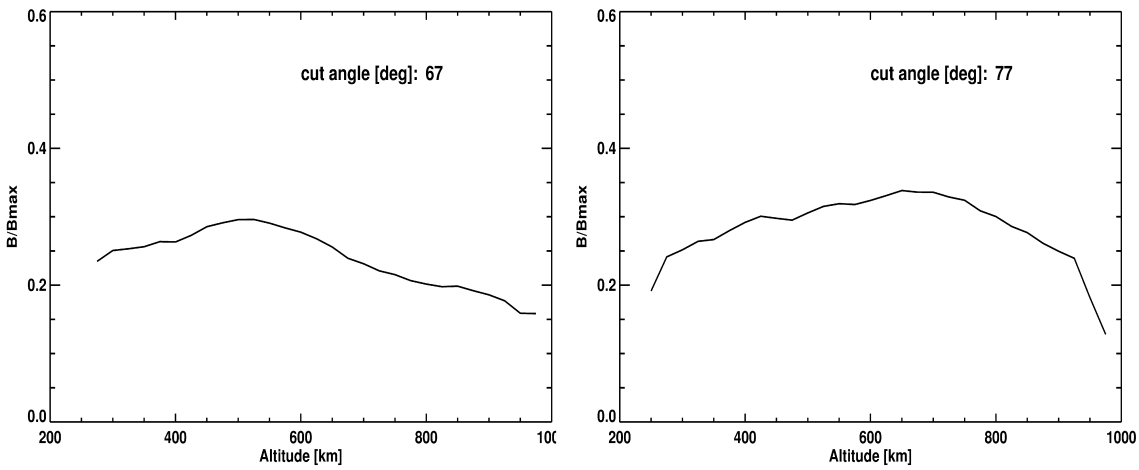

Figure 2.41: Two cuts across the left panel of Figure 2.40 at fixed solar zenith angles of 67° (left-hand side) and 77° (right-hand side). The y axis shows the value of B/B_{max} and the x axis represents the corresponding altitude.

sphere, this cross-correlation should be clearly positive because high electron count rates (due to VEX being located inside the ionosphere) should coincide with high magnetic

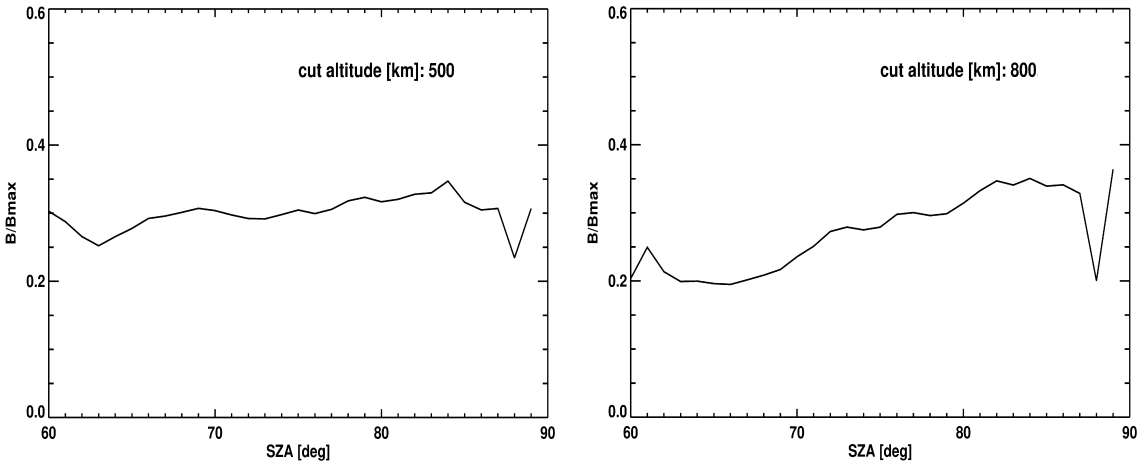

Figure 2.42: Two cuts across the left panel of Figure 2.40 at fixed altitudes of 500 and 800 km. The x axis gives the solar zenith angle, the y axis B/B_{max}.

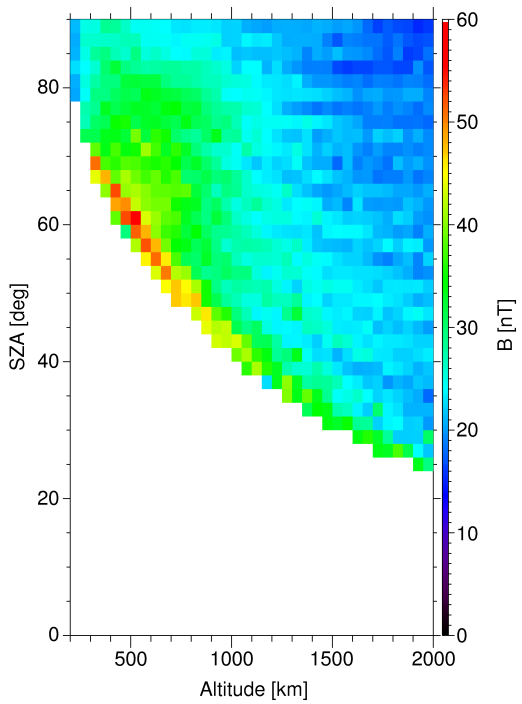

Figure 2.43: Median values of the absolute magnetic field amplitude measured from May 2006 to December 2009. The number of data points per bin is the same as in the right-hand part of Figure 2.38.

field values. In an unmagnetized case, on the other hand, the cross-correlation is expected to be negative since the magnetic field is low in regions of dense plasma and high in flux ropes which are void of plasma when they are in pressure balance. This relation will be investigated in the next section.

The two magnetic field components support the tendency which was already visible in

Figures 2.7 and 2.8, namely that the ionospheric field tends to be horizontally orientated. This agrees with the field configuration described by Luhmann and Cravens (1991) for magnetized cases. For the flux ropes in an unmagnetized ionosphere, however, the first theoretical predictions and measurements led to the conclusion that they can be pointing in any direction and the field configuration within these regions is rather complex (see Russell and Elphic (1979) and Figure 1.25). We found a prevalence of the horizontal field component for most of the orbits, which means that this cannot be just a coincidence for the case presented here. Instead, due to the proximity of the VEX in-situ measurements to the terminator, probably most of the flux ropes extend in a direction parallel to the VSO x axis. These will also usually be crossed longitudinally or only with a slight inclination because the VEX orbit lies almost in the VSO x-z plane. Elphic and Russell (1983a) analyzed a set of PVO flux rope detections which they separated into measurements taken at SZAs above and below 45°. They reported that flux ropes within the high-SZA subset are randomly distributed below 300 km altitude, but above 300 km, horizontally-orientated flux ropes dominate. This trend agrees with our findings, since VEX is conducting its measurements at large SZAs and often only above 300 km altitude. The statistical distribution of flux rope orientations in various altitude intervals is an interesting investigation which can be done in the future.

2.5.2.1 Sample plots of magnetized and unmagnetized states

These cross-correlation properties were indeed found for a large number of VEX orbits. Figures 2.44 and 2.45 show examples of a magnetized and an unmagnetized ionospheric state, respectively. It is visible that within the time of the ionosphere crossing, in both cases the cross-correlation function behaves as expected: in the magnetized example (Figure 2.44), during the pass of VEX through the ionosphere from approximately 4:55 to 4:58, the magnetic field remains high, leading to a clearly positive cross-correlation function. When evaluating these observations, one has to keep in mind that Luhmann and Cravens (1991) described the field configuration for magnetized states as having a minimum near 190 km altitude and a maximum at about 170 km, as was mentioned in Section 1.2.4.3. Since the periapsis of VEX was located at much higher altitudes for most of the mission time up to now, we do not have a large amount of data for this altitude range yet. But we observe strong magnetic fields even at larger altitudes, which is consistent with the PVO observations presented by Luhmann et al. (1980) for magnetized states. The unmagnetized example in Figure 2.45, on the other hand, represents a very typical case of the opposite state, and even contains a possible flux rope, namely the peak in magnetic field amplitude near 01:58:30. Within this small region, it is also clearly visible that the local electron count rate is lower than in the rest of the ionosphere. This indicates that the local plasma is pushed out of this magnetic tube by magnetic pressure. Except for the flux rope, the magnetic field strength is very low from 01:57 to 02:01, the same time in which a strong ionospheric photoelectron band is observed.

The described characteristics were seen for a large number of orbits. After excluding measurements for which ELS or MAG data were not available, as well as those where no clear photoelectron band was visible, 526 of 846 orbits could be clearly classified.

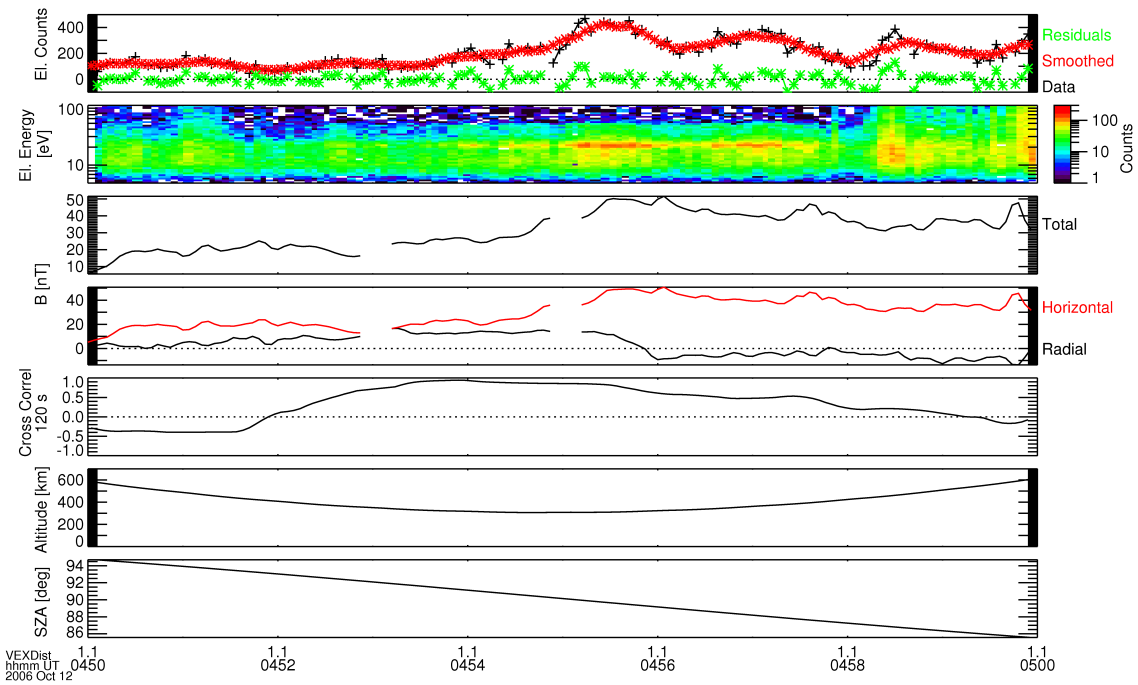

Figure 2.44: An example of a typical magnetized state. The time range comprises only ten minutes, mainly around the VEX ionosphere crossing. The uppermost panel contains the electron counts within the energy range of 18 - 25 eV (black), a smoothed version of these data (red) and the residuals (real data minus smoothed data) in green colour. The second panel shows the electron spectrum and the third panel contains the magnetic field strength, which is separated into two components (radial and tangential to the surface of Venus) in the fourth panel. In the fifth panel, the cross correlation described in the text is displayed. The two lowest plots show the altitude and solar zenith angle of the VEX spacecraft.

The remaining non-classified orbits often have a magnetic field amplitude around 20 nT and probably represent transitional states from a magnetized to an unmagnetized case, or cases in which the external pressure is too low to cause a strong field in the ionosphere, but too high to leave it essentially unmagnetized. Some examples of these “transitional cases” will be shown and discussed in Section 2.5.2.2.

In our analysis, it turned out that the cross-correlation function alone does not always determine the magnetic state correctly. The agreement with the orbits that were sorted manually is about 76%. Possible reasons for this are fluctuations in magnetic field strength for unmagnetized orbits with very low magnetic field values, in which case small absolute changes correspond to strong relative changes in field amplitude. Furthermore, there are sometimes gaps in the MAG measurements which change the cross-correlation function, although the state can be identified clearly with the naked eye. It could help to exclude these cases from the study, but this would strongly decrease the number of orbits which can be evaluated. Similarly, there are sometimes gaps in the photoelectron band which might be due to flux ropes and cause jumps in the cross-correlation function. This procedure thus still has to be amended and improved. For this study, we decided to

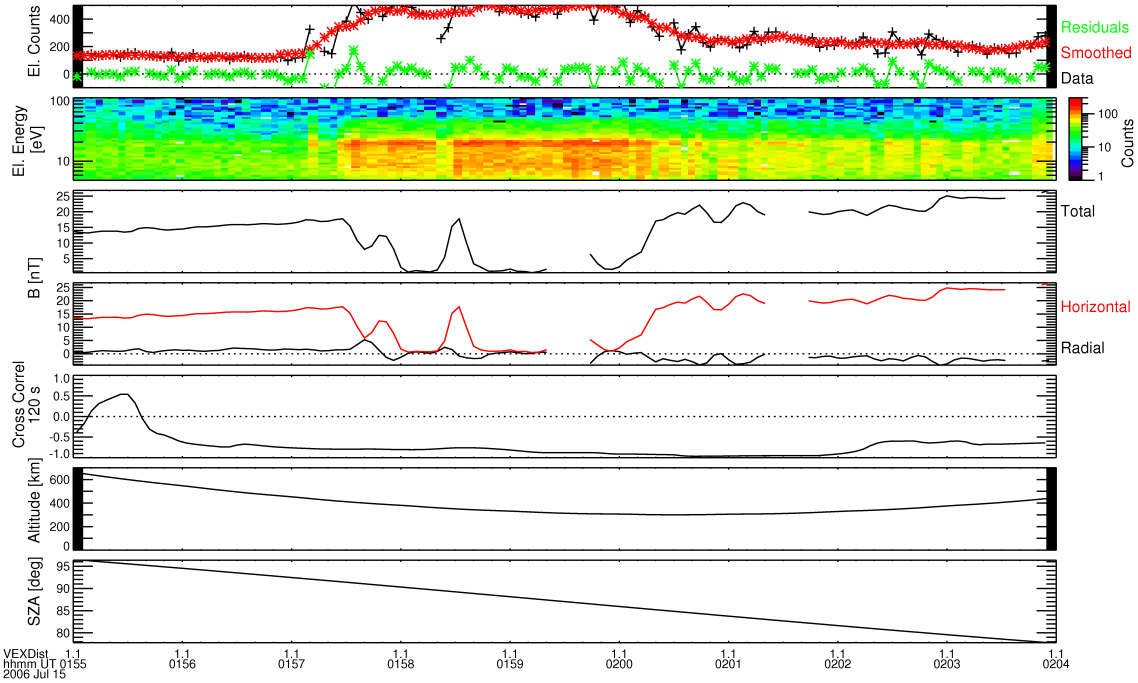

Figure 2.45: A typical unmagnetized ionospheric state (time range: nine minutes). Panels are the same as in Figure 2.44.

use the manually sorted orbits, as they seem more reliable at this point. In total, **58%** of the observed ionospheres with clearly classifiable states were found to be magnetized, and consequently, **42%** were unmagnetized. From July 2008 on, after the lowering of the VEX periapsis (see Figure 2.37), the percentage of magnetized states decreases. Since the solar activity was nearly constant over this time range, only beginning to increase again near the end of 2009, its variations cannot be the reason for the differences. The mean external (dynamic plus magnetic) pressure remained near the same value over the whole time range, and the same holds when we regard only the dynamic pressure. The mean range of solar zenith angles covered by VEX did not change either (see Figure 2.16), so it is very likely that the different magnetization that was found is due to the lower periapsis altitude, since magnetic fields do not necessarily penetrate that far into the ionosphere.

2.5.2.2 Transitional cases

In this section, some examples of orbits are shown which could neither be clearly classified as unmagnetized nor as magnetized. All of them have in common that the magnetic field is neither "high" (above 30 nT) nor "low" (below 10 nT). It is still not completely clear what kind of magnetic states they represent; probably they are transitional states from a magnetized to an unmagnetized ionosphere, or they are located at the spatial boundary between regions with strong and weak ionospheric magnetic fields. They could also be unmagnetized flux-rope cases which contain such a large number of flux ropes that they nearly form a continuum and cannot be distinguished as single magnetic tubes.

Some ideas will be presented for each sample plot.
In Figure 2.46, the electron band extends over a large range in altitude and solar zenith angle, whereas the magnetic field amplitude generally lies around 20 nT. This value is located between the typical ranges for magnetized and unmagnetized states. Furthermore, there is a broad peak on the nightside, shortly after the terminator crossing, which is too extended to be a single flux rope. At the time of this measurement, the velocity of VEX was about 9.7 km/s, which means that the magnetic peak structure has a diameter of almost 600 km. It could be a collection of several merged flux ropes, but this seems improbable because it is very smooth; another possibility is however that it was a flux rope swept towards the nightside which stretched towards the tail, almost tangential to the orbit of VEX, so that it was crossed over most of its length, which is much larger than the diameter. The probability for such an encounter has not yet been investigated, but it is possible. Another scenario could be an ionosphere which is magnetized only locally, in this small region on the nightside, and is otherwise in a transitional state with a magnetic field around 20 nT.

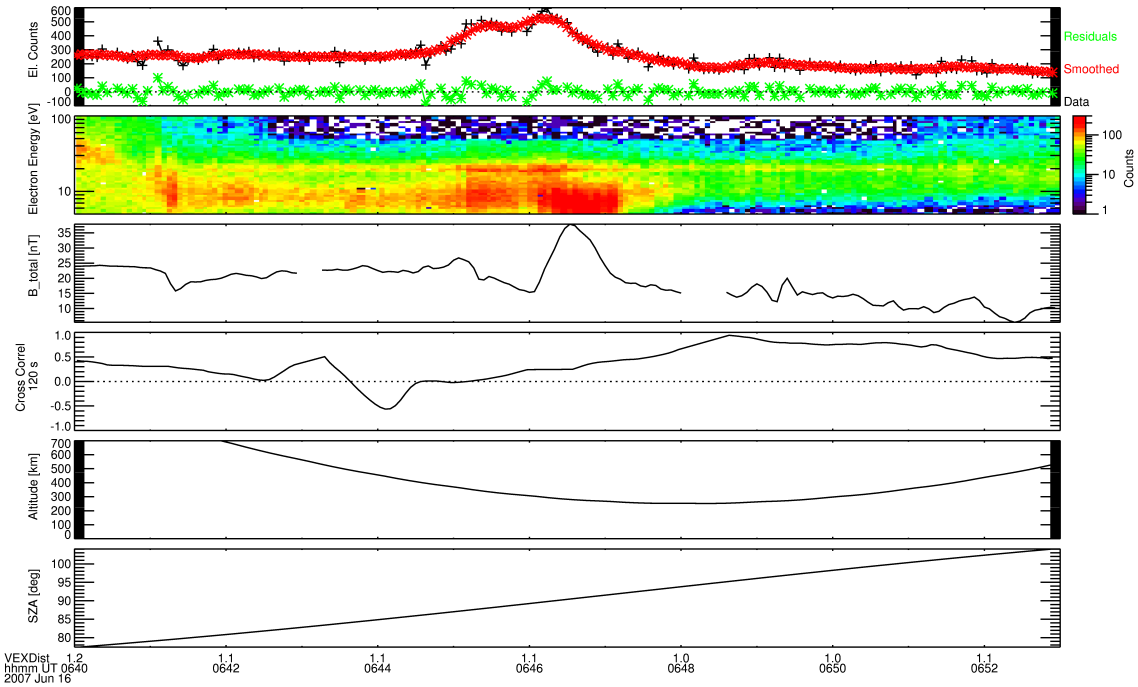

Figure 2.46: Measurements recorded on June 16th, 2007.

Figure 2.47 presents a similar case, but with a more varying magnetic field. The ionosphere is clearly defined on the dayside and gradually weakens on the nightside. In the dayside ionosphere, the field reaches about 30 nT between 04:37 and 04:38, but afterwards it rapidly drops to only a few nT, which would correspond to an unmagnetized case. Therefore it appears as if one is looking at an example of a crossing of an ionosphere which is magnetized in one region and unmagnetized in the other. Further into the nightside, after about 04:39, the magnetic field increases again to values around 20 nT. But in this region, the photoelectron count rate is already very low, so that the nightside

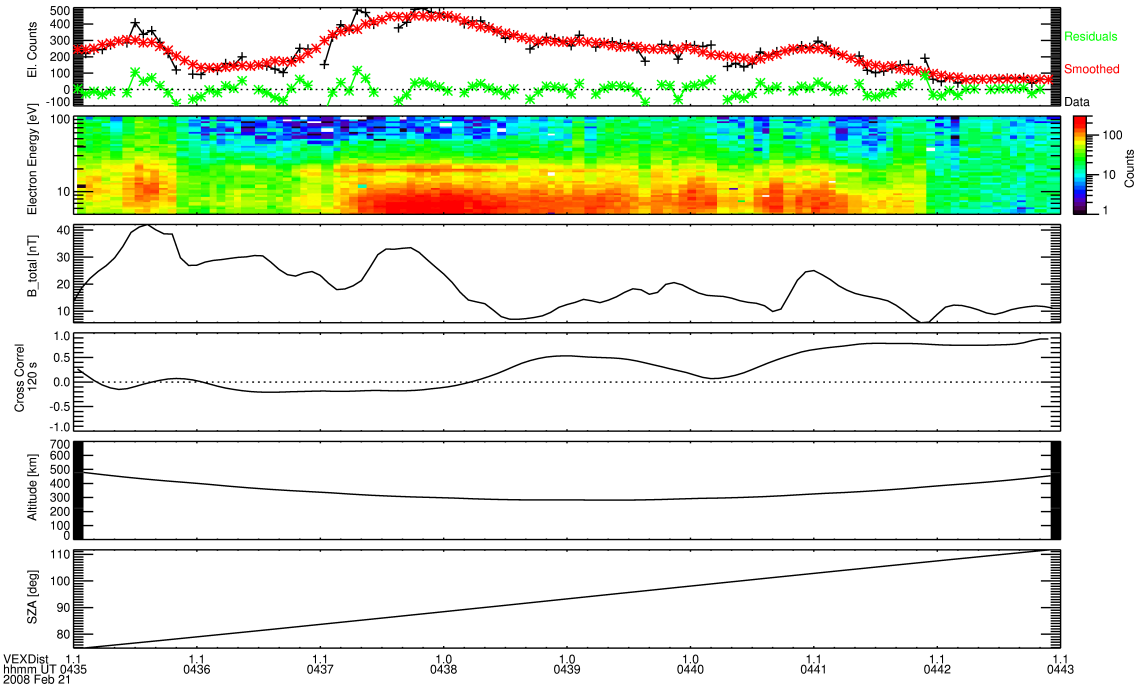

Figure 2.47: Measurements recorded on February 21st, 2008.

ionospheric crossing is probably located around 04:39:30, and the detections after this time represent only some swept-away tail electrons.
In Figure 2.48, the photoelectron band is very clear, and the ionopause locations can be recognized both on the dayside (≈ 04:00) and the nightside (≈ 04:05). Further into the nightside, there is another region in which photoelectrons appear (≈ 04:07:30 - 04:10); since there is a distinct gap between the ionosphere itself and this region, it is probably either a tail ray or even a detached plasma cloud in the tail. In the dayside ionosphere, there is at first a strong magnetic field around 30 nT, which however drops very rapidly to low values towards the terminator, before increasing again on the nightside. The terminator region with its low and fluctuating magnetic field looks like an unmagnetized or very weakly magnetized case; in this part of the ionosphere, the fluctuations are probably due to Kelvin-Helmholtz instabilities and similar processes. The nightside portion of the ionosphere with its magnetic field around 20 nT is once more an in-between case; it might also be possible that different magnetic field thresholds have to be used in determining nightside ionospheric magnetization states. The detached photoelectron cloud in the tail looks clearly unmagnetized; however, this weak field is apparently still strong enough to drag the electrons away. But this is only an assumption, since we were not able to determine the electron velocity distribution within this region.

Figure 2.49 shows a slightly different, interesting example. The ionospheric passage of VEX takes place within a comparatively small altitude range and especially in a very restricted angular range of only one degree, very close to the terminator. Basically, Venus Express just “dips” into the ionosphere with an almost negligible x-velocity component (less than one km/s). The ionospheric structure appears rather filamentary, with many

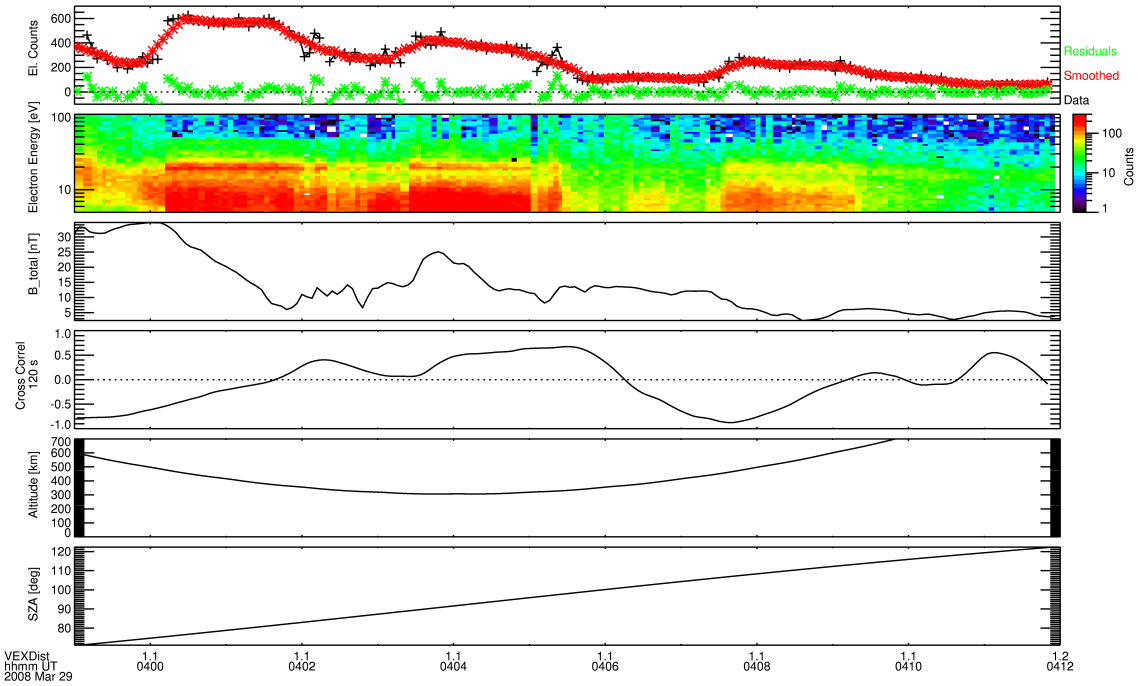

Figure 2.48: Measurements recorded on March 29th, 2008.

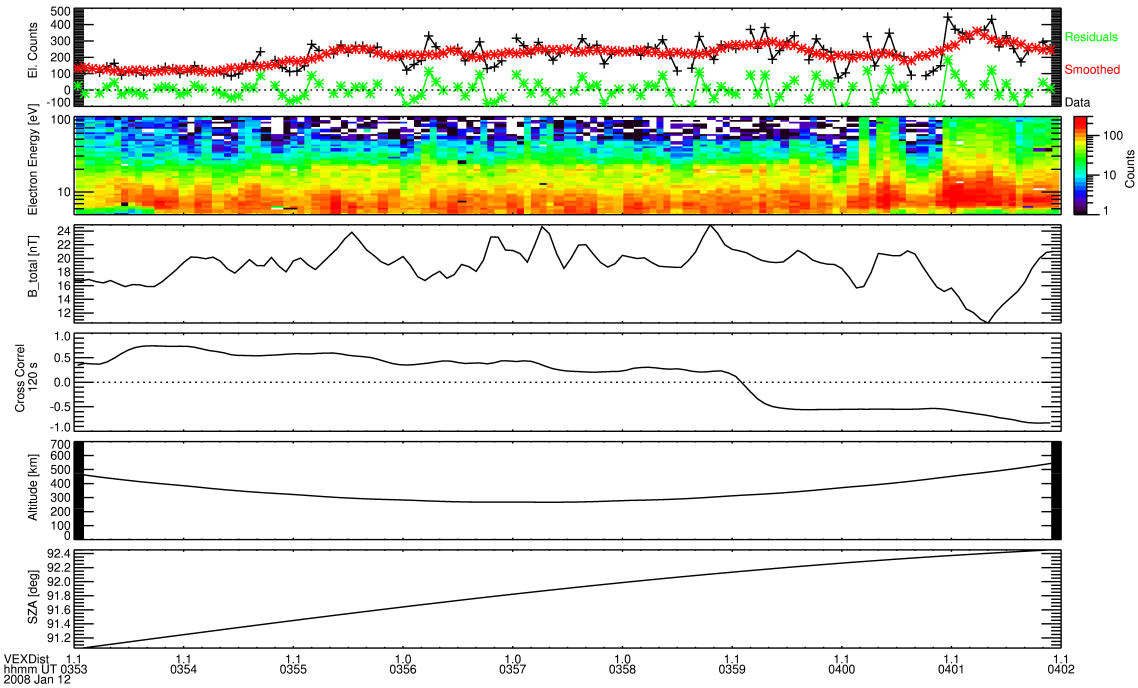

Figure 2.49: Measurements recorded on January 12th, 2008.

gaps in the photoelectron band. The magnetic field behaves in a similar way, exhibiting many fluctuations. One possible interpretation is that Venus Express crosses such a large

number of near-terminator flux ropes that they merge to an average field of about 20 nT, and due to this overlap the ionosphere does not seem clearly unmagnetized. At the same time, it could simply be a transitional state with a weak but large-scale magnetic field, while due to near-terminator turbulences, many small regions are alternatingly present in which either magnetic pressure or plasma pressure dominates, leading to the observed fluctuations in both ELS and MAG measurements.
Another puzzling example is illustrated in Figure 2.50, in which probably many of the factors mentioned before play a role. The ionospheric photoelectron band is weak, but still distinct, and characterized by varying magnetic fields. While in the dayside part, the field is rather weak and decreasing towards larger solar zenith angles, a stronger field appears near the terminator (04:44:30 - 04:45:30). On the nightside, this field briefly decreases to only a few nT, before growing again towards the nightside ionospheric crossing at 04:46:20. Even after this point, the field remains between 10 and 15 nT for a while before it drops to almost zero. In this case, there is no apparent relation to the photoelectron density at all, except possibly for the weak nightside photoion region (04:47 - 04:48), where the onset of photoelectrons coincides with a distinct drop in B.

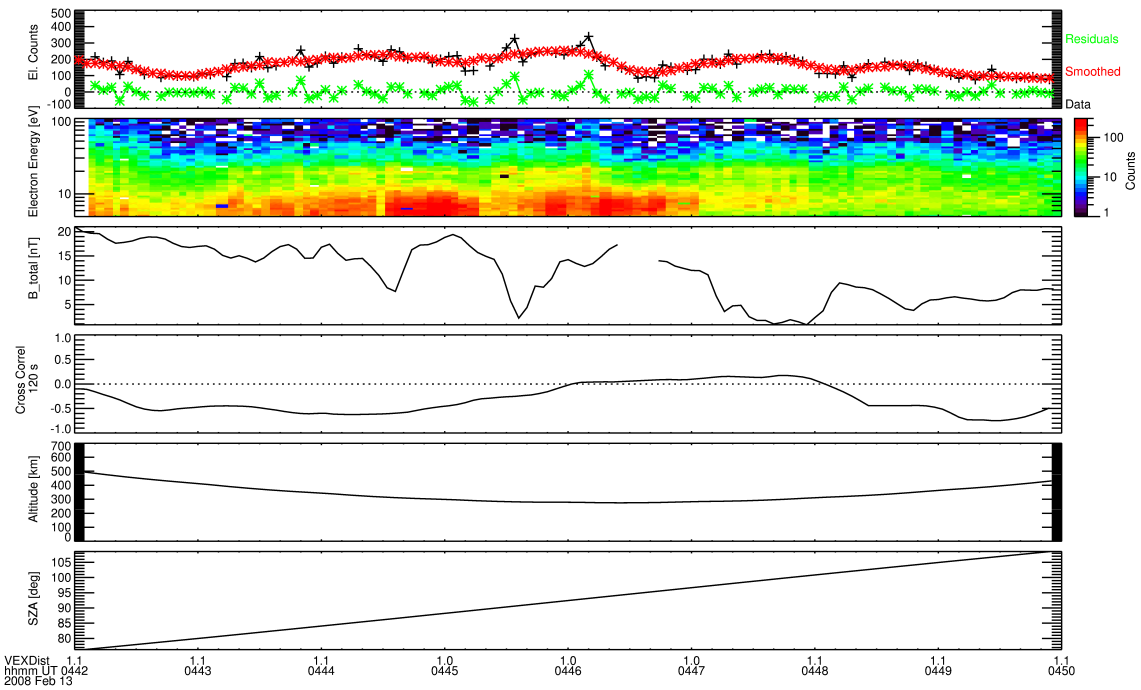

Figure 2.50: Measurements recorded on February 13th, 2008.

In all of these examples, the cross-correlation function varies between positive and negative values and does not give any clear hints as to what kind of magnetic state is present in the ionosphere. Of course, in a crossing of different regions, one of which is magnetized and one unmagnetized, the cross correlation will correspond accordingly. But in our classification, we did not take into account these cases yet, so they will be classified as an unclear or transitional state. Overall, these examples illustrate the variability of the near-terminator ionosphere, which still requires a large amount of investigation.

2.5.3 Mean magnetic field method

To get a more general view on the properties of the ionospheric magnetization states and verify the findings presented in the previous section, we employed yet another approach. Elphic et al. (1984) described a method of classifying these states by simply calculating the average magnetic field strength within a certain altitude range. They used PVO data from the beginning of the mission, where the orbital periapsis was constantly at ~ 150 km altitude for about 450 orbits. This enabled them to compute the average magnetic field within the fixed range from 150 to 200 km for each single orbit. In their definition, the unmagnetized flux rope cases display average field amplitudes up to 25 nT, while the magnetized states lie above 50 nT. Note that Elphic et al. (1984) thus also found many transitional or "in-between" states (located between 25 and 50 nT) and not only clearly classifiable cases. The orbital situation looks quite different for Venus Express, as its periapsis has a strong temporal variability and never reaches the lowest altitudes of PVO (cf. Figure 2.37). Moreover, all VEX PEB observations are conducted at large SZAs, usually above 70° with only very few exceptions. This means that new criteria for the VEX measurements have to be derived.
In order to obtain a sufficient number of data points, we chose to calculate the mean magnetic field between the periapsis and an altitude of 500 km, naming this variable B_{elphic}. (We also conducted the investigations described in this section with a B_{elphic} that was calculated only below 400 and 300 km, respectively, and found no significant difference to the 500 km values. Therefore we decided to use the latter one as it yields more data points.) Taking advantage of our determined plasma boundaries from Section 2.2.3, we also calculated the mean magnetic field between periapsis and ionopause/PEB and named this variable B_{elphic_iono}. Figure 2.51 shows the good agreement between these two mean magnetic field values. This is due to the fact that near the terminator, the ionosphere often extends to altitudes near 500 km and therefore the measurement ranges are very similar for both variables. The data points seem evenly distributed, so one cannot find a clear threshold separating magnetized and unmagnetized states without further investigations.

2.5.3.1 Comparison with manually sorted orbits

In order to determine threshold values of B_{elphic} and B_{elphic_iono} to distinguish between different magnetization states, a comparison of this method with the manual sorting method from Section 2.5.2 makes sense. This will also show whether both approaches are in agreement with each other. In order to combine these methods, we simply assigned values to the manually sorted orbits (0 for unmagnetized and 1 for magnetized cases) and then plotted these as colours in the same representation as in Figure 2.51. The result is given in Figure 2.52.
One can see that the unmagnetized cases do indeed display low mean magnetic field values, while the magnetized orbits are generally located at larger average magnetic fields. Analogously to Elphic et al. (1984), we can now determine thresholds for a classification of magnetization states. This can be done in a more exact way by displaying the distribution of magnetized and unmagnetized cases in bins of mean magnetic field strength, as shown in Figures 2.53 and 2.54. From these figures, we found that the magnetized cases can be characterized by $B_{elphic} > 20$ nT and $B_{elphic_iono} > 22$ nT, whereas the unmagnetized states have values below 15 nT for both variables.

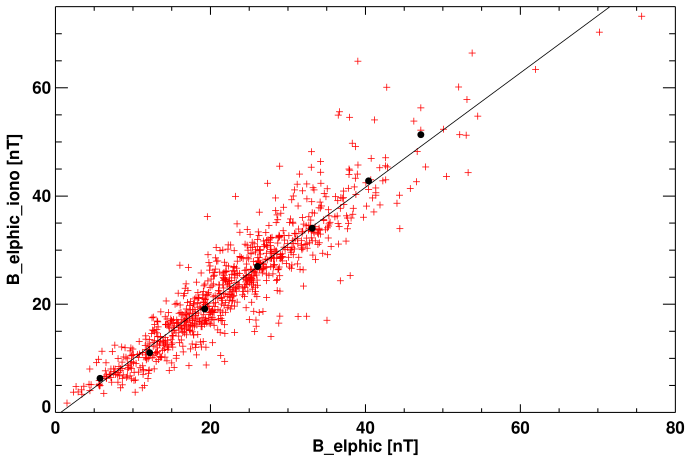

Figure 2.51: B_{elphic}, the average magnetic field below 500 km altitude, plotted versus B_{elphic_iono}, the average magnetic field below the ionopause/PEB (red crosses). Even though they might comprise quite different altitude ranges, the two variables clearly show a linear dependence, which indicates that both of them can be used for further investigations. The black circles are median values, the black line represents a linear fit to the data points.

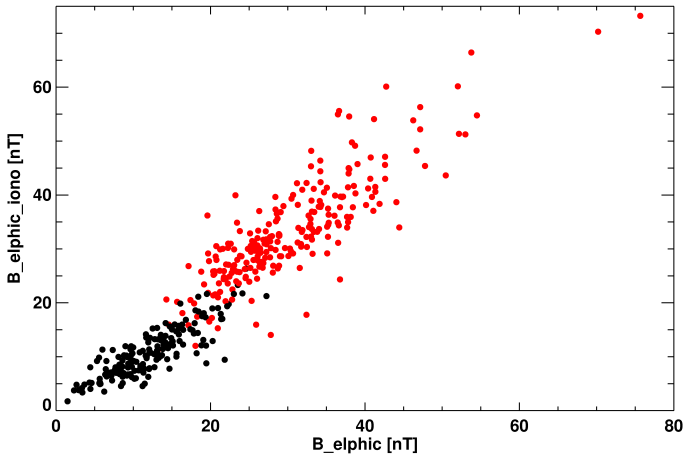

Figure 2.52: The same variables as in Figure 2.51, but with additional colours yielding a comparison between both approaches. Black circles indicate orbits which were classified as unmagnetized in the manual sorting; red circles are the measurements classified as magnetized states.

The advantage of the B_{elphic} method is that it yields quantitative values instead of only a qualitative statement about magnetized and unmagnetized states. These mean magnetic field values allow to investigate more closely the dependence of the degree of ionospheric magnetization on external factors.

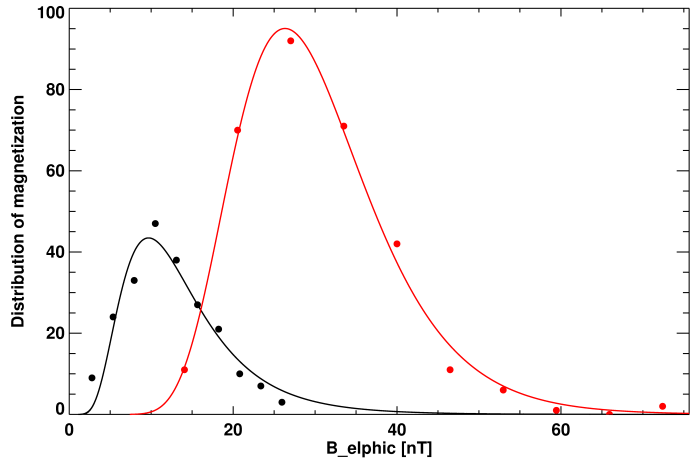

Figure 2.53: Distribution of the numbers of classified measurements for fixed intervals of B_{elphic}. Black circles denote unmagnetized orbits and red circles represent magnetized states. A log-normal function was fitted to each of the two distributions in according colours.

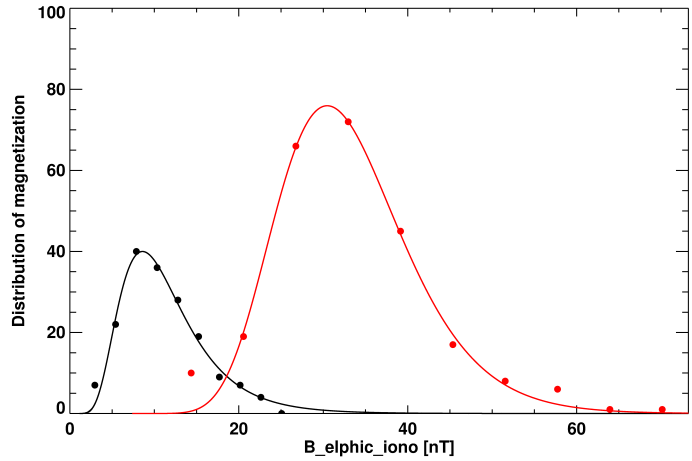

Figure 2.54: The same distributions as in Figure 2.53 for intervals of B_{elphic_iono}, also including log-normal fits.

2.6 Influence of external factors on ionospheric magnetization

With B_{elphic} and B_{elphic_iono}, there is now a powerful tool to directly investigate how the penetration of magnetic fields into the ionosphere depends on the surrounding plasma parameters. In Figures 2.22 and 2.27, the dependence of ionopause altitude and magnetic barrier field on the solar wind pressure were investigated. Now it is also possible to look for relations between the mean ionospheric magnetic field and external contributions. Figure 2.55 shows the variable B_{elphic} versus the magnetic field inside the magnetic barrier for all inbound crossings by Venus Express. The colours indicate the solar zenith

angle at the ionopause location. For dayside measurements, a linear relation between the two variables is recognizable, while the measurements near and behind the terminator (above ≈ 85°) seem to cluster at larger B_{elphic} values and show a steeper slope. This can be seen more easily in Figure 2.56, which illustrates the measurements in both regions separately. While on the dayside, the ionospheric magnetic field, represented by B_{elphic}, increases linearly with growing magnetic barrier pressure, towards and on the nightside the scattering gets larger. This points to more turbulent conditions around the terminator. Another important point is that the slope is generally higher in this part of the plot, and it increases further with larger SZAs. This can be seen again from the colours in Figure 2.55, where data points with an SZA near 90° (blue) tend to lie closer to the dayside values, but green (≈ 100°) and red (≈ 120°) points are located at very low ranges of B_{MB_in}. This can be easily understood from the fact that the magnetic barrier transforms most of the incident solar wind dynamic pressure to magnetic pressure, which is then transferred to the ionopause and might induce magnetic fields there. However, the magnetic barrier becomes much weaker towards the nightside because there is almost no directly impacting solar wind, and the field draping mainly takes place on the dayside. Nevertheless, B_{elphic} reaches similar amplitudes as on the dayside, which is due to the fact that the ionosphere is also much weaker near and behind the terminator, thus allowing for an easier penetration of magnetic fields. Even though the magnetic barrier is only weakly developed , there are several other external pressure contributions, constituted e.g. by the IMF and the Lorentz (J × B) force.

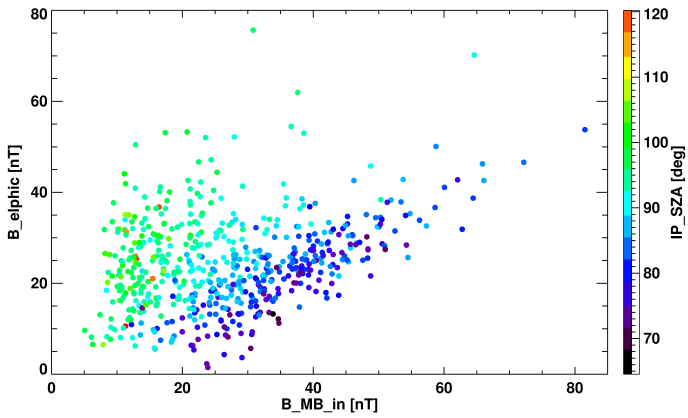

Figure 2.55: The dependence of B_{elphic} on the magnetic pressure inside the magnetic barrier, and on the solar zenith angle. These are only inbound measurements.

For the outbound measurements, the general picture is the same (see Figures 2.57 and 2.58). The SZA dependence is also very well visible when regarding the same figures, but using the solar zenith angle at the magnetopause instead of the ionopause, as shown in Figure 2.59. We can now try to combine the inbound and outbound results, since there should not be any difference between them regarding the general statistics. In order to get good estimates of the mean magnetic field, we decided to use only those orbits in which both the inbound and outbound magnetic barrier locations could be determined, so that a mean value of the field acting on the ionosphere could be calculated. Because B_{elphic} also

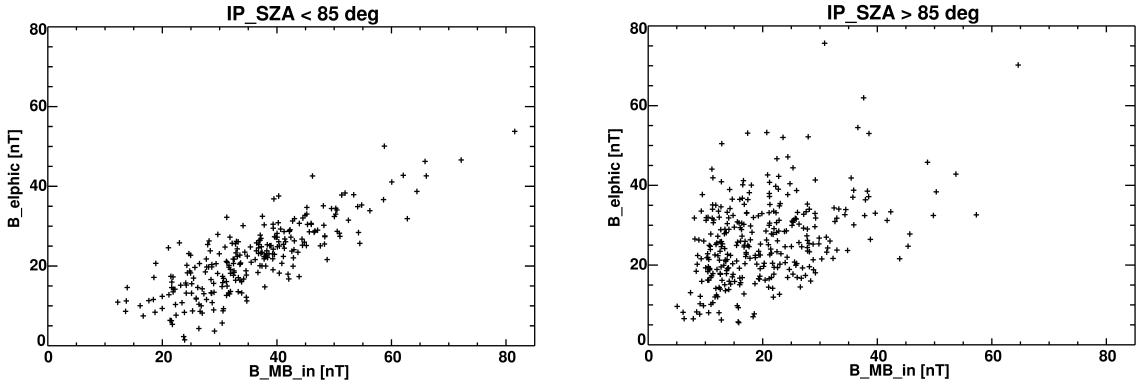

Figure 2.56: The same data as in Figure 2.55, but this time separated into values measured at an ionopause SZA below 85° (left-hand side) and above 85° (right-hand side).

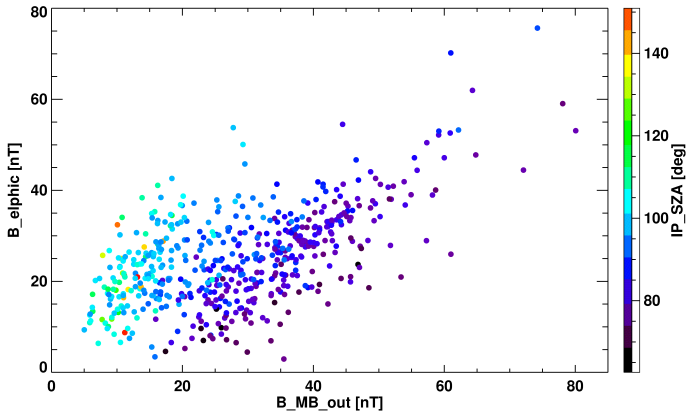

Figure 2.57: The dependence of B_{elphic} on the magnetic pressure inside the magnetic barrier, and on the solar zenith angle. The data given are outbound measurements.

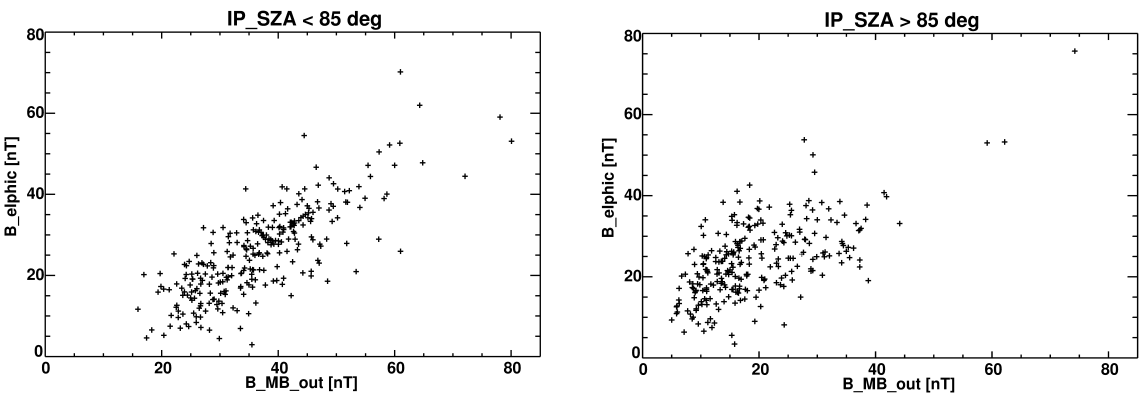

Figure 2.58: The same data as in Figure 2.55, but this time separated into values measured at an ionopause SZA below 85° (left-hand side) and above 85° (right-hand side).

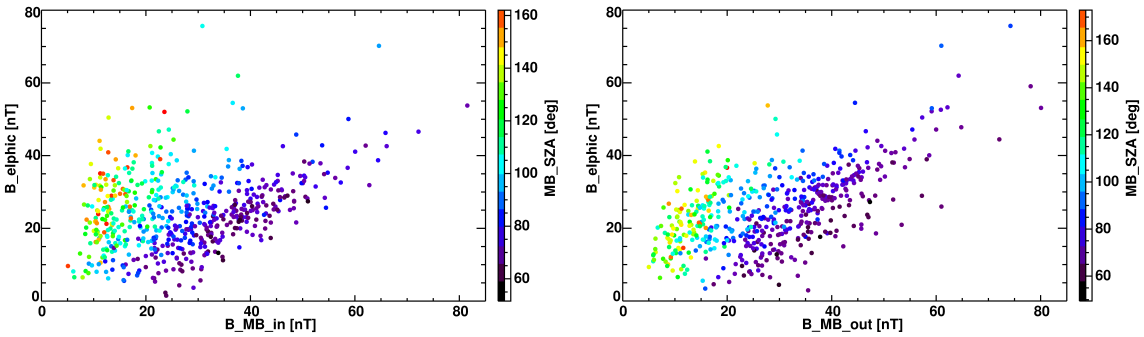

Figure 2.59: Values of B_{elphic} versus inbound and outbound magnetic barrier pressures. The colours stand for the solar zenith angle at each respective crossing of the magnetopause.

delivers only one field value for the whole ionospheric crossing over a certain SZA range, the average field in the magnetic barrier is supposed to better represent the external pressure than single inbound and outbound values. The resulting relation between the external and internal field for the ionopause is presented in Figure 2.60. Their linear dependence is clearly visible, and the scattering is surprisingly low, considering that the original data were those plotted in Figures 2.55 and 2.57, which were much more scattered. But the use of "high-quality" orbits with two clearly defined magnetopause locations as well as the averaging of two values per orbit reveals this intrinsic dependence.
One could of course argue that B_{elphic} is not a very reliable variable because it comprises measurements up to 500 km in altitude and might thus include data from the magnetic barrier region itself. Then a linear dependence would be constructed without any physical meaning. However, if one uses B_{elphic_iono} instead, which only contains measurements below the ionopause as detected by ELS, the relation still holds (see Figure 2.61). This plot thus shows the magnetic field above the ionopause on the x axis, and the resulting magnetic field below the ionopause on the y axis. The magnetization of the ionosphere clearly is strongly correlated with the pressure acting on it via the magnetic barrier.

Since the non-SZA-corrected solar wind dynamic pressure and magnetic barrier internal pressure are correlated (see Figure 2.27), and the ionospheric magnetization in turn depends on the field in the magnetic barrier, one would also expect a linear dependence between total solar wind pressure and ionospheric magnetization, the latter being represented by B_{elphic} (Figure 2.62) and B_{elphic_iono} (Figure 2.63). Again, a linear correlation between the two variables in the left-hand parts of both figures is obvious. For the perpendicular solar wind dynamic pressure component, on the other hand, there is no clear relation with B_{elphic} or B_{elphic_iono} (see the right-hand panels of both figures). This fact further supports the idea explained in Section 2.3 describing a different and more complex pressure balance scenario than near the subsolar point.

It is also worth investigating the orientation of the magnetic field near Venus, and its influence on the magnetization of the ionosphere. The easiest way to define this orientation near the planet is using the clock angle, which is the angle of the projection of a vector

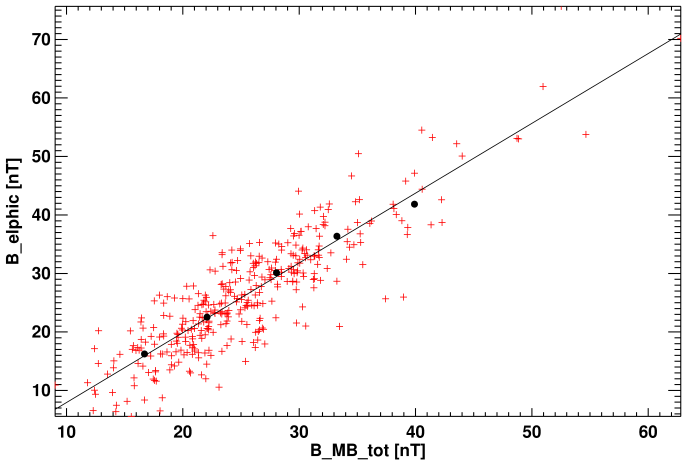

Figure 2.60: The average magnetic field between the VEX periapsis and 500 km altitude (B_{elphic}) versus the mean magnetic field inside the magnetic barrier region. The black circles represent median values and the black line is a linear fit to the (red) data points.

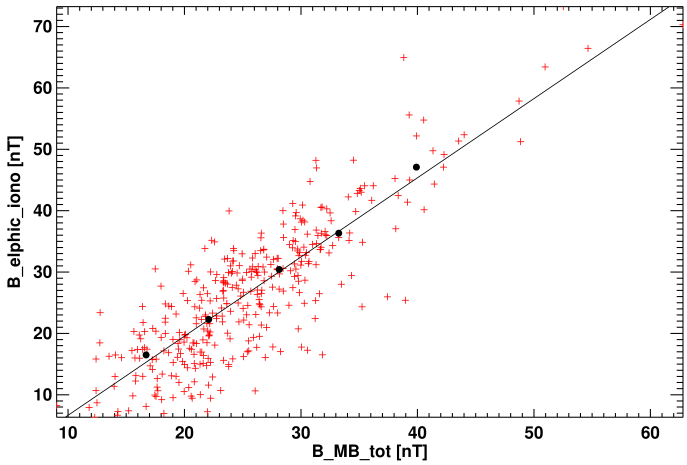

Figure 2.61: The average magnetic field between the VEX periapsis and the ionopause (B_{elphic_iono}) versus the mean magnetic field inside the magnetic barrier region.

onto the terminator plane (the VSO *y*-*z* plane) within this plane. Therefore we produced a plot of B_{elphic} versus the clock angle difference between the VEX position and the magnetic field, both measured at the orbital periapsis. As can be seen in Figure 2.64, there is no detectable dependence of the magnetization on this angular difference. This means that the magnetization does not depend on the degree of draping of magnetic field lines in the respective location of measurement.

A different interesting aspect is the direction of the IMF itself. It is known that the IMF configuration affects the bow shock shape and creates asymmetries (Kallio et al. (2006), Martinecz et al. (2009)). Therefore it might also have an influence on the plasma regions closer to the planet. To investigate this relation, we averaged the amplitude and direction

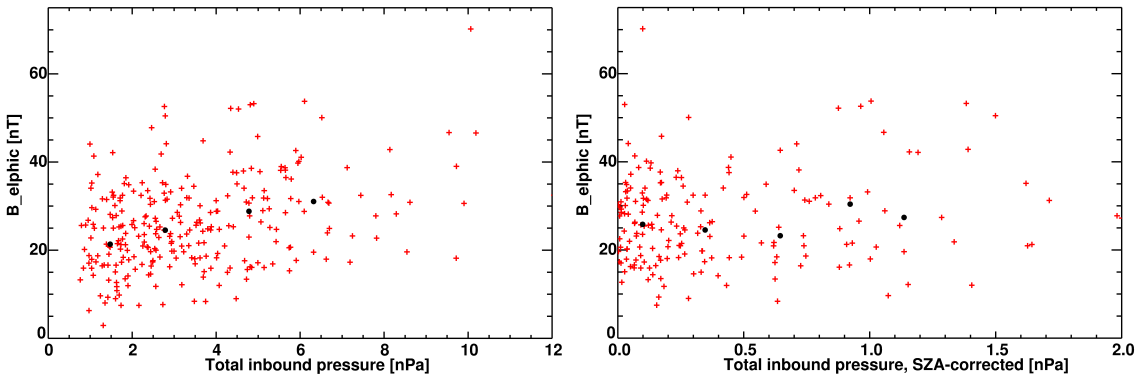

Figure 2.62: The dependence of B_{elphic} on the external pressure (P_{dyn} + P_{mag}) acting on the planet. The red crosses represent the data points, while the black circles are median values. In the left-hand panel, the x axis shows the total pressure measured in the solar wind, while in the right-hand plot, this pressure is corrected by the solar zenith angle.

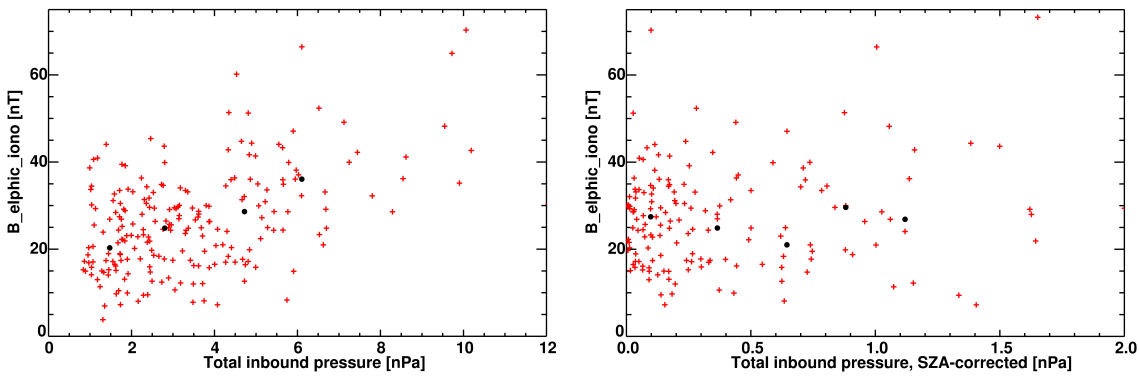

Figure 2.63: The dependence of B_{elphic_iono} on the external pressure acting on the planet. Panels are the same as in Figure 2.62.

of the magnetic field for each orbit over the time range from 2.5 - 1.5 hours before and after the periapsis. After a normalization of B_{elphic} and B_{elphic_iono} to this average IMF amplitude, we displayed the resulting variable against the angle between the VSO x direction and the IMF in Figure 2.65, the so-called IMF cone angle. The data points are scattered over a large range, which is probably due to the different SZA regions which were probed. Nevertheless, the median values of the data clearly show that the ratio of B_{elphic} versus the IMF amplitude decreases with smaller IMF angles. While both B_{elphic} and B_{elphic_iono} are about ten times as large as the IMF for an average angle of about 60°, this ratio decreases as the IMF angle gets smaller. At around 30°, the induced magnetic field is approximately equal to the IMF amplitude, which means that the magnetic compression disappears at this point. A similar result was presented by Zhang et al. (2009) who found that for the rare cases in which the IMF is aligned with the solar wind flow, the induced magnetosphere at Venus disappears. This agrees well with our results.

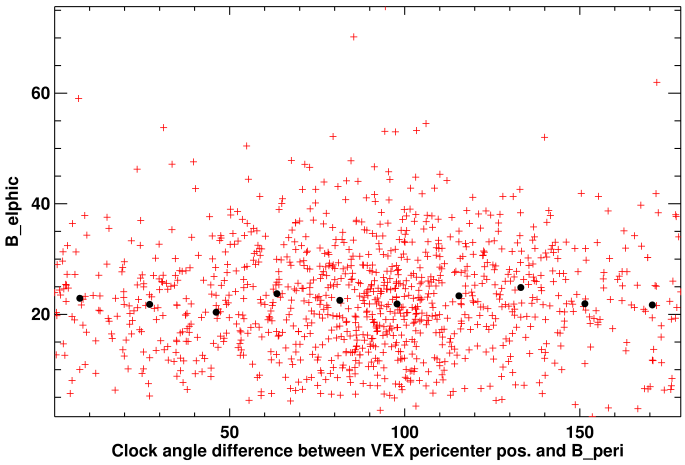

Figure 2.64: B_{elphic} versus the clock angle difference between VEX at periapsis and the magnetic field measured in the same location.

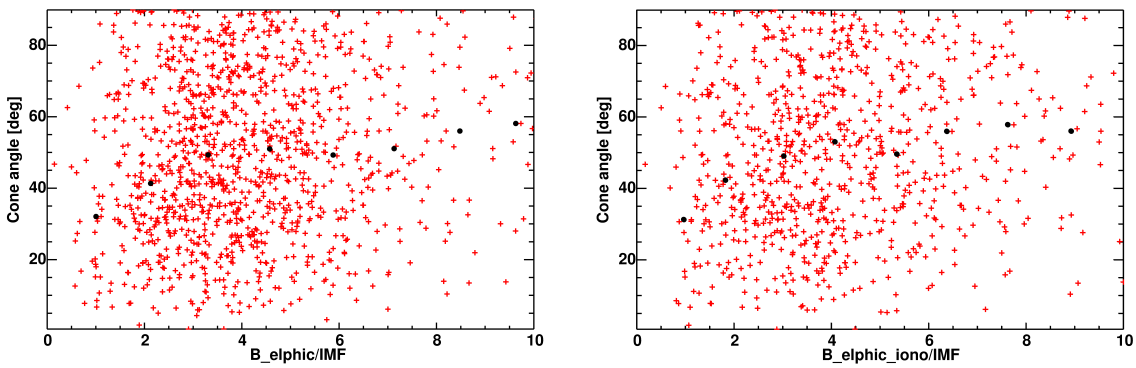

Figure 2.65: The dependence of B_{elphic} (left-hand panel) and B_{elphic_iono} (right-hand side), normalized to the IMF amplitude measured outside the bow shock, on the IMF cone angle. Red crosses represent the data points, black circles are median values.

In Section 2.5.2.1, we mentioned that there is a lower relative amount of magnetized cases after the decrease of the periapsis altitude of VEX in 2008. This tendency is confirmed in Figures 2.66 and 2.67, which show that the average magnetic field below 500 km, as well as the mean field below the ionopause, decreases when the averaging range extends to lower altitudes. This means that at least in some cases, the magnetic field does not penetrate the lower ionosphere. This idea, which was already discussed in Section 2.5.1, is thus further corroborated. Figures 2.68 and 2.69 additionally show the values of B_{elphic} and B_{elphic_iono} over the whole time range from May 2006 to end-2009, where the decrease is clearly visible. Thus it can also be excluded that a mere misinterpretation of the plots which were described in 2.5.2 led to this conclusion.
According to the pressure-balance scenario explained by Luhmann and Cravens (1991), the magnetization is generally more prevailing towards the subsolar point. Thus B_{elphic} should decrease towards larger solar zenith angles, which is indeed confirmed in Figure 2.70. It is clearly visible that there is a strong correlation between both variables up

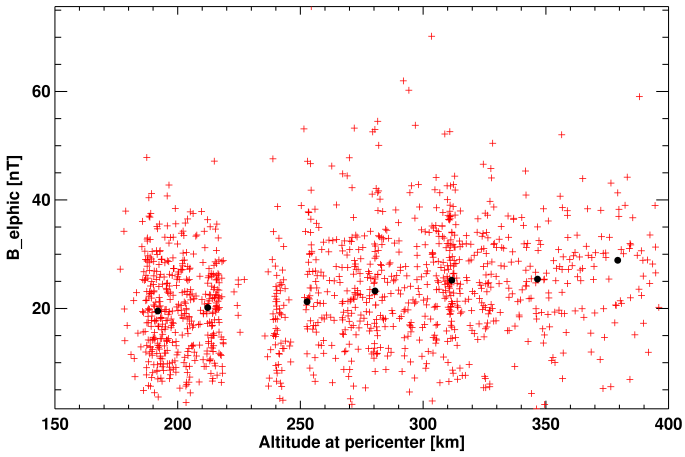

Figure 2.66: The dependence of B_{elphic} on the corresponding periapsis altitude of VEX for each orbit (red crosses) and median values of the data (black circles).

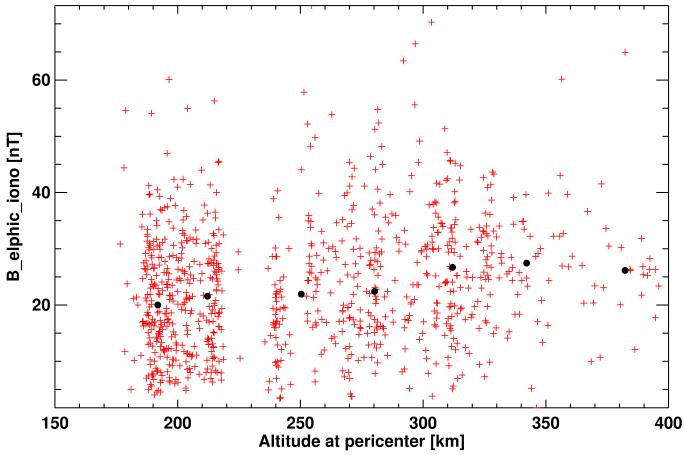

Figure 2.67: The dependence of B_{elphic_iono} on the corresponding periapsis altitude of VEX for each orbit.

to 90°, but then the slope approaches zero and there is hardly any difference in magnetization for increasing SZA.
Furthermore, if the magnetic field can only enter the ionosphere when the external pressure overcomes the ionospheric pressure, the ionopause altitude should exhibit a relation to B_{elphic}. This is shown in Figure 2.71, where the median ionopause altitude is indeed higher for low average magnetic field values. However, this relation soon levels off as higher fields prevail and the ionopause reaches an altitude of 300 km, which is close to its minimum altitude (cf. Figure 1.23).

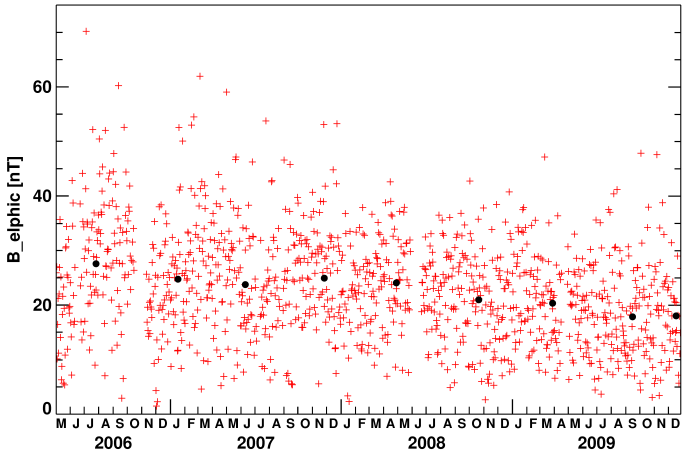

Figure 2.68: Values of B_{elphic} over the full time range in which MAG data were available.

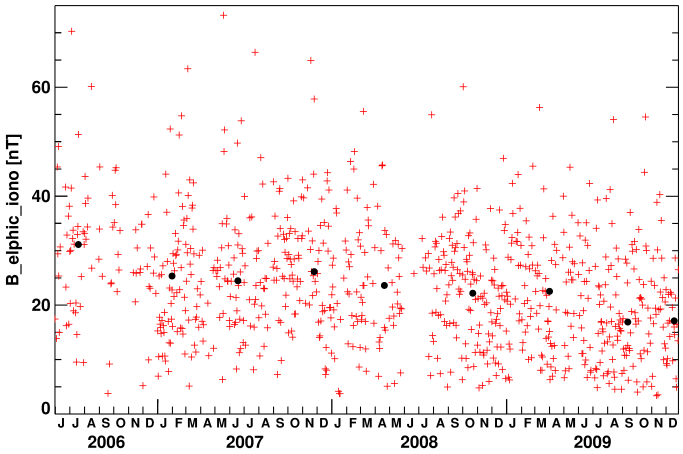

Figure 2.69: Values of B_{elphic_iono} over the full time range in which MAG data were available.

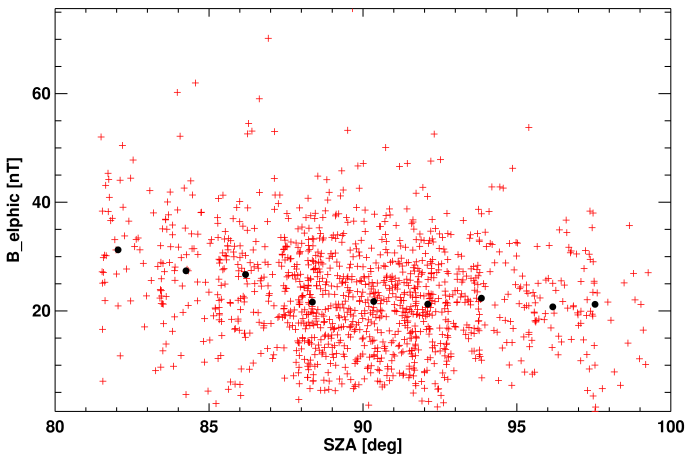

Figure 2.70: B_{elphic} versus the solar zenith angle at the orbital periapsis of VEX. Red crosses are data points, black circles represent medians.

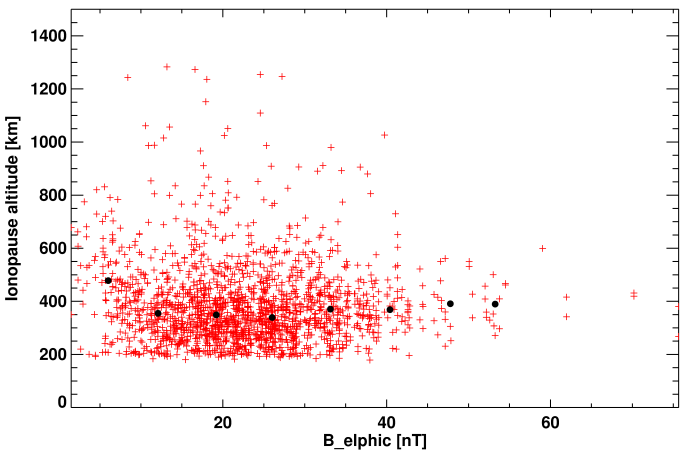

Figure 2.71: The dependence of B_{elphic} on the ionopause altitude.

3 Comparison with previous results

In this chapter, the results obtained in Chapter 2 will be recapitulated and compared to previous results of other researchers. This will fit the focus of this work into a larger context. However, several of these analyses have not been conducted before or only under different conditions, therefore a direct comparison with previous results is not possible in these cases. Instead, we try to determine whether the differences e.g. at different solar activities appear as we expected, and provide explanations as to the nature of these discrepancies.

3.1 Plasma boundaries

In Section 2.2.3, we showed the locations of the bow shock, magnetopause and ionopause which we derived from ELS and MAG data. These have already been investigated by various researchers, especially based on PVO data, but there are some other surveys already using VEX data as well. Therefore it is very interesting to compare our results to those obtained by other methods or based on other data sets.

3.1.1 Bow shock

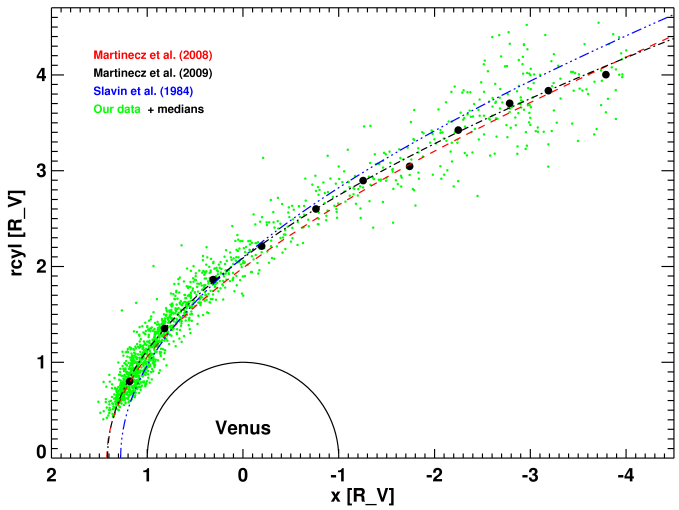

Figure 3.1: Our VEX bow shock locations (green) with median values (black circles) and three fits from Slavin et al. (1984), Martinecz et al. (2008) and Martinecz et al. (2009). Aberration was taken into account for all cases presented in this figure.

Figure 3.1 shows our bow shock crossings and the corresponding median values together with different bow shock fits. The blue curve was taken from Slavin et al. (1984) and represents a fit to the bow shock locations derived from PVO data for solar minimum conditions. The function which was used is a conic section (in this case a hyperbola) whose focus is not located in the centre of Venus, but shifted along the VSO x axis. The red and black curves were taken from Martinecz et al. (2008) and Martinecz et al. (2009). They were fitted to the data using the same kind of function as for the blue curve, but this time, VEX data were used. All three curves lie very close to each other, which demonstrates that the bow shock has a rather constant shape and distance from Venus under similar solar conditions. Moreover, our data set, which comprises a large number of additional points compared to Martinecz et al. (2009), still fits these curves very well.
There are other literature examples of bow shock fits, e.g. Russell et al. (1988), but these are ellipses with the centre of Venus in one of the foci. They fit the current data set less well than the hyperbolae, therefore they were omitted in this study. Figure 2 of Martinecz et al. (2008) shows these two different types of fits in comparison.

3.1.2 Magnetopause

The magnetopause locations which were derived from PVO OMAG (magnetometer) data by Zhang et al. (1991) are displayed in Figure 3.2. They defined this boundary as the location where the local magnetic pressure was equal to half of the perpendicular component of the solar wind dynamic pressure. Due to the temporal evolution of the orbit of PVO, these close-by in-situ measurements were only recorded near solar maximum. Figure 3.3 shows our VEX magnetopause locations in a plot with the same axes, and Figure 3.4 is a combination of both plots, distorted accordingly to allow an exact overlap. It is apparent that the PVO median values form an upper boundary or envelope for the VEX data, generally following the highest VEX magnetopause altitudes. This can be understood by considering that the in-situ PVO measurements were conducted near solar activity maximum, as opposed to the present VEX observations. Therefore the typical PVO magnetopause altitudes are only rarely reached under solar minimum conditions, and form a kind of upper boundary for all VEX measurements.
Zhang et al. (2008a) also presented an initial investigation of the magnetic barrier configuration at Venus using VEX data from the very first few months of the mission. Their magnetopause crossings are shown in Figure 3.5, and agree well with our findings (cf. Figure 2.12).

3.1.2.1 Magnetospheric flaring angle

Using the magnetopause crossings, one can also infer the so-called magnetospheric flaring angle. This is the angle between the solar wind flow direction (thus the aberration has to be taken into account) and the magnetotail surface (Zhang et al. (1994)), where the magnetotail is basically the continuation of the magnetosphere towards the wake, as described in Section 1.2.4.2. We have calculated this angle for our data, using only the measurements on the nightside, as shown in Figure 3.6. The black dots represent the magnetopause crossings at SZA $\geq 90°$. A simple linear fit was applied to these data, resulting in a slope of 0.08, represented by the red line. The standard deviation (1σ) of the slope of

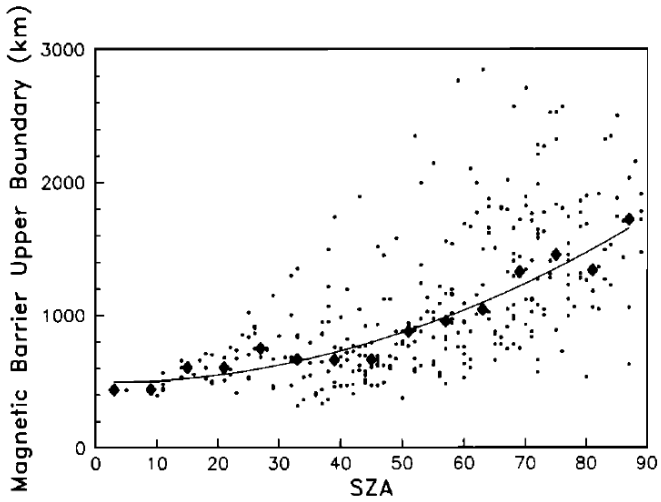

Figure 3.2: Magnetopause altitudes for different SZAs, inferred from PVO data by Zhang et al. (1991). The black dots are the data points, the diamonds correspond to median values and the black curve is a fit to these medians.

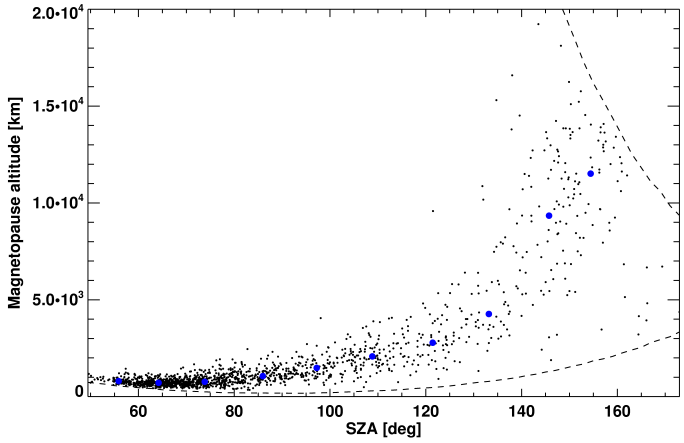

Figure 3.3: The aberration-corrected magnetopause altitudes determined from VEX ELS and MAG data, versus solar zenith angle. Black dots are the data points and the blue circles correspond to median values. The dashed line represents the boundary of the spatial coverage of the VEX in-situ instruments.

the linear fit is indicated by the two dashed red lines. This resulting slope corresponds to a flaring angle of $\alpha = (4.6 \pm 0.7)^\circ$. This is only an average value from all measurements; in reality, the flaring angle depends on the solar wind dynamic pressure (Zhang et al. (1994)) and is thus fluctuating around this mean value. Figure 3.7 shows a plot of flaring angles which we determined from VEX magnetopause crossings for each single orbit versus external pressure (P_{dyn}+P_{mag}). Firstly, one notices that the pressure range under which these measurements were recorded is smaller than in Zhang et al. (1994), who observed pressures from about 0.1 to 10 nPa at Mars. In their plot, the gradient in flaring angle levels off above about 1 nPa. If this is the same at Venus, it is very difficult to detect this

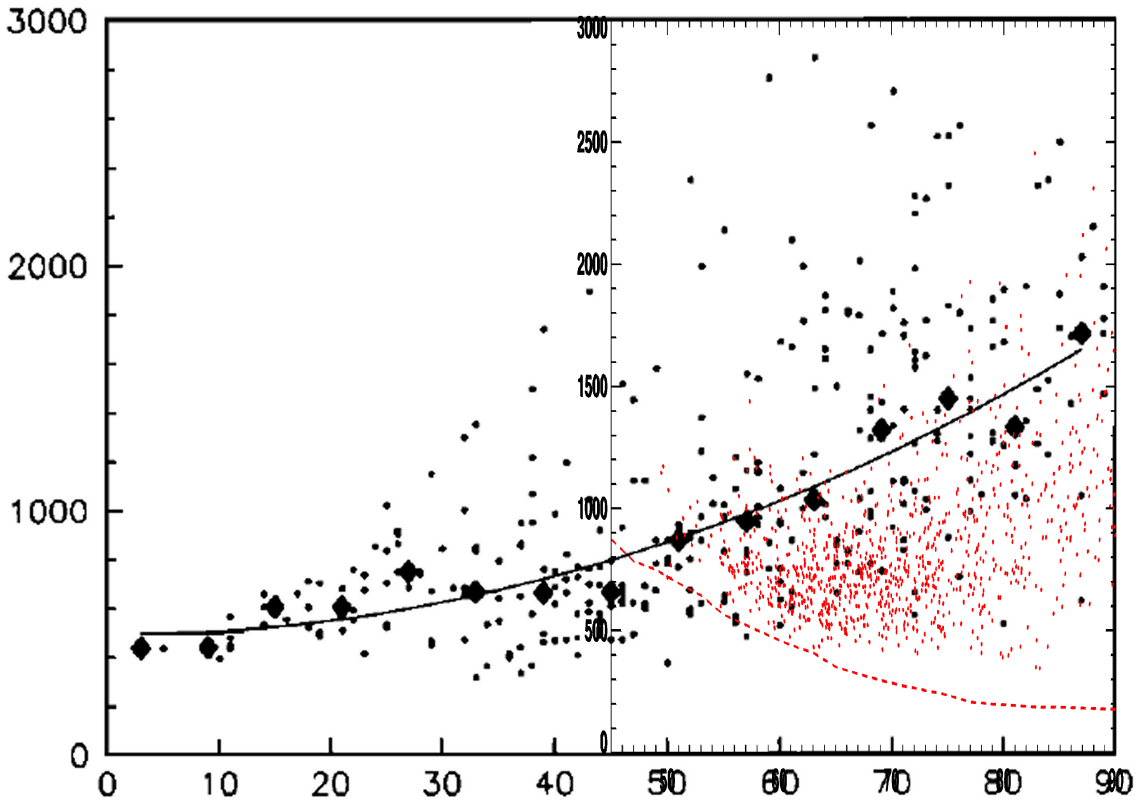

Figure 3.4: A combination of Figures 3.2 (black) and 3.3 (red), using only the data up to 90° in the latter plot. The x axis represents the solar zenith angle of each measurement and the y axis stands for the altitude in km.

dependence because we never measured dynamic pressures at values significantly below 1 nPa. Therefore there is no clear trend in our figure, but the median values remain near 0° for the whole pressure range.

Martinecz et al. (2009) conducted a similar investigation of the average magnetospheric flaring angle as in our Figure 3.6, naming the magnetopause the ion composition boundary (ICB). They found a slope of 0.101 for their linear fit, resulting in a flaring angle of 5.8°. This slight difference to our study may be due to the fact that they used data from May 2006 to December 2007 only. We now have data over a much larger time range, increasing the number of data points. The solar conditions may as well have changed enough to decrease the average flaring angle. Moreover, Martinecz et al. (2009) derived their ICB positions from ELS and IMA data, whereas we used ELS and MAG measurements.

3.1.3 Ionopause

Phillips et al. (1988) compiled a plot containing ionopause altitudes that were determined by different instruments on the Pioneer Venus Orbiter. This is shown in Figure 3.8. A comparison with VEX data is only possible within a solar zenith angle range between 60 and 120°, due to the different spatial coverage of both spacecraft. The data points from

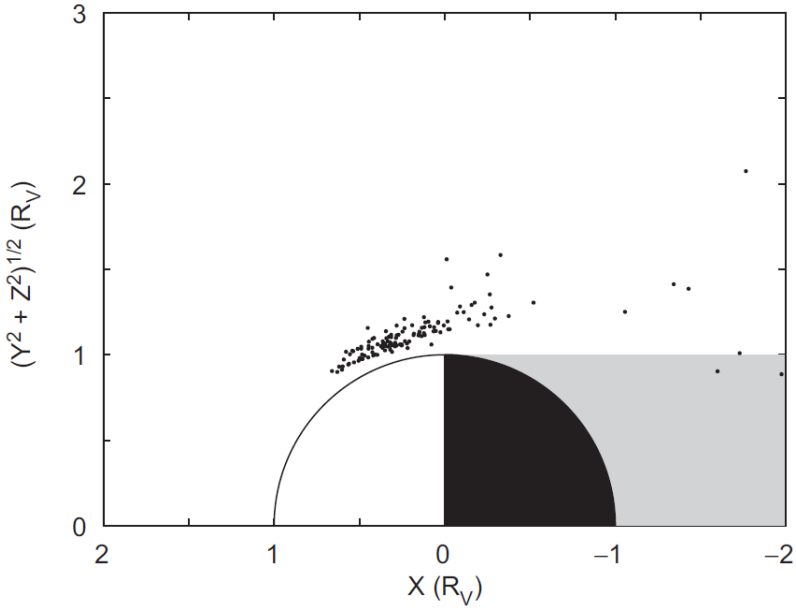

Figure 3.5: Magnetopause crossings from VEX MAG data for the time from May to August 2006 (Zhang et al. (2008a)).

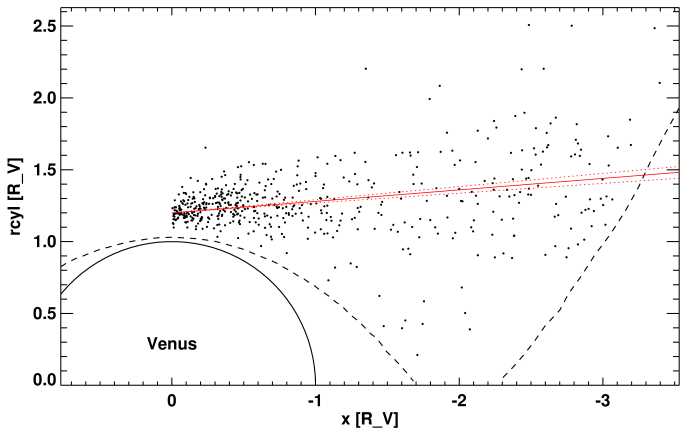

Figure 3.6: Tail magnetopause crossings (black) and a linear fit (solid red line) which yields the average magnetospheric flaring angle for Venus. Dashed lines indicate the standard deviation.

Figure 2.39, which represent the ionopause altitude in dependence of the solar zenith angle, can now be overlaid on the PVO figure. The result can be seen in Figure 3.9. Again, the PVO mean values appear like an upper boundary of the bulk VEX data, a feature which is presumably due to the different solar activity conditions.

Figure 3.10 shows directly and indirectly determined average ionopause and magnetopause locations for solar maximum and solar minimum conditions. Generally, our boundaries fit these curves quite well, but a direct comparison is difficult because the figure only extends to a solar zenith angle of 90°. Thus the main focus is on the dayside, where the

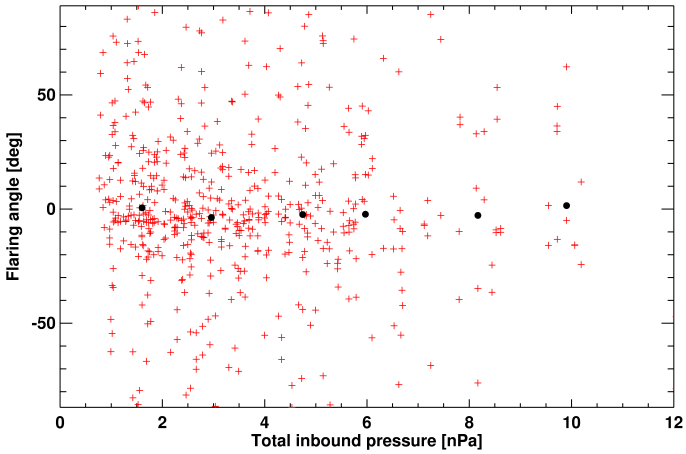

Figure 3.7: Distribution of flaring angles for each single orbit versus incident pressure (P_{dyn}+P_{mag}). Red crosses denote data points and the black circles are median values.

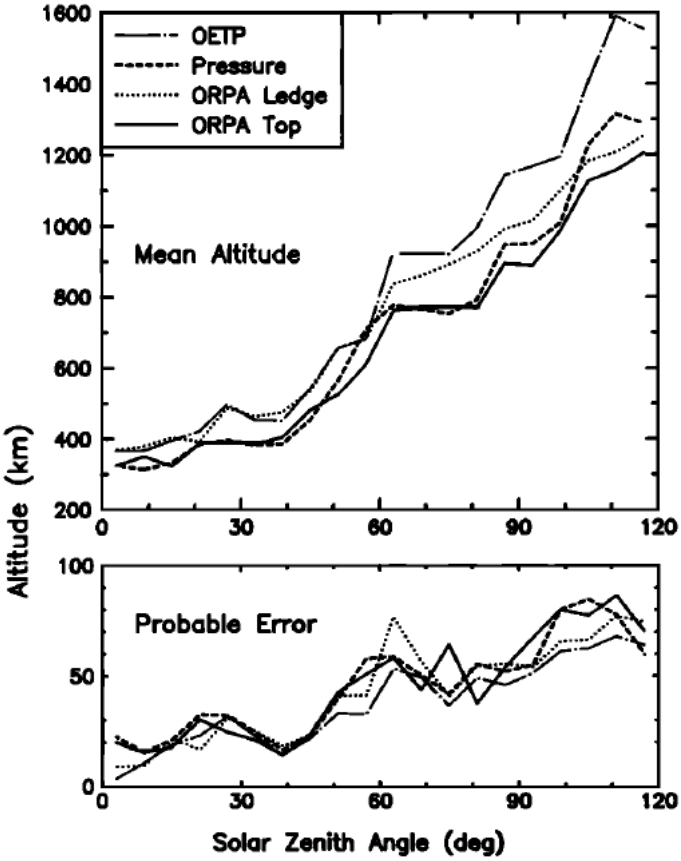

Figure 3.8: Ionopause altitudes in SZA bins of 6°, derived from PVO measurements (Phillips et al. (1988)). OETP was the PVO electron spectrometer, while ORPA analyzed ions as well as photoelectrons (see Section 1.1.3.1). “Pressure” stands for the pressure balance layer, in which the ionospheric thermal pressure equals the external magnetic pressure.

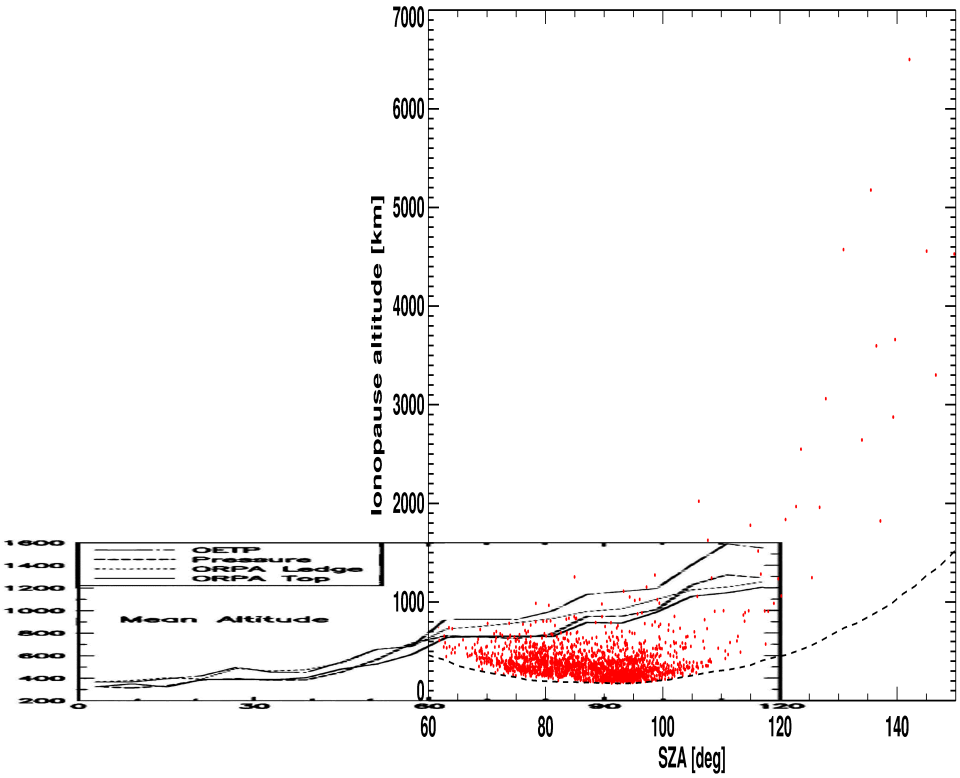

Figure 3.9: A combination of Figures 3.8 and 2.39.

in-situ coverage of VEX is limited. It is possible that the ionopause altitude on the dayside is indeed constant at solar minimum, but especially these data (below 90° SZA) are biased by the sampling. On the nightside, however, there is a very distinct rise in ionopause altitude with increasing solar zenith angle (see Figure 3.9), which is clearly not due to the sampling bias because there are no data points located near the nightside sampling boundary.

3.2 Ionospheric magnetization

Zhang et al. (2008a) investigated the magnetic barrier at Venus using VEX MAG data from 2006. Besides this region, they also briefly consider the ionosphere and its magnetic properties. They say that the ionopause was found to be located at about 250 km altitude throughout the entire dayside by PVO radio occultation measurements during solar minimum. Based on these results, they evaluate the MAG measurements and come to the conclusion that the dayside ionosphere is magnetized in 95% of the cases under solar minimum conditions. This is a significantly larger amount than the 58% which we found. But one has to take into account that these authors only investigated orbits for the time range from April to August 2006, while our data set comprises measurements from June 2006 to December 2009. Furthermore Zhang et al. (2008a) do not include ELS data in their study but rely entirely on the MAG measurements. Luhmann (1986) explains that the percentage of magnetized cases is low during solar maximum because of the higher

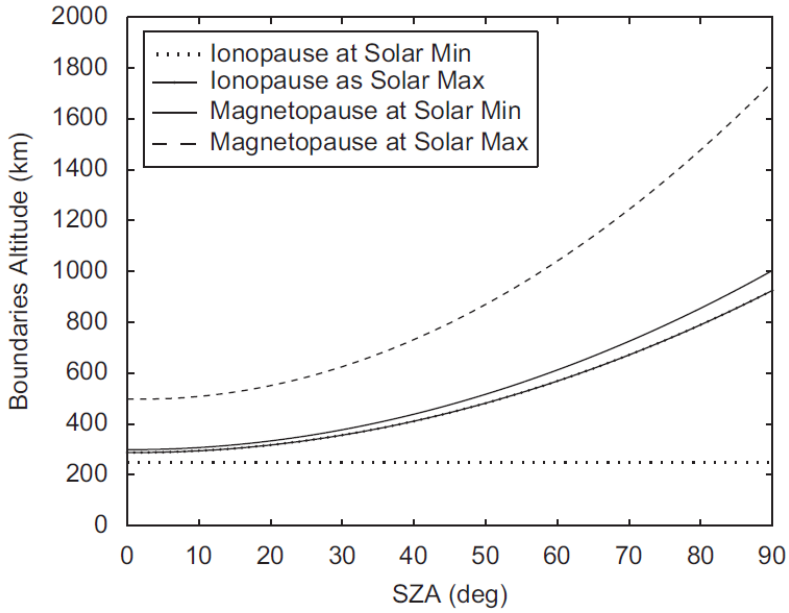

Figure 3.10: Plasma boundary locations for solar minimum and solar maximum (Zhang et al. (2008a)). The solar minimum ionopause function is an assumption, while the other three lines are based on observations. It is visible that the solar minimum magnetopause (plain black line) is located nearly as low as the solar maximum ionopause (black line with dots).

solar EUV radiation flux (more ionization) compared to solar minimum and the increase in exospheric scale height (more atoms and molecules are present to be ionized). Accordingly, the opposite relation holds for solar minimum conditions. The two mentioned effects lead to a lower thermal pressure of the ionosphere and therefore to a higher probability of magnetic field entering this region. However, Luhmann and Cravens (1991) describe that the relative amount of magnetized states becomes smaller with increasing solar zenith angle, as the local radial component of the solar wind dynamic pressure decreases towards higher solar zenith angles. Therefore a lower percentage of magnetized states can be expected near the terminator where VEX is conducting its in-situ measurements, which qualitatively agrees with our observations.
There seem to be no other statistics of magnetized and unmagnetized ionospheric states present in the literature. In particular, solar minimum conditions have never been studied in situ before, thus this is the only comparison that can be done.

4 Summary and conclusions

Even though the orbit of any spacecraft carrying scientific instruments puts constraints on the regions which can be sampled, the trajectory of VEX allows for many exciting new results regarding the plasma environment of Venus. Using data delivered by the magnetometer and the electron spectrometer on board of Venus Express, we successfully determined a large number of PEB, magnetopause and bow shock locations on the dayside as well as on the nightside for the time range from May 2006 to August 2010. These results complement the boundaries found by PVO which were located at different solar zenith angles, and in this way make the existing picture more complete. A direct comparison of VEX (solar minimum) and PVO (solar maximum) plasma boundaries shows that the solar minimum data points are usually found at distinctly lower altitudes due to the weaker ionospheric pressure compared to the solar wind dynamic pressure. In those cases for which solar minimum measurements were available in the literature, e.g. for the bow shock location, our results agree well with previous reports. In other cases, it is only possible to compare solar maximum literature examples to our solar minimum results. From these comparisons, it is apparent that both the magnetopause and the PEB are significantly depressed under low solar activity conditions, as was predicted by theoretical approaches. Moreover, we found many relations between external influences and the location of these plasma boundaries, partially confirming PVO results, but also contributing new findings. The boundary data were used to calculate the average magnetospheric flaring angle, which was found to be smaller than at Mars and Earth. This was already predicted by Luhmann et al. (1991). There are some small differences to the results of Martinecz et al. (2009), which can probably be explained by the different instruments and the smaller time range of the measurements used by these authors.

The magnetization states of the ionosphere were investigated in great detail, employing different approaches to categorize them. We found that the two main methods used for the classification yield results which agree well with each other. The cross-correlation function is a new way of classifying these states which looks quite promising, even though it still has to be amended. In combination with the mean magnetic field method (the calculation of B_{elphic}), we could successfully determine thresholds separating magnetized and unmagnetized cases, which proves that this approach can be applied even under different solar activity and less constant spacecraft orbital conditions. We determined the typical properties of ionospheric magnetization states and derived thresholds for their classification under present solar activity conditions and for the orbital configuration of Venus Express. For the first time, statistics of the prevalence of different ionospheric magnetization states near the terminator and under solar minimum conditions could be established. The percentage of magnetized orbits is larger than for the PVO investigations, which took place at solar maximum. The difference in solar activity is expected to be the main reason

for this discrepancy. This shows that, as expected from theoretical considerations, the ionosphere is magnetized more often at solar minimum than at solar maximum, and this effect is still visible at high latitudes. Due to the weaker solar radiation at low solar activity, the ionosphere is weakly developed and therefore less able to withstand the magnetic pressure acting on it via the magnetic barrier.

Furthermore, the dependence of ionospheric magnetization on various external plasma parameters and geometrical effects was investigated. The penetration of magnetic fields into the ionosphere is proportional to the field acting on it externally via the magnetic barrier. Interestingly, the solar wind dynamic and magnetic pressure were found to influence ionospheric and magnetic barrier fields only to a certain degree, since after including a corrective term to remove the SZA dependence, no correlation could be detected any more. We interpret this as a prevalence of other pressure contributions, e.g. solar wind/ionosheath thermal pressure and $\vec{J} \times \vec{B}$ forces which play a much larger role near the terminator and on the nightside. The magnetic barrier field still does influence ionospheric magnetization, but apparently this field is mainly created by draping of field lines near the terminator and not by the transformation of external dynamic pressure.

According to our results, the magnetization of the ionosphere does not depend on the difference in clock angle between the VEX periapsis location and the magnetic field, i.e. on the question whether the measurement is taking place near the draping pole. However, it does depend on the direction of the interplanetary magnetic field, a parameter which strongly influences the draping near Venus according to our data as well as according to Zhang et al. (2009).

We were also able to confirm many of the relations predicted by simple pressure balance equations, e.g. the decrease of ionospheric magnetization with growing solar zenith angle, or the increase in magnetization for lower ionopause altitudes.

5 Outlook

We analyzed a large number of ionospheric magnetization states using VEX ELS and MAG data. As the periapsis of VEX will be lowered further, already reaching 165 km in 2010, an analysis within the same altitude range which was used by Elphic et al. (1984) will become possible in the future. However, it is important to keep in mind that the solar zenith angle at periapsis is very different from the typical SZA values during the PVO mission, and will even continue to move further into the nightside. There already seems to be a relation between the amount of magnetized states and the minimum spacecraft sampling altitude. In Section 2.5.2.1, we excluded other geometric influences as well as solar EUV and solar wind pressure variations. Moreover, we found a decrease after July 2008 even in the variables B_{elphic} and B_{elphic_iono}. This fact rules out a mere misinterpretation of the available data.
The investigation of the dependence of the magnetization on the IMF direction can be conducted more thoroughly in the future by looking at fixed SZA ranges or even particular orbits with similar SZA, but different IMF directions. So far, we could only show a general trend without taking the SZA into account. Nevertheless, the connection between IMF direction and magnetic compression seems obvious and also agrees with the results of Zhang et al. (2009).
We are able to confirm many of the PVO findings with the VEX ASPERA-4 and MAG data. Due to the different orbit configuration, we can now investigate the terminator region much more closely than with PVO. In particular, detailed measurements of electrons near the planet are possible, enabling a better determination of PEB altitudes. The combination of ELS and MAG data leads to a clear classification of magnetized and unmagnetized ionospheric states. This manual classification can be automatized in the future, making use of the cross-correlation function which seems to be a good indicator, but still has to be supplemented by some additional criteria. Especially in the unmagnetized cases, statistics of flux rope orientations could be investigated, analogously to Elphic and Russell (1983a).
In order to confirm our ionopause locations and find out more about the behaviour of the various tracers of ionospheric plasma being used, a detailed comparison with VeRa data is planned for the future, as described in Section 2.4. In the meantime, several radio-occultation measurements have been conducted in locations close to the ASPERA in-situ sampling region, which can be used for this investigation. Furthermore, even for measurements taken at different solar zenith angles, a Chapman profile could be fitted to the (up to) two ELS PEB and the VeRa ionopause locations which are available per orbit. This procedure would also show whether the ionopause/PEB crossings determined with these different instruments are in agreement with each other. Furthermore, it would yield the general shape and the altitude function of the ionopause, which can then be set into relation to solar EUV flux intensity and external pressure contributions.

Another interesting future prospect is the comparison of ELS results with an ionospheric model which was developed by Dr. Olivier Witasse (ESTEC, the Netherlands). In this way, we will be able to gain further insights into the general structure of the ionosphere and the factors which influence it, and of course it will also be possible to verify the ionopause locations derived from ELS data. Furthermore, a computing code was developed by Prof. Dr. Uwe Motschmann (Technical University of Braunschweig) which is used for the simulation of plasma processes in the environment of Venus. It was already successfully applied by several researchers, e.g. Martinecz (2008), and is now being refined by Stefan Wiehle (Technical University of Braunschweig). In the future, it will be applied to simulate the creation and decay of magnetic fields in the ionosphere of Venus, and will offer a very good opportunity to understand the underlying processes when comparing the simulation results with VEX data.
Magnetic fields in the ionosphere of Venus are also important in a broader context, e.g. pertaining to the detection of lightning on Venus. Russell et al. (2010) describe that various signs pointing to the presence of lightning have been detected by spacecraft previously. One of these signs are electromagnetic whistler-mode waves produced by lightning, which can be detected by the VEX magnetometer. This kind of signal, however, has to cross the ionosphere in order to be detectable by remote-sensing instruments. This is only possible if the local magnetic field is at least partially orientated radially and not purely horizontal, and moreover if it is weak. Strong magnetic fields prevent the propagation and therefore also the detection of these whistler modes. Thus ionospheric magnetic fields do indeed have a large influence on many processes, not only on the transport of charged particles but also on the propagation of waves and therefore the detectability of other processes taking place on planet Venus.

Bibliography

Adams, W. S. and Dunham, T., Jr., 1932. *Absorption Bands in the Infra-Red Spectrum of Venus*. PASP 44, 243–245

Alexander, C. J., Luhmann, J. G. and Russell, C. T., 1986. *Interplanetary field control of the location of the Venus bow shock - Evidence for comet-like ion pickup*. Geophys. Res. Lett. 13, 917–920

Angsmann, A., Fränz, M., Dubinin, E., Woch, J., Barabash, S., Zhang, T. L. and Motschmann, U., 2011. *Magnetic states of the ionosphere of Venus observed by Venus Express*. Planet. Space Sci. 59, 327–337

Barabash, S., Fedorov, A., Sauvaud, J. J., Lundin, R., Russell, C. T., Futaana, Y., Zhang, T. L., Andersson, H., Brinkfeldt, K., Grigoriev, A., Holmström, M., Yamauchi, M., Asamura, K., Baumjohann, W., Lammer, H., Coates, A. J., Kataria, D. O., Linder, D. R., Curtis, C. C., Hsieh, K. C., Sandel, B. R., Grande, M., Gunell, H., Koskinen, H. E. J., Kallio, E., Riihelä, P., Säles, T., Schmidt, W., Kozyra, J., Krupp, N., Fränz, M., Woch, J., Luhmann, J., McKenna-Lawlor, S., Mazelle, C., Thocaven, J., Orsini, S., Cerulli-Irelli, R., Mura, M., Milillo, M., Maggi, M., Roelof, E., Brandt, P., Szego, K., Winningham, J. D., Frahm, R. A., Scherrer, J., Sharber, J. R., Wurz, P. and Bochsler, P., 2007a. *The loss of ions from Venus through the plasma wake*. Nature 450, 650–653

Barabash, S., Sauvaud, J., Gunell, H., Andersson, H., Grigoriev, A., Brinkfeldt, K., Holmström, M., Lundin, R., Yamauchi, M., Asamura, K., Baumjohann, W., Zhang, T. L., Coates, A. J., Linder, D. R., Kataria, D. O., Curtis, C. C., Hsieh, K. C., Sandel, B. R., Fedorov, A., Mazelle, C., Thocaven, J., Grande, M., Koskinen, H. E. J., Kallio, E., Säles, T., Riihela, P., Kozyra, J., Krupp, N., Woch, J., Luhmann, J., McKenna-Lawlor, S., Orsini, S., Cerulli-Irelli, R., Mura, M., Milillo, M., Maggi, M., Roelof, E., Brandt, P., Russell, C. T., Szego, K., Winningham, J. D., Frahm, R. A., Scherrer, J., Sharber, J. R., Wurz, P. and Bochsler, P., 2007b. *The Analyser of Space Plasmas and Energetic Atoms (ASPERA-4) for the Venus Express mission*. Planet. Space Sci. 55, 1772–1792

Bauer, S. J., Brace, L. H., Hunten, D. M., Intriligator, D. S., Knudsen, W. C., Nagy, A. F., Russell, C. T., Scarf, F. L. and Wolfe, J. H., 1977. *The Venus ionosphere and solar wind interaction*. Space Sci. Rev. 20, 413–430

Baumjohann, W., Blanc, M., Fedorov, A. and Glassmeier, K., 2010. *Current Systems in Planetary Magnetospheres and Ionospheres*. Space Sci. Rev. 152, 99–134

Brace, L. H. and Kliore, A. J., 1991. *The structure of the Venus ionosphere*. Space Science Reviews 55, 81–163

Brace, L. H., Theis, R. F. and Hoegy, W. R., 1982. *Plasma clouds above the ionopause of Venus and their implications*. Planet. Space Sci. 30, 29–37

Brain, D. A., 2004. *The bow shocks and upstream waves of Venus and Mars*. Advances in Space Research 33, 1913–1919

Burlaga, L. F. and Ogilvie, K. W., 1970. *Magnetic and Thermal Pressures in the Solar Wind*. Sol. Phys. 15, 61–71

Burton, M. E., Buratti, B., Matson, D. L. and Lebreton, J., 2001. *The Cassini/Huygens Venus and earth flybys: An overview of operations and results*. J. Geophys. Res. 106, 30099–30108

Carlson, R. W. and Taylor, F. W., 1993. *The Galileo encounter with Venus: results from the near-infrared mapping spectrometer*. Planet. Space Sci. 41, 475–476

Chapman, S., 1931. *The absorption and dissociative or ionizing effect of monochromatic radiation in an atmosphere on a rotating Earth*. Proc. Phys. Soc. 43(5), 26–45

Cloutier, P. A., Tascione, T. F. and Daniell, R. E., 1981. *An electrodynamic model of electric currents and magnetic fields in the dayside ionosphere of Venus*. Planet. Space Sci. 29, 635–652

Coates, A. J., 2004. *Ion pickup at comets*. Advances in Space Research 33, 1977–1988

Coates, A. J., Frahm, R. A., Linder, D. R., Kataria, D. O., Soobiah, Y., Collinson, G., Sharber, J. R., Winningham, J. D., Jeffers, S. J., Barabash, S., Sauvaud, J., Lundin, R., Holmström, M., Futaana, Y., Yamauchi, M., Grigoriev, A., Andersson, H., Gunell, H., Fedorov, A., Thocaven, J., Zhang, T. L., Baumjohann, W., Kallio, E., Koskinen, H., Kozyra, J. U., Liemohn, M. W., Ma, Y., Galli, A., Wurz, P., Bochsler, P., Brain, D., Roelof, E. C., Brandt, P., Krupp, N., Woch, J., Fraenz, M., Dubinin, E., McKenna-Lawlor, S., Orsini, S., Cerulli-Irelli, R., Mura, A., Milillo, A., Maggi, M., Curtis, C. C., Sandel, B. R., Hsieh, K. C., Szego, K., Asamura, A. and Grande, M., 2008. *Ionospheric photoelectrons at Venus: Initial observations by ASPERA-4 ELS*. Planet. Space Sci. 56, 802–806

Colin, L. and Hall, C. F., 1977. *The Pioneer Venus program*. Space Sci. Rev. 20, 283–306

Cravens, T. E. and Gombosi, T. I., 2004. *Cometary magnetospheres: a tutorial*. Advances in Space Research 33, 1968–1976

Cravens, T. E. and Shinagawa, H., 1991. *The ionopause current layer at Venus*. J. Geophys. Res. 96, 11119–11131

Dubinin, E., Modolo, R., Fraenz, M., Woch, J., Duru, F., Akalin, F., Gurnett, D., Lundin, R., Barabash, S., Plaut, J. J. and Picardi, G., 2008. *Structure and dynamics of the solar wind/ionosphere interface on Mars: MEX-ASPERA-3 and MEX-MARSIS observations*. Geophys. Res. Lett. 35, L11103

Duru, F., Gurnett, D. A., Frahm, R. A., Winningham, J. D., Morgan, D. D. and Howes, G. G., 2009. *Steep, transient density gradients in the Martian ionosphere similar to the ionopause at Venus*. Journal of Geophysical Research (Space Physics) 114, A12310

Elphic, R. C., Brace, L. H., Theis, R. F. and Russell, C. T., 1984. *Venus dayside ionospheric conditions - Effects of ionospheric magnetic field and solar EUV flux*. Geophys. Res. Lett. 11, 124–127

Elphic, R. C. and Russell, C. T., 1983a. *Global characteristics of magnetic flux ropes in the Venus ionosphere*. J. Geophys. Res. 88, 2993–3003

Elphic, R. C. and Russell, C. T., 1983b. *Magnetic flux ropes in the Venus ionosphere - Observations and models*. J. Geophys. Res. 88, 58–72

Elphic, R. C., Russell, C. T., Luhmann, J. G., Scarf, F. L. and Brace, L. H., 1981. *The Venus ionopause current sheet - Thickness length scale and controlling factors*. J. Geophys. Res. 86, 11430–11438

Elphic, R. C., Russell, C. T., Slavin, J. A. and Brace, L. H., 1980. *Observations of the dayside ionopause and ionosphere of Venus*. J. Geophys. Res. 85, 7679–7696

Fox, J. L., 2007. *Near-terminator Venus ionosphere: How Chapman-esque?* Journal of Geophysical Research (Planets) 112, E04S02

Fox, J. L., 2008. *Morphology of the dayside ionosphere of Venus: Implications for ion outflows*. Journal of Geophysical Research (Planets) 113, E11001

Fränz, M., Dubinin, E., Nielsen, E., Woch, J., Barabash, S., Lundin, R. and Fedorov, A., 2010. *Transterminator ion flow in the Martian ionosphere*. Planet. Space Sci. 58, 1442–1454

Funsten, H. O. and McComas, D. J., 1998. *Limited Resource Plasma Analyzers: Miniaturization Concepts*. In Pfaff, R. F., Borovsky, J. E. and Young, D. T. (editors), *Measurement Techniques in Space Plasmas - Particles, Geophysical Monograph 102*, pages 157–167. American Geophysical Union

Gan, L., Cravens, T. E. and Horanyi, M., 1990. *Electrons in the ionopause boundary layer of Venus*. J. Geophys. Res. 95, 19023–19035

Gillmann, C., Chassefière, E. and Lognonné, P., 2009. *A consistent picture of early hydrodynamic escape of Venus atmosphere explaining present Ne and Ar isotopic ratios and low oxygen atmospheric content*. Earth and Planetary Science Letters 286, 503–513

Grinspoon, D. H., 1993. *Implications of the high D/H ratio for the sources of water in Venus' atmosphere*. Nature 363, 428–431

Grünwaldt, H., Neugebauer, M., Hilchenbach, M., Bochsler, P., Hovestadt, D., Bürgi, A., Ipavich, F. M., Reiche, K., Axford, W. I., Balsiger, H., Galvin, A. B., Geiss, J., Gliem, F., Gloeckler, G., Hsieh, K. C., Kallenbach, R., Klecker, B., Livi, S., Lee, M. A., Managadze, G. G., Marsch, E., Möbius, E., Scholer, M., Verigin, M. I., Wilken, B.

and Wurz, P., 1997. *Venus tail ray observation near Earth*. Geophys. Res. Lett. 24, 1163–1166

John, C. E. and Nicholson, S. B., 1922. *The Physical Constituents of the Atmosphere of Venus*. Physical Review 19, 444

Kallio, E., Jarvinen, R. and Janhunen, P., 2006. *Venus solar wind interaction: Asymmetries and the escape of O^+ ions*. Planet. Space Sci. 54, 1472–1481

Kallio, E., Zhang, T. L., Barabash, S., Jarvinen, R., Sillanpää, I., Janhunen, P., Fedorov, A., Sauvaud, J., Mazelle, C., Thocaven, J., Gunell, H., Andersson, H., Grigoriev, A., Brinkfeldt, K., Futaana, Y., Holmström, M., Lundin, R., Yamauchi, M., Asamura, K., Baumjohann, W., Lammer, H., Coates, A. J., Linder, D. R., Kataria, D. O., Curtis, C. C., Hsieh, K. C., Sandel, B. R., Grande, M., Koskinen, H. E. J., Säles, T., Schmidt, W., Riihelä, P., Kozyra, J., Krupp, N., Woch, J., Luhmann, J. G., McKenna-Lawlor, S., Orsini, S., Cerulli-Irelli, R., Mura, A., Milillo, A., Maggi, M., Roelof, E., Brandt, P., Russell, C. T., Szego, K., Winningham, J. D., Frahm, R. A., Scherrer, J. R., Sharber, J. R., Wurz, P. and Bochsler, P., 2008. *The Venusian induced magnetosphere: A case study of plasma and magnetic field measurements on the Venus Express mission*. Planet. Space Sci. 56, 796–801

Kar, J., 1996. *Recent Advances in Planetary Ionospheres*. Space Sci. Rev. 77, 193–266

Kar, J. and Mahajan, K. K., 1987a. *On the response of ionospheric magnetisation to solar wind dynamic pressure from Pioneer Venus measurements*. Geophys. Res. Lett. 14, 507–510

Kar, J. and Mahajan, K. K., 1987b. *Reply to Phillips*. Geophys. Res. Lett. 14, 1070–1071

Killen, R. M., Sarantos, M. and Reiff, P. H., 2004. *Space weather at Mercury*. Advances in Space Research 33, 1899–1904

Kivelson, M. G., 2004. *Moon-magnetosphere interactions: a tutorial*. Advances in Space Research 33, 2061–2077

Kliore, A. J. and Mullen, L. F., 1989. *The long-term behavior of the main peak of the dayside ionosphere of Venus during solar cycle 21 and its implications on the effect of the solar cycle upon the electron temperature in the main peak region*. J. Geophys. Res. 94, 13339–13351

Kulikov, Y. N., Lammer, H., Lichtenegger, H. I. M., Penz, T., Breuer, D., Spohn, T., Lundin, R. and Biernat, H. K., 2007. *A Comparative Study of the Influence of the Active Young Sun on the Early Atmospheres of Earth, Venus, and Mars*. Space Sci. Rev. 129, 207–243

Kulikov, Y. N., Lammer, H., Lichtenegger, H. I. M., Terada, N., Ribas, I., Kolb, C., Langmayr, D., Lundin, R., Guinan, E. F., Barabash, S. and Biernat, H. K., 2006. *Atmospheric and water loss from early Venus*. Planet. Space Sci. 54, 1425–1444

Lammer, H., Lichtenegger, H. I. M., Biernat, H. K., Erkaev, N. V., Arshukova, I. L., Kolb, C., Gunell, H., Lukyanov, A., Holmstrom, M., Barabash, S., Zhang, T. L. and Baumjohann, W., 2006. *Loss of hydrogen and oxygen from the upper atmosphere of Venus*. Planet. Space Sci. 54, 1445–1456

Langlais, B., Lesur, V., Purucker, M. E., Connerney, J. E. P. and Mandea, M., 2010. *Crustal Magnetic Fields of Terrestrial Planets*. Space Sci. Rev. 152, 223–249

Law, C. C. and Cloutier, P. A., 1995. *Observations of magnetic structure at the dayside ionopause of Venus*. J. Geophys. Res. 100, 23973–23982

Luhmann, J. G., 1986. *The solar wind interaction with Venus*. Space Science Reviews 44, 241–306

Luhmann, J. G., 1988. *Comment on 'On the response of ionospheric magnetisation to solar wind dynamic pressure from Pioneer Venus measurements'*. Geophys. Res. Lett. 15, 118–119

Luhmann, J. G. and Cravens, T. E., 1991. *Magnetic fields in the ionosphere of Venus*. Space Science Reviews 55, 201–274

Luhmann, J. G., Elphic, R. C., Russell, C. T., Brace, L. H. and Hartle, R. E., 1982. *Effects of large-scale magnetic fields in the Venus ionosphere*. Advances in Space Research 2, 17–21

Luhmann, J. G., Elphic, R. C., Russell, C. T., Mihalov, J. D. and Wolfe, J. H., 1980. *Observations of large scale steady magnetic fields in the dayside Venus ionosphere*. Geophys. Res. Lett. 7, 917–920

Luhmann, J. G., Ledvina, S. A. and Russell, C. T., 2004. *Induced magnetospheres*. Advances in Space Research 33, 1905–1912

Luhmann, J. G., Phillips, J. L. and Russell, C. T., 1987. *Studies of the configuration of the Venus ionospheric magnetic field*. Advances in Space Research 7, 101–106

Luhmann, J. G. and Russell, C. T., 1997. *Venus: Magnetic field and magnetosphere*. In Shirley, J. H. and Fairbridge, R. W. (editors), *Encyclopedia of Planetary Sciences*, pages 905–907. Chapman & Hall

Luhmann, J. G., Russell, C. T. and Elphic, R. C., 1984. *Time scales for the decay of induced large-scale magnetic fields in the Venus ionosphere*. J. Geophys. Res. 89, 362–368

Luhmann, J. G., Russell, C. T., Schwingenschuh, K. and Eroshenko, E., 1991. *A comparison of induced magnetotails of planetary bodies - Venus, Mars, and Titan*. J. Geophys. Res. 96, 11199–11208

Lundin, R. and Barabash, S., 2004. *The wakes and magnetotails of Mars and Venus*. Advances in Space Research 33, 1945–1955

Mahajan, K. K. and Dwivedi, A. K., 2004. *Ionospheres of Venus and Mars: a comparative study*. Advances in Space Research 33, 145–151

Mahajan, K. K., Lodhi, N. K. and Singh, S., 2010. *Observations of electron density and electron temperature during large scale magnetic fields in the dayside Venus ionosphere and lesson for Mars*. Geophys. Res. Lett. 37, L06202

Mantas, G. P. and Hanson, W. B., 1979. *Photoelectron fluxes in the Martian ionosphere*. J. Geophys. Res. 84, 369–385

Martinecz, C., 2008. *The Venus Plasma Environment: a comparison of Venus Express ASPERA-4 measurements with 3D hybrid simulations*. Ph.D. thesis, Technical University of Braunschweig

Martinecz, C., Boesswetter, A., Fränz, M., Roussos, E., Woch, J., Krupp, N., Dubinin, E., Motschmann, U., Wiehle, S., Simon, S., Barabash, S., Lundin, R., Zhang, T. L., Lammer, H., Lichtenegger, H. and Kulikov, Y., 2009. *Plasma environment of Venus: Comparison of Venus Express ASPERA-4 measurements with 3-D hybrid simulations*. Journal of Geophysical Research (Space Physics) 114, E00B30

Martinecz, C., Fränz, M., Woch, J., Krupp, N., Roussos, E., Dubinin, E., Motschmann, U., Barabash, S., Lundin, R., Holmström, M., Andersson, H., Yamauchi, M., Grigoriev, A., Futaana, Y., Brinkfeldt, K., Gunell, H., Frahm, R. A., Winningham, J. D., Sharber, J. R., Scherrer, J., Coates, A. J., Linder, D. R., Kataria, D. O., Kallio, E., Sales, T., Schmidt, W., Riihela, P., Koskinen, H. E. J., Kozyra, J. U., Luhmann, J., Russell, C. T., Roelof, E. C., Brandt, P., Curtis, C. C., Hsieh, K. C., Sandel, B. R., Grande, M., Sauvaud, J., Fedorov, A., Thocaven, J., Mazelle, C., McKenna-Lawler, S., Orsini, S., Cerulli-Irelli, R., Maggi, M., Mura, A., Milillo, A., Wurz, P., Galli, A., Bochsler, P., Asamura, K., Szego, K., Baumjohann, W., Zhang, T. L. and Lammer, H., 2008. *Location of the bow shock and ion composition boundaries at Venus - initial determinations from Venus Express ASPERA-4*. Planet. Space Sci. 56, 780–784

Moissl, R., 2008. *Morphology and dynamics of the Venus atmosphere at the cloud top level as observed by the Venus Monitoring Camera*. Ph.D. thesis, Technical University of Braunschweig

Nimmo, F., 2002. *Why does Venus lack a magnetic field?* Geology 30, 987–990

Parker, E. N., 1958. *Dynamics of the Interplanetary Gas and Magnetic Fields.* ApJ 128, 664–676

Parker, G. D. and Jokipii, J. R., 1976. *The spiral structure of the interplanetary magnetic field*. Geophys. Res. Lett. 3, 561–564

Pätzold, M., Häusler, B., Bird, M. K., Tellmann, S., Mattei, R., Asmar, S. W., Dehant, V., Eidel, W., Imamura, T., Simpson, R. A. and Tyler, G. L., 2007. *The structure of Venus' middle atmosphere and ionosphere*. Nature 450, 657–660

Phillips, J. L., 1987. *Comment on 'On the response of ionospheric magnetization to solar wind dynamic pressure from Pioneer Venus measurements'*. Geophys. Res. Lett. 14, 1068–1069

Phillips, J. L., Luhmann, J. G., Knudsen, W. C. and Brace, L. H., 1988. *Asymmetries in the location of the Venus ionopause*. J. Geophys. Res. 93, 3927–3941

Phillips, J. L., Luhmann, J. G. and Russell, C. T., 1984. *Growth and maintenance of large-scale magnetic fields in the dayside Venus ionosphere*. J. Geophys. Res. 89, 10676–10684

Phillips, J. L., Luhmann, J. G. and Russell, C. T., 1985. *Dependence of Venus ionopause altitude and ionospheric magnetic field on solar wind dynamic pressure*. Advances in Space Research 5, 173–176

Phillips, J. L., Luhmann, J. G., Russell, C. T. and Alexander, C. J., 1986. *Interplanetary magnetic field control of the Venus magnetosheath field and bow shock location*. Advances in Space Research 6, 179–183

Phillips, J. L. and McComas, D. J., 1991. *The magnetosheath and magnetotail of Venus*. Space Sci. Rev. 55, 1–80

Piccioni, G., Drossart, P. and Virtis-Venus Express Team, 2009. *A Review of the Main Results about Venus' Atmosphere from VIRTIS on Venus Express*. In *Lunar and Planetary Institute Science Conference Abstracts*, volume 40 of *Lunar and Planetary Institute Science Conference Abstracts*, page 2569

Russell, C. T., 1989. *Comment on 'On the response of ionospheric magnetisation to solar wind dynamic pressure from the Pioneer Venus measurements' by J. Kar and K. K. Mahajan*. Geophys. Res. Lett. 16, 771–772

Russell, C. T., 2004. *Outer planet magnetospheres: a tutorial*. Advances in Space Research 33, 2004–2020

Russell, C. T., Chou, E., Luhmann, J. G., Gazis, P., Brace, L. H. and Hoegy, W. R., 1988. *Solar and interplanetary control of the location of the Venus bow shock*. J. Geophys. Res. 93, 5461–5469

Russell, C. T. and Elphic, R. C., 1979. *Observation of magnetic flux ropes in the Venus ionosphere*. Nature 279, 616–618

Russell, C. T., Elphic, R. C. and Slavin, J. A., 1980. *Limits on the possible intrinsic magnetic field of Venus*. J. Geophys. Res. 85, 8319–8332

Russell, C. T. and Luhmann, J. G., 1997. *Earth: Magnetic field and magnetosphere*. In Shirley, J. H. and Fairbridge, R. W. (editors), *Encyclopedia of Planetary Sciences*, pages 208–211. Chapman & Hall

Russell, C. T., Luhmann, J. G. and Strangeway, R. J., 2006. *The solar wind interaction with Venus through the eyes of the Pioneer Venus Orbiter*. Planet. Space Sci. 54, 1482–1495

Russell, C. T., Strangeway, R. J., Wei, H. Y. and Zhang, T. L., 2010. *Venus Lightning: What We Have Learned from the Venus Express Fluxgate Magnetometer*. In *Lunar and Planetary Institute Science Conference Abstracts*, volume 41 of *Lunar and Planetary Institute Science Conference Abstracts*, page 1215

Russell, C. T., Zhang, T. L. and Wei, H. Y., 2008. *Whistler mode waves from lightning on Venus: Magnetic control of ionospheric access*. Journal of Geophysical Research (Space Physics) 113, E00B05

Schunk, R. W. and Nagy, A. F., 1980. *Ionospheres of the Terrestrial Planets*. Reviews of Geophysics 18, 813–852

Schunk, R. W. and Nagy, A. F., 2009. *Ionospheres. Physics, Plasma Physics and Chemistry, Second edition*. Cambridge University Press

Shinagawa, H., 2004. *The ionospheres of Venus and Mars*. Advances in Space Research 33, 1924–1931

Slavin, J. A., 2004. *Mercury's magnetosphere*. Advances in Space Research 33, 1859–1874

Slavin, J. A., Acuña, M. H., Anderson, B. J., Barabash, S., Benna, M., Boardsen, S. A., Fraenz, M., Gloeckler, G., Gold, R. E., Ho, G. C., Korth, H., Krimigis, S. M., McNutt, R. L., Raines, J. M., Sarantos, M., Solomon, S. C., Zhang, T. and Zurbuchen, T. H., 2009. *MESSENGER and Venus Express observations of the solar wind interaction with Venus*. Geophys. Res. Lett. 36, L09106

Slavin, J. A., Holzer, R. E., Spreiter, J. R. and Stahara, S. S., 1984. *Planetary Mach cones - Theory and observation*. J. Geophys. Res. 89, 2708–2714

Solomon, S. C., 1997. *Venus: Geology and geophysics*. In Shirley, J. H. and Fairbridge, R. W. (editors), *Encyclopedia of Planetary Sciences*, pages 895–904. Chapman & Hall

Svedhem, H., Titov, D., Taylor, F. and Witasse, O., 2009. *Venus Express mission*. Journal of Geophysical Research (Planets) 114, E00B33

Svedhem, H., Titov, D. V., McCoy, D., Lebreton, J., Barabash, S., Bertaux, J., Drossart, P., Formisano, V., Häusler, B., Korablev, O., Markiewicz, W. J., Nevejans, D., Pätzold, M., Piccioni, G., Zhang, T. L., Taylor, F. W., Lellouch, E., Koschny, D., Witasse, O., Eggel, H., Warhaut, M., Accomazzo, A., Rodriguez-Canabal, J., Fabrega, J., Schirmann, T., Clochet, A. and Coradini, M., 2007a. *Venus Express - The first European mission to Venus*. Planet. Space Sci. 55, 1636–1652

Svedhem, H., Titov, D. V., Taylor, F. W. and Witasse, O., 2007b. *Venus as a more Earth-like planet*. Nature 450, 629–632

Taylor, F. W., 1985. *The atmospheres of the terrestrial planets*. Geophysical Surveys 7, 385–408

Taylor, F. W., 2006. *Venus before Venus Express*. Planet. Space Sci. 54, 1249–1262

Taylor, H. A., Brinton, H. C., Bauer, S. J., Hartle, R. E., Cloutier, P. A. and Daniell, R. E., 1980. *Global observations of the composition and dynamics of the ionosphere of Venus - Implications for the solar wind interaction*. J. Geophys. Res. 85, 7765–7777

Titov, D. V., Svedhem, H., Koschny, D., Hoofs, R., Barabash, S., Bertaux, J., Drossart, P., Formisano, V., Häusler, B., Korablev, O., Markiewicz, W. J., Nevejans, D., Pätzold, M., Piccioni, G., Zhang, T. L., Merritt, D., Witasse, O., Zender, J., Accomazzo, A., Sweeney, M., Trillard, D., Janvier, M. and Clochet, A., 2006. *Venus Express science planning*. Planet. Space Sci. 54, 1279–1297

van Allen, J. A. and Frank, L. A., 1959. *Radiation Around the Earth to a Radial Distance of 107,400 km.* Nature 183, 430–434

Vasyliūnas, V. M., 2004. *Comparative magnetospheres: lessons for Earth*. Advances in Space Research 33, 2113–2120

Verigin, M. I., Gringauz, K. I., Gombosi, T., Breus, T. K., Bezrukikh, V. V., Remizov, A. P. and Volkov, G. I., 1978. *Plasma near Venus from the Venera 9 and 10 wide-angle analyzer data*. J. Geophys. Res. 83, 3721–3728

Wallis, M. K. and Ip, W., 1982. *Atmospheric interactions of planetary bodies with the solar wind.* Nature 298, 229–234

Williams, D. R., 2007. *Venus exploration timeline*. `http://nssdc.gsfc.nasa.gov/planetary/chronology_venus.html`

Williams, D. R., 2010. *Venus fact sheet*. `http://nssdc.gsfc.nasa.gov/planetary/factsheet/venusfact.html`

Woo, R. and Kliore, A. J., 1991. *Magnetization of the ionospheres of Venus and Mars - Results from radio occultation measurements*. J. Geophys. Res. 96, 11073–11081

Zhang, T. L., Baumjohann, W., Delva, M., Auster, H., Balogh, A., Russell, C. T., Barabash, S., Balikhin, M., Berghofer, G., Biernat, H. K., Lammer, H., Lichtenegger, H., Magnes, W., Nakamura, R., Penz, T., Schwingenschuh, K., Vörös, Z., Zambelli, W., Fornacon, K., Glassmeier, K., Richter, I., Carr, C., Kudela, K., Shi, J. K., Zhao, H., Motschmann, U. and Lebreton, J., 2006. *Magnetic field investigation of the Venus plasma environment: Expected new results from Venus Express*. Planet. Space Sci. 54, 1336–1343

Zhang, T. L., Delva, M., Baumjohann, W., Auster, H., Carr, C., Russell, C. T., Barabash, S., Balikhin, M., Kudela, K., Berghofer, G., Biernat, H. K., Lammer, H., Lichtenegger, H., Magnes, W., Nakamura, R., Schwingenschuh, K., Volwerk, M., Vörös, Z., Zambelli, W., Fornacon, K., Glassmeier, K., Richter, I., Balogh, A., Schwarzl, H., Pope, S. A., Shi, J. K., Wang, C., Motschmann, U. and Lebreton, J., 2007. *Little or no solar wind enters Venus' atmosphere at solar minimum.* Nature 450, 654–656

Zhang, T. L., Delva, M., Baumjohann, W., Volwerk, M., Russell, C. T., Barabash, S., Balikhin, M., Pope, S., Glassmeier, K., Wang, C. and Kudela, K., 2008a. *Initial*

Venus Express magnetic field observations of the magnetic barrier at solar minimum. Planet. Space Sci. 56, 790–795

Zhang, T. L., Delva, M., Baumjohann, W., Volwerk, M., Russell, C. T., Barabash, S., Balikhin, M., Pope, S., Glassmeier, K.-H., Kudela, K., Wang, C., Vörös, Z. and Zambelli, W., 2008b. *Initial Venus Express magnetic field observations of the Venus bow shock location at solar minimum*. Planet. Space Sci. 56, 785–789

Zhang, T. L., Delva, M., Baumjohann, W., Volwerk, M., Russell, C. T., Wei, H. Y., Wang, C., Balikhin, M., Barabash, S., Auster, H. and Kudela, K., 2008c. *Induced magnetosphere and its outer boundary at Venus*. Journal of Geophysical Research (Planets) 113, E00B20

Zhang, T. L., Du, J., Ma, Y. J., Lammer, H., Baumjohann, W., Wang, C. and Russell, C. T., 2009. *Disappearing induced magnetosphere at Venus: Implications for close-in exoplanets*. Geophys. Res. Lett. 36, L20203

Zhang, T. L., Khurana, K. K., Russell, C. T., Kivelson, M. G., Nakamura, R. and Baumjohann, W., 2004. *On the venus bow shock compressibility*. Advances in Space Research 33, 1920–1923

Zhang, T. L., Luhmann, J. G. and Russell, C. T., 1991. *The magnetic barrier at Venus*. J. Geophys. Res. 96, 11145–11153

Zhang, T. L., Schwingenschuh, K., Russell, C. T., Luhmann, J. G., Rosenbauer, H., Verigin, M. I. and Kotova, G., 1994. *The flaring of the Martian magnetotail observed by the PHOBOS 2 spacecraft*. Geophys. Res. Lett. 21, 1121–1124

Zurbuchen, T. H., Koehn, P., Fisk, L. A., Gombosi, T., Gloeckler, G. and Kabin, K., 2004. *On the space environment of Mercury*. Advances in Space Research 33, 1884–1889

Acknowledgements

I am very thankful to Dr. Markus Fränz, my supervisor at the MPS, for his support and help throughout the three years of my PhD. He has always been willing to reserve some time for explanations or for helping me to solve a problem. Markus also supplied me with his analyzing software, *ccati*, which saved me from having to spend a lot of time on programming plot layouts and thus enabled me to focus on my research. Even if there were some issues with my computer at work, he usually helped me out before I could even ask for aid at the computer centre. Furthermore, he provided me with the great opportunity to get into contact with other scientists at various conferences and ASPERA team meetings, and apart from the science part, he often showed me some nice places to visit at those locations.
To Prof. Dr. Uwe Motschmann, my supervisor at the Technical University of Braunschweig, I am grateful for his willingness to take me as a PhD student even though I had already been working on my thesis for two years when the decision for my enrollment in Braunschweig was made. Within a short time, he decided to supervise my thesis and gave me valuable ideas regarding my work from a more theoretical point of view. He also encouraged me to publish my results and to work on a comparison between data and simulations together with his PhD student Stefan Wiehle. Both of these propositions were a very good incentive for me and helped me to fit my work into a larger context.
Many thanks also to Prof. Dr. Kristian Schlegel for his willingness to act as a referee for my PhD thesis, and to Prof. Dr. Karl-Heinz Glaßmeier for being the chairman of the examination board during my PhD defence.
I am also indebted to Dr. Martin Pätzold, who was my PhD supervisor at the university of Cologne for two years. Within this time, besides giving me good advice regarding my thesis, he introduced me to the VeRa radio occultation experiment and provided me with ionospheric density profiles for a comparison with ASPERA data.
Many thanks to Dr. Dieter Schmitt, who is very successfully coordinating the Solar System School. He is putting a lot of effort into finding new students and helping the current students with all issues concerning their work and life in Lindau. His commitment supports the wonderful international atmosphere among the students, which I really enjoyed. This community feeling is increased by the yearly retreat, which is also organized by Dieter. The retreat is always a great opportunity to gain some additional skills during the workshops, but also to get to know interesting regions in Germany (even as a German) and, of course, to socialize with our fellow students. For me, the retreat was always a special and enjoyable event. My thanks go as well to Dr. Julia Thalmann who supports Dieter in the coordination of the School and is always willing to give advice to students.
To the directors of the MPS, Prof. Dr. Ulrich Christensen and Prof. Dr. Sami K. Solanki, for providing me with the unique opportunity to do my PhD at the Max Planck Institute

for Solar System Research. This institute has a very high reputation and I consider myself very lucky that I had the opportunity to experience this wonderful working atmosphere and very stimulating international environment.
I am thankful also to the members of the Planetary Plasma Group within the MPS. The weekly meetings were helpful to get into contact with institute members who are working on similar topics and could therefore provide valuable feedback and ideas. Among these people, my special thanks go to Dr. Cornelia Martinecz (now Dr. Cornelia Schlundt), who was in the last year of her PhD when I arrived at the institute, and due to the similarities of our topics was able to help me to get started. The same holds for Dr. Elias Roussos and Dr. Norbert Krupp, who offered me their help on several occasions.
I am very grateful to Peter Kollmann for all the hours we spent together studying plasma physics. Our discussions helped me a lot in the preparation for my PhD defence, and our free-time activities were a welcome break from studying. Thanks also to Daniel Verscharen and Lars Guicking for several good discussions and explanations.
To Claudia Rudolph, the institute's receptionist, and Sibylla Siebert-Rust, my group secretary, not only for their help in administrational issues and providing me with information, but also for their friendliness and their contagious good humour. They made my life in Lindau even happier.
To Petra Fahlbusch, for taking care of the guesthouses and always trying to make our lives there as easy as possible.
To the computer centre, for supporting me in case of technical problems.
To the whole ASPERA team, for providing a very inspiring and fruitful environment and giving me expert feedback on my research. The team meetings were always scientifically very stimulating for me.
To Werner Drost, my mathematics teacher at school, who recognized my interest in maths and science despite my quiet manners and often encouraged me to come to the front and present my results to the class. I am sure that this helped me to develop many of the abilities which I needed later in my studies and during my PhD. Tasks like giving a presentation in front of other people would have posed a much larger problem without him.
To Dr. Mike Bird, my diploma thesis supervisor. He deepened my interest in planetary physics and helped me to continue on the way towards my PhD.
To Prof. Dr. Klaus Jockers, for introducing the student choir in Lindau, which offered a great compensation for my work. I enjoyed it a lot! Moreover, I am grateful to Klaus for asking many critical questions about my topic, which made me rethink some assumptions and helped me to get a better overview.
To my friends at the institute, for making life in and around Lindau very enjoyable. There was generally a very positive atmosphere among the students, and every newcomer was welcomed. I learned a lot about other cultures (as well as about my own!), customs and languages. I found many good friends here and spent a great time with them.
To my friends outside the institute, especially Alice, Elisabeth and Ulrike. The four of us made our way through our physics studies in Bonn together. This path was not always easy or straightforward, which only made our friendship stronger. As a compensation for our studies, we spent many evenings with good food, some nice cocktails, watching movies etc. A very special experience that we shared was our participation in the parabolic flight, including all the months of ups and downs (and funny moments) in preparing our experiment. I am very, very glad to have you as my friends and I hope we will keep

up our regular meetings in Bonn also in the future.
To Rolf, who has been by my side for more than three years now. I am extremely happy that we have found each other. Your humour, your understanding and your love make me feel much more self-confident and valuable, and we complement each other in many respects. I am really looking forward to our common future.
To my parents, Christine and Klaus, for their support in every aspect of my life. They were always happy with my achievements and never put me under pressure. When my interest in science became apparent, my parents did everything they could to satisfy my thirst for knowledge. They brought me to scientific exhibitions, planetariums, talks and many more activities, and even bought me my own telescope for my 13th birthday. But one of their best accomplishments in this respect was probably that they convinced the director of my school to grant me some extra holidays so that I could participate in an international astronomy camp! Thank you very much for all you did for me and for making me the person I am now.
To my sisters, Lisa, Kathrin and Theresa, who sometimes gave me a hard time in the past, but who are very close friends nowadays. Thanks to you, our parents' house is always lively and I'm never getting bored when I come to visit. This also holds for my grandmother Alwine, who lives next door, so I spent a lot of time with her during my childhood and we developed a close relationship. Thank you for all your support and understanding.
To my other family members - my grandparents, uncles, aunts, and cousins. I always enjoy our annual meetings for Christmas, and we've shared many great moments in the past which I will never forget. In particular, our yearly camping trips throughout my childhood and youth were always a long-anticipated event for me.

Lebenslauf

Persönliche Daten

Name:	Anne Angsmann
Geburtsdatum:	9. Mai 1983
Geburtsort:	Oelde
Staatsangehörigkeit:	deutsch

Schulausbildung

1989 - 1993:	Grundschule St. Marien, Enniger
1993 - 2002:	Gymnasium St. Michael, Ahlen

Studium

2002 - 2008:	Studium der Physik (Diplom) an der Rheinischen Friedrich-Wilhelms-Universität Bonn
2005 - 2006:	Auslandsjahr an der Radboud Universiteit Nijmegen (Niederlande)
2008 - 2011:	Doktorarbeit an der “International Max Planck Research School” (IMPRS) in Katlenburg-Lindau und der Technischen Universität Braunschweig